

Experiments and Computer Simulations on Aerodynamic Drag Reduction of Light  
Vehicle-Trailer Systems

by

Henry Royce Boyer

A thesis submitted in partial fulfillment of the requirements for the degree of

Master of Science

Department of Mechanical Engineering  
University of Alberta

© Henry Royce Boyer, 2015

## **Abstract**

Wind-tunnel experiments and Computational Fluid Dynamics (CFD) were performed to study the effect a deflector had on the flow and drag force associated with a 2010 F-150 truck and cargo trailer (Light Vehicle-Trailer System - LVTS). Image Correlation Velocimetry (ICV) on smoke-wire streaklines measured the velocity field on the model mid-plane. CFD was used to elucidate the flow, calculate the drag force, and study the effects of a moving ground-plane and blockage. The drag was reduced by approximately 13% at a  $Re$  of 14,900 with a moving ground-plane, and 17% without. Experiments suggested that the large difference in  $Re$  between wind-tunnel and the full-scale 5 million is not expected to significantly diminish the full-scale relevance of the drag results. One low  $Re$  effect was the presence of a separation bubble on the hood of the tow vehicle whose size reduced with an increase in  $Re$ . Three other characteristic flow patterns were identified: separation off the lead vehicle cab, stagnation of the free-stream on the trailer face for the no-deflector case, and subsequent separation at the trailer front corner. Comparisons of the ICV and CFD results with no deflector indicated good agreement, particularly in the direction of the velocity vectors. The ICV method under-evaluated the speed of the flow by up to 15%. The smoke streaklines and CFD streamlines agreed well for the no deflector case. However, for the deflector case, the CFD found an entirely different topological solution absent in the experiment. A pair of vertically-oriented vortices were found, wrapped around the front of the trailer on the mid-plane.

## **Preface**

This thesis is a hybrid format between the traditional format and paper format. Chapters 1, 3, 4, 5, and 6 follow the traditional format, while Chapter 2 is from a published paper. All references are located at the end of the thesis.

Chapters 1, 3, 4, 5, and 6 are an original work done by Henry Boyer.

Chapter 2 of this thesis has been published as Boyer H., Sigurdson L., (2015) Flow Visualization of Light Vehicle-Trailer Systems Aerodynamics. *Journal of Visualization* 18 (3) pp. 459 – 468. The paper can be found online at: <http://link.springer.com/article/10.1007/s12650-014-0263-9>. I was responsible for data collection, analysis, and manuscript composition. L. Sigurdson was the supervisory author and was involved with manuscript composition, and was the project originator and supervisor.

## **Acknowledgements**

I would like to express my thanks to everyone involved with this project. First, I would like to thank Bradley Myers for his time and effort in helping select and manufacture the models used in this study. His help was invaluable and set the ground work for this project. Special thanks to Bernie Faulkner whose technical expertise was appreciated. Thanks to Dr. Zhu for allowing access to his research license for ANSYS CFX in the early parts of this study. I would like to express my gratitude towards Dr. Bob Koch and Dr. John Wilson for their constructive suggestions which improved the presentation and content of this thesis.

Second, I would like to thank Dr. Carlos Lange who has been my supervisor, course instructor, and friend. His insight into computational fluid dynamics was helpful throughout my research project, and I am glad that we could share a few laughs along the way.

Finally, I would like to express my gratitude to Dr. Lorenz Sigurdson. I am truly thankful for all the guidance and support you have given me throughout the time we have worked together. Our first meeting, before I was even his student, lasted for six hours, and since then you have been my supervisor, grad coordinator, course instructor, mentor and friend. The small talk, and bananas during our meetings will surely be missed.

Thanks to the National Sciences and Engineering Research Council who provided funding for this work in the form of Undergraduate Summer Research Award (USRA), and NSERC Discovery Grant No. 41747. I extend my thanks to FGSR for the Queen Elizabeth II scholarship.

# Table of Contents

Abstract .....	ii
Preface.....	iii
Acknowledgements.....	iv
List of Tables .....	x
List of Figures.....	xi
Nomenclature.....	xvi
1. Introduction.....	1
1.1 Background and Literature Survey .....	2
1.2 Development of an Equation for $C_d$ for Modern LVTS .....	4
1.3 Objectives .....	6
1.4 Outline of Thesis.....	7
2. Preliminary Flow Visualization Experiments of Light Vehicle-Trailer Systems Aerodynamics	9
2.1 Introduction.....	9
2.2 Methodology.....	9
2.2.1 Models.....	10
2.2.2 Instruments.....	10
2.3 Results and Discussion .....	11
2.3.1 Reasons for Appearance of Separation on the Hood of the Truck .....	13
2.3.2 Stagnation and Separation on the Trailer.....	17
2.3.3 Other Concerns .....	19

2.4 Conclusions.....	23
2.5 Acknowledgements.....	25
References.....	25
3. Experimental Setup and Methodology.....	26
3.1 Setup .....	26
3.1.1 Fluid Properties.....	27
3.1.2 Camera.....	28
3.1.3 Wind-tunnel .....	29
3.1.4 Controls – Timing Box .....	29
3.1.5 Strobe Lights.....	30
3.1.6 Smokewire .....	30
3.1.7 Vehicle-Trailer Models Chosen.....	31
3.1.8 Air Velocity Choice.....	31
3.2 Image Correlation Velocimetry .....	32
3.2.1 Flow Patterns for ICV Correlation.....	32
3.2.2 Image Acquisition and Calculation Methods and Challenges .....	34
3.3 Methodology.....	38
3.3.1 Wind-Tunnel Operation.....	38
3.3.2 Non-ICV vs. ICV Setup.....	39
3.3.3 Drop Collector .....	40
4. Computer Simulation Setup.....	43

4.1 Problem Description .....	43
4.2 Model Setup .....	44
4.2.1 Simplified Geometries .....	44
4.2.2 Mesh.....	45
4.3 Numerical Setup.....	51
4.3.1 Assumptions.....	51
4.3.2 Governing Equations .....	51
4.3.3 Equation Discretization.....	52
4.3.4 Solver Setup.....	52
4.4 Verification .....	57
4.4.1 Estimated Order of Truncation .....	57
4.5 Sample Results.....	60
5. Results and Discussion .....	63
5.1 Reynolds Number Effects.....	63
5.1.1 Effect of Reynolds Number on Simulation Drag.....	66
5.2 Blockage Effect, Domain and Mesh Independence .....	67
5.2.1 Blockage in Computer Simulation.....	67
5.2.2 Domain Independence and Richardson Extrapolation.....	69
5.2.3 Mesh Independence .....	70
5.3 Streaklines and Streamlines .....	71
5.3.1 Flow Separating from Truck Roof.....	71

5.3.2 With Deflector .....	73
5.3.3 Streamline and Streakline Comparison.....	75
5.4 Velocity Vector Plot .....	77
5.4.1 No Model .....	77
5.4.2 Model Without Deflector.....	81
5.4.3 Model with Deflector.....	84
5.4.4 Flow Profile Comparisons .....	86
5.5 Pressure Contours .....	89
5.6 Vortex Pair at Front of Trailer .....	90
5.7 Moving Ground-Plane .....	91
5.7.1 Effect on Flow Around Model.....	91
5.7.2 Effectiveness of Deflector with Moving Ground-Plane .....	96
5.7.3 Greenhouse Gas Emissions and Fuel Consumption Reduction.....	97
6. Conclusions.....	99
6.1 Summary.....	99
6.2 CFD Drag Force Reduction .....	99
6.2.1 Comparison of Preliminary Investigations with Final CFD Results .....	100
6.2.2 Relevance to Full-Scale Road Applications .....	100
6.3 Greenhouse Gas Emission and Fuel Savings.....	101
6.4 Experiment-Simulation Comparison Conclusions.....	101
6.4.1 Reynolds Number Effect.....	101

6.4.2 CFD Moving Ground-Plane.....	102
6.4.3 Streaklines and Streamlines .....	103
6.4.4 Velocity Vector Plots.....	104
6.5 Strictly Experimental Conclusions .....	104
6.5.1 Preliminary Experiments .....	104
6.5.2 Turbulent Bottom Boundary Layer.....	105
6.5.3 ICV Mean Stream Flow (No Model).....	105
6.6 Strictly Simulation Conclusions .....	106
6.6.1 Domain Independence .....	106
6.6.2 Mesh Independence .....	106
6.6.3 Pressure Contours .....	106
6.7 Future Work .....	107
References.....	108
7. Appendices.....	111
7.1 Appendix A – Image Correlation Velocimetry Program Settings .....	111
7.2 Appendix B – Dimensions of Models.....	113
7.3 Appendix C – Mesh Images of No Deflector Case.....	114

## List of Tables

Table 1: Time activation of instruments. ....	11
Table 2: Final Simulation Properties. ....	53
Table 3: Fluid Properties and Drag Coefficients Changes For Different Settings Between Original Simulation and Actual Lab Values. ....	66
Table 4: Fluid Properties for Domain Independence Test. ....	67
Table 5: Test Values for Domain Independence. ....	69
Table 6: Mesh Independence Test Results With and Without a Deflector. ....	70
Table 7: ICV Calculated Free-stream Velocity for Various Horizontal Locations, Nondimensionalized Velocity with Pitot-static Probe Velocity. ....	79
Table 8: Effect of Deflector on Coefficient of Drag with Moving Ground-Plane. ....	96

## List of Figures

Figure 1: Modern Light Vehicle-Trailer Systems. From left to right: a Fifth-Wheel, a truck or van with a Cargo Trailer, an SUV with Travel Trailer, a Jeep type vehicle with Classic Travel Trailer. Photo courtesy of Bradley Myers.....	1
Figure 2: Wind-tunnel model of Light-Vehicle Trailer System studied here. ....	7
Figure 3: Simplified computer model of Light-Vehicle Trailer System studied here. ....	7
Figure 4: Ford F-150 and cargo trailer, $Re = 13,700$ , flow is from right to left. ....	12
Figure 5: Ford F-350 and fifth wheel trailer, $Re = 13,700$ , flow is from right to left.....	12
Figure 6: Ford F-150 directly behind smokewire, $Re = 13,700$ . ....	14
Figure 7: Ford F-150, without roughness, $Re = 13,700$ .....	15
Figure 8: Ford F-150 with roughness, $Re = 13,700$ .....	15
Figure 9: Ford F-150 and cargo trailer without deflector. $Re = 13,700$ .....	16
Figure 10: Ford F-150 and cargo trailer with deflector. $Re = 13,700$ .....	16
Figure 11: Ford F-350 with fifth wheel trailer, $Re = 13,700$ . ....	18
Figure 12: No model present with wind-tunnel running.....	19
Figure 13: Only truck model present in wind-tunnel.....	20
Figure 14: Truck and trailer present in wind-tunnel. ....	20
Figure 15: F-150 and cargo trailer with deflector.....	22
Figure 16: Sketch of experimental setup, from the side. The camera is placed between the wind-tunnel and the viewer. Flow is right to left breaking usual left to right convention. ....	27
Figure 17: No model heat wave intensity in smoke.....	33

Figure 18: ICV Photograph showing red and then delayed blue strobe exposures of smoke streaklines. ....	34
Figure 19: Beam splitter apparatus. Image used with permission of Chris Apps. (Apps 2001; Sigurdson 2003).....	37
Figure 20: Bottom boundary flow with drop collector. Flow in right to left direction.....	40
Figure 21: Bottom boundary flow without drop collector. Flow in right to left direction. ....	41
Figure 22: Bottom boundary flow without drop collector, laminar. Flow in right to left direction. ....	42
Figure 23: Side mesh for model with deflector. ....	46
Figure 24: Side mesh for model with deflector, detailed view. ....	47
Figure 25: Front view mesh for model with deflector. ....	47
Figure 26: $Y^+$ contour plot for LVTS without deflector.....	50
Figure 27: $Y^+$ contour plot for LVTS with deflector.....	50
Figure 28: Boundary conditions, front view. ....	55
Figure 29: Boundary Conditions, side view. ....	56
Figure 30: Residual output for simulation without deflector.....	60
Figure 31: Force plot for simulation without deflector.....	61
Figure 32: Side view of pressure contour on the surface of the LVTS with no deflector .....	62
Figure 33: Top view of pressure contour on the surface of the LVTS with deflector. ....	62
Figure 34: Hood separation, $Re = 15,800$ . Flow in right to left direction, contrary to convention. ....	64
Figure 35: Hood separation reduced, $Re = 44,400$ . ....	65

Figure 36: Coefficient of Drag vs. Blockage Percent, for varying domain sizes. ....	68
Figure 37: Main flow streamlines over truck with no deflector, $Re = 15,800$ . Flow in right to left direction, contrary to convention. ....	72
Figure 38: Simulation featuring streamlines creating a flow channel between the truck and trailer. ....	73
Figure 39: Simulation streamlines of mean stream flow over model with deflector. Flow in right to left direction, contrary to convention. ....	74
Figure 40: Experimental streaklines of mean stream flow over model with deflector. ....	75
Figure 41: Streamline, streakline overlay with no deflector. Flow in right to left direction. $Re = 14,900$ . ....	76
Figure 42: Streamline, streakline overlay with deflector. Flow in right to left direction. $Re = 14,900$ . ....	76
Figure 43: Image Correlation Velocimetry, vector plot of mean stream flow (Positions nondimensionalized with the trailer height of 115.26 mm, and velocities nondimensionalized with free-stream Pitot-static probe measurement). ....	78
Figure 44: Nondimensional horizontal velocity, mean stream flow 2.34 m/s. ....	79
Figure 45: Nondimensionalized vertical velocity showing the buoyancy with no model present. ....	81
Figure 46: ICV Model without deflector (velocity nondimensionalized with $U_{\infty} = 2.34$ m/s). ....	83
Figure 47: Simulation velocity contour and vector plot (velocity nondimensionalized with $U_{\infty} = 2.34$ m/s). ....	83
Figure 48: ICV Model with deflector (velocity nondimensionalized with $U_{\infty} = 2.34$ m/s). ....	85
Figure 49: Simulation velocity contour and vector plot (velocity nondimensionalized with $U_{\infty} = 2.34$ m/s). ....	85

Figure 50: Vector plot comparisons between simulation and ICV. Blue/Hollowed vectors are from the simulation. Black/Filled vectors are from ICV. The error bar shown in the image is the uncertainty in the ICV method. The nondimensionalized error is plus/minus 0.3 from the middle of the error bar. ....	87
Figure 51: Vector comparison between simulation and experiment with deflector. Blue/Hollowed vectors are from the simulation. Black/Filled vectors are from ICV. The error bar shown in the image is the uncertainty in the ICV method. The nondimensionalized error is plus/minus 0.3 from the middle of the error bar.....	88
Figure 52: Pressure contour model no deflector according to CFD. ....	89
Figure 53: Pressure contour model with deflector.....	89
Figure 54: Vortex wrapping around the front of the trailer. ....	90
Figure 55: Flow profile underneath vehicle with non-moving and moving ground-plane. (Position nondimensionalized by $h = 115$ mm, Velocity nondimensionalized by $U_{\infty}=2.34$ m/s)92	92
Figure 56: Simulation of LVTS with non-moving ground-plane. ....	93
Figure 57: Simulation of LVTS with moving ground-plane. ....	93
Figure 58: Simulation with deflector, stationary ground-plane.....	94
Figure 59: Simulation with deflector, moving ground-plane.....	94
Figure 60: Truck stagnation, non-moving ground-plane, no deflector.....	95
Figure 61: Truck stagnation, moving ground-plane, no deflector. ....	95
Figure 62: Overall dimensions of the model, truck and trailer. Dimensions in millimeters. ....	113
Figure 63: Dimensions of the deflector. Dimensions in millimeters.....	113
Figure 64: <b><i>Cd</i></b> vs. case number, overview of mesh evolution through testing. ....	114
Figure 65: No deflector side mesh.....	114

Figure 66: Zoomed view of no-deflector case side mesh. .... 115

Figure 67: Front mesh of no-deflector case. .... 115

## Nomenclature

### Latin Symbols

$a$	Refinement/Expansion rate
$A$	Front projected area for Light-Vehicle Trailer System [m <sup>2</sup> ]
$A_1$	Cross-sectional area of small domain [m <sup>2</sup> ]
$A_2$	Cross-sectional area of large domain [m <sup>2</sup> ]
$A_{Trailer}$	Front projected area for trailer [m <sup>2</sup> ]
$A_{Vehicle}$	Front projected area for vehicle [m <sup>2</sup> ]
$C_d$	Coefficient of Drag
$C_{dTotal}$	Coefficient of Drag for combined vehicle and trailer
CFD	Computational Fluid Dynamics
CDS	Central Differencing Scheme
$C_{dTrailer}$	Coefficient of Drag, for trailer
$C_{dVehicle}$	Coefficient of Drag, for vehicle
$D_{Total}$	Total drag of vehicle and trailer [N]
$D_{Vehicle}$	Drag of vehicle [N]
$D_{Trailer}$	Drag of trailer [N]
$F_d$	Force of drag [N]
$h$	Model height [m]
HVTS	Heavy-Vehicle Trailer Systems

ICV	Image Correlation Velocimetry
$k$	Conversion factor from pixels to meters, [pixels/m]
$k_t$	Turbulent Kinetic Energy
LVTS	Light-Vehicle Trailer Systems
$m$	Pixel indice
$N_1$	Number of nodes in coarse case
$N_2$	Number of nodes in refined case
$p$	Calculated order of discretization
$P$	Pressure [Pa]
$pixel_m$	Pixel velocity [pixel]
Re	Reynolds number
$Re_h$	Reynolds number, based on model height
$R_{specific}$	Specific gas constant [J/(kg K)]
RMS	Root Mean Squared
RPM	Revolutions Per Minute [rev/min]
$T$	Temperature [K]
$\Delta t$	Time difference between strobes [s]
$u$	x-component of the velocity
$u_\tau$	Shear velocity [m/s]
$U_\infty$	Free-stream velocity [m/s]
$U_i$	Mean velocity component

$U_m$	Calculated velocity at pixel $m$
UDS	Upwinding Difference Scheme
$v$	y-component of the velocity
$w$	z-component of the velocity
$\Delta x_1$	Coarse element length [m]
$\Delta x_2$	Refined element length [m]
$x$	x coordinate
$x_i$	Direction component
$y$	y coordinate
$y^+$	Normalized distance from first node to wall based on shear velocity
$z$	z coordinate
Greek Letters	
$\beta$	Blockage Ratio
$\delta_{ij}$	Kronecker delta
$\varepsilon$	Eddy viscosity
$\epsilon_h^d$	Error due to discretization
$\mu$	Dynamic viscosity [kg/(m s)]
$\mu_t$	Turbulent viscosity [kg/(m s)]
$\nu$	Kinematic viscosity [m <sup>2</sup> /s]
$\rho$	Density [kg/m <sup>3</sup> ]

$\rho_{air}$	Air density [kg/m <sup>3</sup> ]
$-\rho\overline{u_i u_j}$	Reynolds stress
$\tau_{ij}$	Newtonian stress tensor
$\tau_w$	Wall shear stress [N/m <sup>2</sup> ]
$\phi_{\Delta x_1}$	Value of interest
$\phi_{exact}$	Estimate of exact value
$\omega$	Turbulence frequency

## 1. Introduction

Vehicle aerodynamics are a large part of the current design process for many vehicles. However, this design is usually done with only the vehicle in mind and does not account for the use of a trailer. Thus many different vehicle combinations have quite poor aerodynamics, resulting in increased fuel consumption and greenhouse gas emissions. In 2009 Canada joined the Copenhagen Accord, which set the goal of reducing greenhouse gas emissions to 17% less than 2005 levels by 2020 (Environment Canada 2013). Recently, in May 2015 it was announced that Canada's new goal was to reduce greenhouse gas emissions to 30% less than 2005 levels by 2030 (CBC 2015). To assist in this effort a method of drag reduction on Light Vehicle-Trailer Systems (LVTS) is being studied here. Previous LVTS research is dated and was on vehicles that did not represent modern LVTS (Hands 1981; Beauvais 1967). In these studies the LVTS consisted of a car towing a small travel trailer (caravan). In contrast, modern vehicles used in LVTS include light duty trucks or Sport Utility Vehicles (SUV's), and less frequently used are vans and cars. Modern trailers have three common designs; travel trailers, fifth wheel trailers, and cargo trailers. An example of modern combinations can be seen in Fig. 1.



**Figure 1: Modern Light Vehicle-Trailer Systems. From left to right: a Fifth-Wheel, a truck or van with a Cargo Trailer, an SUV with Travel Trailer, a Jeep type vehicle with Classic Travel Trailer. Photo courtesy of Bradley Myers.**

In these dated studies experiments were performed in wind-tunnels with drag measurements. One also used smoke visualization to detect how the flow was being altered by the presence of a deflector (Hands 1981). It was found that a reduction in the aerodynamic drag was obtained when the flow visualized by smoke indicated that the flow has been deflected from the front face of the trailer, reducing the high drag resulting from the stagnation region. In contrast, many studies on the use of drag reducing fairings have been undertaken for large Heavy Vehicle (tractor)-Trailer Systems (HVTS). Many aerodynamic modifications were found which could significantly reduce drag. In these studies a mixture of wind-tunnel experiments and Computational Fluid Dynamics (CFD) were used to study and analyze the flow, and determine the effectiveness of different fairings. They will be discussed in the Literature Survey section.

For HVTS a large reduction in drag could be achieved if the stagnation on the front face of the trailer was moved off it, by use of a deflector located on top of the cab of the tractor. However, in an HVTS the deflector would be located much closer to the trailer than in the typical LVTS. Therefore, the goal was to determine if the same effect can be obtained through the use of a similar deflector placed on the roof of a light truck, and to learn the characteristic flow patterns over a model modern LVTS by performing smokewire flow visualizations, Image Correlation Velocimetry (ICV), and CFD.

## **1.1 Background and Literature Survey**

To begin this study a literature survey was conducted in the field of LVTS drag reduction. It was found that little research had been completed for LVTS drag reduction, and what little work had been done was dated. It was found that for a small car towing a small camping trailer (caravan) a 15% reduction in the drag could be obtained with the use of a simple wedge deflector (Beauvais 1967). Currently, there are two deflectors on the market which are versions of a simple wedge deflector placed on the top of the tow vehicle. The first is the Aeroshield (2015) and the second is the Aeroplus (2015). The latter claimed a 15% fuel savings as determined by MIRA in the UK.

Conversely, a large majority of research has been done on HVTS. This was the case because companies that own fleets of HVTS want to save money wherever possible, and since there are so many HVTS travelling many miles, a small reduction in aerodynamic drag leading to a

reduction in fuel consumption would result in large monetary savings. It was shown that a moderate reduction in drag led to a lower amount of fuel consumption (Wood 2003). One further by-product of this reduction in fuel consumption is a reduction in greenhouse gas emissions. In one study it was found that approximately 67% of the power required to cruise at highway speeds for HVTS was to overcome the aerodynamic drag (National Research Council Canada 2012).

In these studies performed on HVTS many different fairings and other devices were made to reduce the drag. In addition to wind-tunnel experiments performed for HVTS, CFD was performed to study the drag reduction effects of fairings (Sitlani 2006). Most notably the gap between the truck and trailer was studied with attempts to block off the gap, or restrict the flow of air between the tractor and the trailer (Lakshman 2004; Buckley 1978).

Further attempts at drag reduction were made by analyzing the flow at the rear of the trailer (Wood 2003). More recently the addition of skirts on the underside of the trailer was proven effective (van Raemdonck 2008). The most effective method for reducing the drag of a HVTS was by adding a deflector to the roof of the tractor, which would deflect the flow of air up and over the front of the trailer. This was found to remove the free-stream impacting stagnation zone from the front of the trailer, and therefore, a large reduction in drag could be obtained. Since deflectors on the roof of the towing vehicle worked well for HVTS, there was an interest to determine how well they would work on LVTS. A large difference between an HVTS and LVTS is that the deflector is much closer to the trailer in an HVTS, and therefore the effectiveness of a deflector on a LVTS may be reduced.

Apart from these studies of fairings on HVTS a more fundamental understanding of the flow was required. This would allow for a more complete understanding of the flow characteristics present. A fundamental experiment was performed which studied the effect that geometric parameters had on the drag and flow field of two bluff bodies separated by a gap (Koenig 1985). In this study the drag of a flat-faced cylinder was studied when shielded by a disk placed coaxially upstream. The diameter of the disk and the gap distance from the disk to the cylinder were varied. They found that the drag of the cylinder could be reduced substantially if critical flow characteristics could be set. This happened when the disk's diameter and the gap distance

were such that the flow separating from the disk reattached exactly on the cylinder's front leading edge. Amazingly the coefficient of drag ( $C_d$ ) of the cylinder was reduced from 0.72 down to 0.03 at this critical flow. This finding indicated that if the flow about a LVTS could be altered in such a way that the flow separating from the tow vehicle reattached to the front leading edge of the trailer, a large reduction in drag was possible.

There was an interest in knowing about other forms of drag reduction for vehicles. One interesting concept was drafting (slipstreaming), which is the effective drag reduction of a body that is closely following another body. Therefore, the analogy for an LVTS is that the drag might be reduced if the trailer is set at an appropriate distance from the lead vehicle. Several research studies showed that if the gap between the bodies was at a critical value, then the  $C_d$  of each of the bodies could be reduced (Watkins 2008; Zhang 2012; Hammache 2002; Hong 1998; Browand 2004). However, it was also determined that if the two bodies are too close to each other there is a negative effect, and the  $C_d$  will actually be increased for the following body.

## 1.2 Development of an Equation for $C_d$ for Modern LVTS

As the literature survey progressed attempts were made to estimate what the potential  $C_d$  of a modern LVTS would be before and after drag reduction, and before experiments and simulations were performed. This would be useful as a guide during the study. The coefficient of drag for this study is defined as:

$$C_d = \frac{F_d}{\frac{1}{2}\rho U_\infty^2 A} \quad (1)$$

Where,  $F_d$  is the drag force,  $\rho$  is the density of the air,  $U_\infty$  is the free-stream velocity,  $A$  is the frontal projected area of the model. Furthermore, these estimated values of  $C_d$  could then be compared to the drag coefficients obtained from CFD. A general equation was developed for the  $C_d$  of any LVTS, which was then used to find the  $C_d$  of the F-150 truck and cargo trailer used in this study. This was helpful since  $C_d$  values of combined two-body LVTS are not easily attainable without performing experiments or simulations.

To start it was assumed that the total drag of the LVTS was simply the drag of the vehicle added to the drag of the trailer as shown in Eq. 2.

$$D_{Total} = D_{Vehicle} + D_{Trailer} \quad (2)$$

This straight-up addition of the two drag values is not a precise way of finding the combined drag of the model, because it does not account for the pressure interaction between the two bodies. Nonetheless, this formulation is being used because it is very simple and easy to use for preliminary estimates. Next the following was substituted in:

$$D_{Vehicle} = \frac{1}{2} \rho U_{\infty}^2 * C_{d_{Vehicle}} A_{Vehicle}$$

$$D_{Trailer} = \frac{1}{2} \rho U_{\infty}^2 * C_{d_{Trailer}} A_{Trailer}$$

Dividing through by  $\frac{1}{2} \rho U_{\infty}^2$ , and  $A_{Trailer}$  resulted in Eq. 3:

$$C_{d_{Total}} = C_{d_{Vehicle}} \frac{A_{Vehicle}}{A_{Trailer}} + C_{d_{Trailer}} \quad (3)$$

Equation 3 uses estimates of the  $C_d$  for the vehicle and trailer alone in a free-stream. It was assumed the trailer had the same  $C_d$  as a rectangular prism close to a wall. The  $C_d$  of many basic three-dimensional shapes had already been measured (Hucho 1998). The  $C_d$  of the vehicle was selected from a previous study which calculated the  $C_d$  for a generic truck shape.

When assuming the cargo trailer could be represented by a rectangular prism, a  $C_d$  of 0.85 was found (Hucho 1998). However, one study found that a travel trailer, of comparable size to the cargo trailer, had a  $C_d$  of 0.62 (Hucho 1998). To explain this large difference one idea was found in another study done on buses. There it was found that by rounding the front leading edges of a blunt faced body, the  $C_d$  could be substantially reduced (Hucho 1998). From this it was assumed that the travel trailer must have had rounded corners since its  $C_d$  was much lower than the  $C_d$  for a rectangular prism. A plot from the “bus study” correlated the difference in  $C_d$  versus the radius

of the corners, and it was determined that the corners of a rectangular prism needed a radius of 60 mm in order to reduce the prism's  $C_d$  from 0.85 down to 0.62.

The final estimated values of  $C_d$  and projected area for the 2010 F-150 and cargo trailer used in this study, based on the full-scale bodies, are as follows:

$$C_{d_{Vehicle}} = 0.35$$

$$A_{Vehicle} = 2.81 \text{ m}^2$$

$$C_{d_{Trailer}} = 0.62$$

$$A_{Trailer} = 5.03 \text{ m}^2$$

The  $C_d$  of the vehicle was selected from a study of a generic truck shape (Adem 2010), and the  $C_d$  for trailer was from the study presented by Hucho (1998). The final estimated  $C_{d_{Total}}$  of a modern LVTS was found to be 0.82, which will be compared to the  $C_d$  calculated from CFD later in the study. If the same drag reduction could be achieved in this study on a modern LVTS as the dated study presented by Hucho (1998) then the resulting reduced  $C_d$  would be 0.75. Therefore, it is expected that the  $C_d$  calculated for a modern LVTS before drag reduction should be approximately 0.82, and after drag reduction should be approximately 0.75. These estimated values of  $C_d$  give insight into the outcome to be expected of the experiments and simulations performed in this study.

### 1.3 Objectives

The objective of this study was to study the impact of a simple deflector on the flow and drag characteristics of a LVTS. Figure 2 shows the detailed Ford F-150 truck and cargo trailer physical model that was the subject of the present wind-tunnel experiments. A slightly simplified model was used in CFD, shown in Fig. 3. They allowed a comprehensive analysis of the 3D flow interaction with the models.



**Figure 2: Wind-tunnel model of Light-Vehicle Trailer System studied here.**

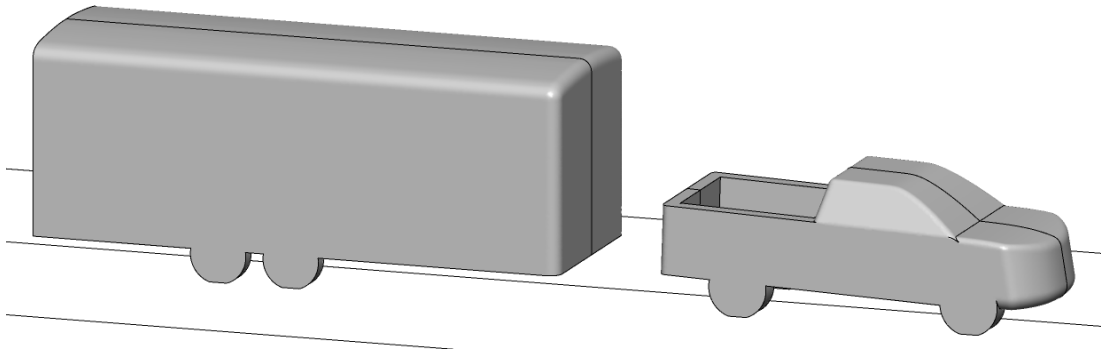


**Figure 3: Simplified computer model of Light-Vehicle Trailer System studied here.**

Two types of experiments were run. One took white-light strobe photographs of smokewire streaklines, which were used to assess the flow conditions and characteristics present in the wind-tunnel. The second type used the ICV method which required two different-coloured strobe lights to be used to illuminate the smoke at slightly offset times. ICV produced a velocity vector plot on the mid-plane of the wind-tunnel.

To compare the experiments with the simulations the experiment's streaklines and CFD streamlines were overlaid. Additionally, the vector plots from both were compared along selected profile lines. These comparisons were made with and without the deflector present on the roof of the truck.

## **1.4 Outline of Thesis**

Now that the introduction and background literature survey have been discussed, an outline of the rest of the thesis is given. Chapter 2 deals with the preliminary flow visualization experiments which were published in the Journal of Visualization. They were performed to learn

the characteristic flow patterns over the model representing modern LVTS, what improvement needed to be made in the experimental setup, and if there is an opportunity for reduction in aerodynamic drag. This Chapter discusses the outcome of the preliminary experiments and gives insight into the primary flow characteristics of an LVTS. It includes the first discovery of hood separation in this low Reynolds Number experiment and its effect on the flow patterns. Chapter 3 details the experimental setup and methodology. It discusses the implementation of the ICV and the methodology of the wind-tunnel experiments. Chapter 4 details the computational setup. It discusses the simplification of the model geometry for use in CFD, the creation of the mesh, and the solver setup. Furthermore, it includes a method for verifying if the simulation results are independent of the setup parameters. Chapter 5 contains the overall results and discussion. The effect of  $Re$  on the experiment and simulation is described. The results of the independence tests are also covered. The experiment's streaklines and CFD streamlines are compared as well as the velocity contour and vector plots between the simulation and experiment. The effect of a moving ground-plane on the drag is also estimated with CFD. Chapter 6 contains the final conclusions of this study.

## **2. Preliminary Flow Visualization Experiments of Light Vehicle-Trailer Systems Aerodynamics\***

### **2.1 Introduction**

A wide range of trailers with very poor aerodynamics are hauled long distances across a vast North American highway system. In 2009 Canada joined the Copenhagen Accord, which set the goal of reducing greenhouse gas emissions to 17 % less than 2005 levels by 2020 (Environment Canada 2013). To assist in this effort a method of drag reduction on Light Vehicle–Trailer Systems (LVTS) is being studied. Previous LVTS research is dated and was on vehicles that did not represent modern LVTS (Hands 1981; Beauvais 1967). In these studies, the LVTS consisted of a car towing a small travel trailer (caravan). In contrast, modern vehicles used in LVTS include light-duty trucks or sport utility vehicles (SUV) and less frequently vans and cars. For modern trailers there are three common designs: travel trailers, fifth wheel trailers, and cargo trailers. In these dated studies, wind-tunnel experiments were carried out with drag measurements and smokewire flow visualizations. It was found that a reduction in the aerodynamic drag could be obtained by optimizing the flow of air, shown by the streaklines, around the LVTS. The goal of this preliminary study was to learn the characteristic flow patterns over models representing modern LVTS by performing smokewire flow visualizations, learn what improvements need to be made in the experimental setup, and to see if there is an opportunity for reduction in aerodynamic drag.

### **2.2 Methodology<sup>†</sup>**

To study the flow of air around various tow vehicle and trailer models, a 0.3 m by 0.3 m wind-tunnel with a 0.91 m test section was used. The wind-tunnel is an open circuit suction style wind-tunnel capable of wind speeds up to 9 m/s. A wind speed of approximately 2 m/s was used in this study. This resulted in a Reynolds number (Re) of 13,700 based on the height of the model. This low speed was used to avoid the formation of a von Karman Vortex street

---

\* This chapter is a paper published in the Journal of Visualization and titled “Flow Visualization of Light Vehicle-Trailer Systems Aerodynamics”, (Boyer 2015). Small changes were made in light of thesis results.

<sup>†</sup> A more complete description can be found in Chapter 3 of this thesis.

behind the smokewire. This low speed also resulted in denser, higher contrast smoke streaklines for better photographic images. The downside is that the low  $Re$  creates a flow that does not have an appropriate transition of the boundary layer. Therefore, it may not represent the typical full-scale high  $Re$  flow of approximately 3 million with sufficient accuracy, as will be discussed later. The smokewire used in this study has a diameter of 0.127 mm. To further increase the contrast of the streaklines, a dark colored piece of matboard was affixed to the inside wall of the wind-tunnel. Its thickness (1 mm) was negligible and did not have any influence on the flow of air inside the wind-tunnel.

### ***2.2.1 Models***

The vehicle models used in this study were a Ford F-150 at a scale of 1/27 (dimensions LxWxH: 0.200 m x 0.074 m x 0.070 m) towing a cargo trailer, and a Ford F-350 at a scale of 1/32 (dimensions LxWxH: 0.184 m x 0.063 m x 0.060 m) towing a fifth wheel trailer. The trucks used in this study were detailed die-cast models, and both trailers were made of injection molded plastic. The Ford F-150 model required a small hitch to be built in order to attach the trailer to the rear of the truck. It was designed in order to hold the trailer level while achieving the proper gap between truck and trailer. The Ford F-350 and fifth wheel trailer had an attachment method already. The low  $Re$  models were held in place by looping plastic line around the front axle and feeding the line through a small hole in the floor of the wind-tunnel. On the outside of the wind-tunnel the line was tied into a loop, from which a weight was hung.

### ***2.2.2 Instruments***

Smoke streaklines were produced by evaporating mineral oil off a smokewire using the standard Vortex Fluid Dynamics Lab rig. The smokewire was heated up by passing an alternating current through the wire; this caused the mineral oil coating the wire to evaporate. Once the oil cooled it condensed into a visible smoke. The alternating current was driven and controlled using an inhouse-built variable voltage device. The value of alternating voltage used in this study was 8.0 volts. The measured smokewire resistance was 2.9  $\Omega$ . It was located 0.152 m upstream of the low  $Re$  model, except in a special test described later.

Images of the smokewire streaklines were captured using a Nikon D1X camera, and were illuminated using two GenRad Strobolumes. The experiment was controlled using a microsecond precision purpose inhouse-built timing system. The timing system controlled the activation of the smokewire, camera, and strobe lights. The timing settings can be found below in Table 1.

**Table 1: Time activation of instruments.**

Instrument	Time Activated (s)
Smoke-wire	0.5
Camera	1.1
Strobe Light	1.2

The camera was set to have an exposure length of  $1/20^{\text{th}}$  of a second, with a F-stop value of F3.2. Prior to activating the timing box, a drop of mineral oil was released to coat the smokewire.

## 2.3 Results and Discussion

Preliminary flow visualizations showed two major flow characteristics. The first was that the flow which separated from the truck would stagnate on the trailer's leading face at a distance approximately  $2/3$  of the way up from the bottom of the trailer body. The flow would continue up and over the top corner leading edge of the trailer where it then created the characteristic separation bubble on a blunt body. The second flow pattern found was the formation of an unexpected, large separated region over the hood of the towing vehicle that appeared to extend from the leading edge of the truck with a possible reattachment to the top of the passenger cab, or somewhere before. A full-scale truck is not expected to usually have this separation. This raised concerns that the low  $Re$  wind-tunnel model may not be a sufficiently accurate representation of the flow surrounding a full-scale high  $Re$  vehicle to reach meaningful conclusions. Therefore, this second flow pattern will be discussed first to convince the reader that the experiment is sufficiently accurate for a preliminary flow study. Early images of the flow visualization for the two LVTS that we did tests on can be seen in Figs. 4 and 5 below.

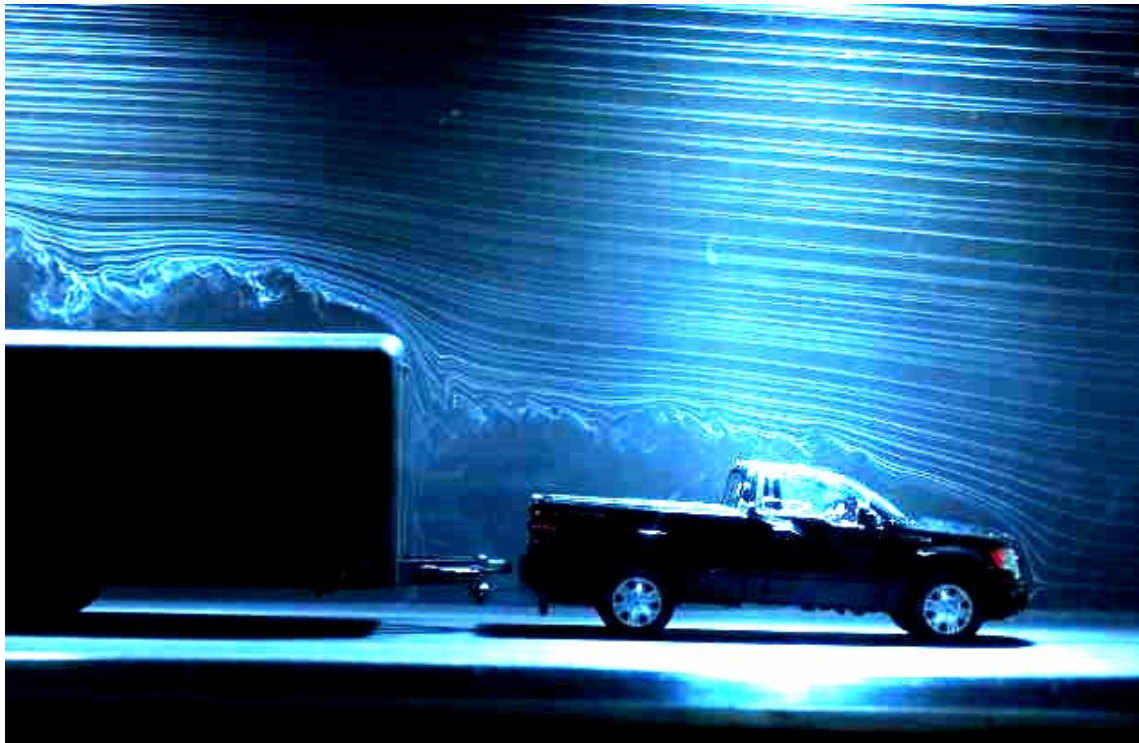


**Figure 4: Ford F-150 and cargo trailer,  $Re = 13,700$ , flow is from right to left.**



**Figure 5: Ford F-350 and fifth wheel trailer,  $Re = 13,700$ , flow is from right to left.**

### ***2.3.1 Reasons for Appearance of Separation on the Hood of the Truck***

From the stagnation point on the leading face of the vehicle the flow is expected to largely remain attached as it flows over the hood, and subsequently the windshield. The flow in this study did not exhibit such a flow pattern, instead it would separate over the hood and appeared to reattach at some point along the windshield. One possible reason for the formation of this separation bubble on the low Re model was that the stagnation point is too low on the front of the model, possibly caused by not having a moving ground-plane. This would cause the stagnation point on the leading face of the vehicle to move downwards, caused by the formation of a boundary layer under the truck reducing the amount of air flow under the model. The idea that the stagnation point on the leading face of the vehicle would move up when the ground-plane was made to move is contrary to what was found later after simulations were run, see Section 5.7.1. The stagnation point moved down when the ground-plane was made to move.

Another possibility that was investigated and ruled out was that there was not actually a separation bubble on the hood, but that it only appeared that there was one there. The hypothesis was that there was a stationary pair of counter-rotating vortices arcing over the hood of the truck, formed by the accumulated vorticity from the wake of the smokewire. These vortices would induce a velocity back upstream as the smoke streaklines reached the front of the truck. This induced velocity would cause the streaklines to be held off the model, not allowing the smoke to properly enter the boundary layer close to the surface of the truck. This would give the illusion of a separation bubble as the streaklines are being held off the model. To verify that these counter-rotating vortices were not the cause of the separation bubbles the model was moved a much shorter distance behind the smokewire. The expectation was that the vortices would not appear because the smokewire was in the stagnation zone and would therefore not have a significant wake vorticity to begin with. The separation bubble still appeared, thus it was concluded that a counter-rotating vortex pair was not the cause. Figure 6 below shows the truck placed directly behind the smokewire. The top leading corner of the hood is 4.5 mm (0.064 truck heights) from the smokewire; the smokewire was almost touching the bumper of the truck.



**Figure 6: Ford F-150 directly behind smokewire,  $Re = 13,700$ .**

The streaklines in Fig. 6 show that the separation bubble is still present over the hood of the truck. Since the separation bubble is still present, the counter-rotating pair of vortices was not responsible for the separation bubble over the hood of the truck.

A third possibility was that the separation bubble was actually there and was caused by the  $Re$  being too low. A standard approach is to use transition grit to induce a turbulent boundary layer which is less likely to separate, and therefore simulate a higher  $Re$  flow. The leading edge of the truck was roughened by attaching 200 grit sand paper to the model. The results of this test can be seen in Figs. 7 and 8. This test was simplified by only placing the truck model in the wind-tunnel.



**Figure 7: Ford F-150, without roughness,  $Re = 13,700$ .**

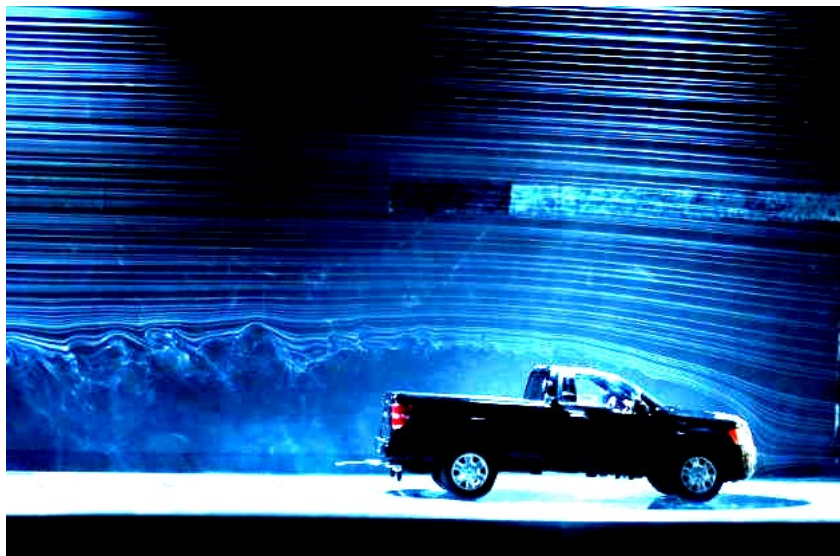


**Figure 8: Ford F-150 with roughness,  $Re = 13,700$**

By comparing Figs. 7 and 8 it can be seen that the addition of roughness at the trucks' leading edge did not have an effect on the separation bubble over the hood of the truck. This method proved difficult to implement as the paper was stiff, and did not conform easily to the shape of the truck. Furthermore, this method proved to have no effect on the separation bubble, therefore ruling this method out as a possible solution to the problem.

Another method attempting to reduce or remove the separation bubble was to put a small deflector on the floor with its leading edge 0.127 m (1.81 truck heights) upstream of the model. This wedge deflector is shown and described later. It is the same wedge deflector that was placed on the cab of the truck in the drag reduction attempt seen in Fig. 15. The effect this had on the flow can be found by comparing Figs. 9 and 10.



**Figure 9: Ford F-150 and cargo trailer without deflector.  $Re = 13,700$ .**



**Figure 10: Ford F-150 and cargo trailer with deflector.  $Re = 13,700$**

It can be seen from Figs. 9, and 10 that the deflector modified the flow enough that the separation bubble was reduced significantly. The flow appears to reattach to the lower portion of the windshield in the presence of the deflector. A question raised during the implementation of the deflector was how the flow around the trailer would be changed by the presence of the deflector. By analyzing these two images it can be seen that the stagnation point on the leading face of the trailer remains unchanged by the addition of the deflector. The location of the stagnation point on the leading face of the trailer is a defining flow characteristic in this study, along with the size of the separation bubble which is not seen to change. This suggests that the hood separation has no significant effect on the separation bubble or stagnation point on the trailer. Since the separation over the hood of the truck seems to have no major influence on the flow over the trailer, it is therefore concluded that these preliminary investigations are accurate enough to define the major flow patterns over models representing typical LVTS, despite the hood separation. Once other modifications are made to the truck however, to try to manipulate the flow into lower drag conditions, this may not be the case. The optimal design of added deflectors, such as the wedge deflector on the truck cab discussed later, is expected to rely significantly on proper modeling of the flow over the front of the truck.

The one drawback to the deflector upstream of the low Re model, in addition to the lack of a moving ground-plane, is that the flow of air around the bottom of the vehicle is even more inaccurately modeled in this experiment. However, the goals of this study are to see the major flow characteristics concerning the tops of the vehicle and trailer. While the flow of air around the bottom of the vehicle may be ignored for the moment, it must not be forgotten.

### ***2.3.2 Stagnation and Separation on the Trailer***

With the hood separation being ruled out as a potential influence on the trailer separation and stagnation point location, these two flow characteristics can now be analyzed. The flow of air once separating from the roof of the Ford F-150 impinges on the front leading face of the trailer resulting in a stagnation point. (This is a two-dimensional view, for the purposes of this discussion we are ignoring the three-dimensionality of the flow.) Once past the stagnation point the air is forced over the top corner leading edge of the trailer where it separates. The combination of both the large stagnation region on the face of the trailer, and separation over the

top of the trailer leads to an unfavourable high drag situation. If this flow were to be altered in order to have the flow reattach at the top leading edge of the trailer the drag would be reduced on the vehicle-trailer system (Koenig 1985). This would be analogous to the situation discussed by Koenig and Roshko for a disc placed in front of a blunt faced cylinder aligned with the flow, a model for a deflector in front of a semi-trailer truck heavy vehicle. An interesting result found on the Ford F-350 with fifth wheel trailer is that after the flow separates from the roof of the truck it appears to reattach somewhere on the truck bed behind the cab toward the back, beneath the bottom corner leading edge of the trailer near the hitch, as seen in Fig. 11.



**Figure 11: Ford F-350 with fifth wheel trailer,  $Re = 13,700$ .**

Apart from the flow reattaching in the hitch area, the flow patterns exhibited here are the same as those experienced with the cargo trailer. The flow separates from the roof of the towing vehicle and stagnates on the front leading face of the trailer, which is then followed by a separation zone over the top of the trailer. To improve the overall aerodynamics, the flow of air in front of either the cargo trailer or the fifth wheel trailer needs to be modified so that the flow reattaches to the top leading edge, thereby removing the stagnation point and the separated flow over the trailer.

### ***2.3.3 Other Concerns***

In addition to these two major flow characteristics, there exist a couple of problems that could further modify the flow from what would be experienced in the full-scale high Re situation. After looking at the preliminary results it was assumed that the streaklines in the far field (towards the top of the wind-tunnel) were being deflected upwards due to the blockage effect and buoyancy. Several tests were run to check if these assumptions were true. The first test consisted of running the wind-tunnel, and producing streaklines with no model in the tunnel, in the second test the truck was introduced to the tunnel, and in the third test the trailer was added. The results of these three tests can be seen in Figs. 12 – 14 below.

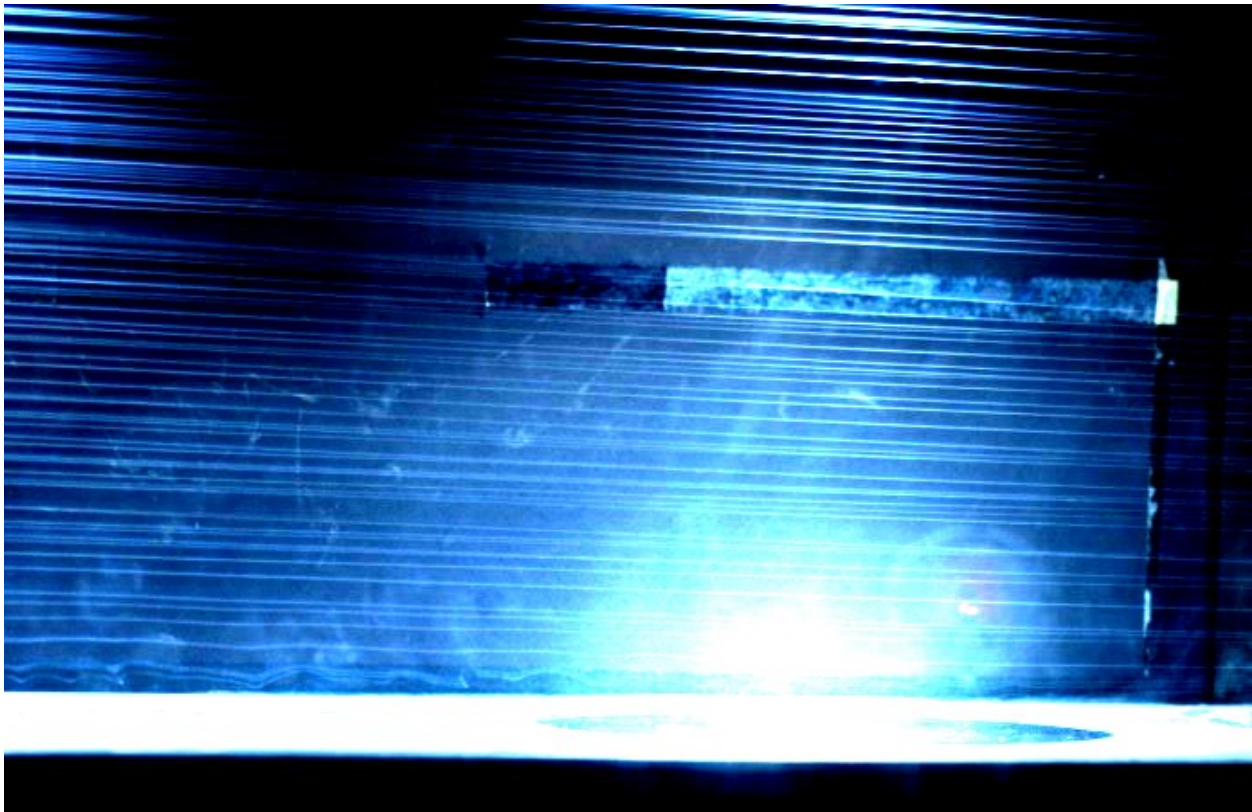


**Figure 12: No model present with wind-tunnel running.**



**Figure 13: Only truck model present in wind-tunnel.**



**Figure 14: Truck and trailer present in wind-tunnel.**

It can be seen by comparing the level of the streaklines to horizontal marker in the background that there exists some buoyancy effects; the best evidence of this is in Fig. 12. From the second test, Fig. 13, where the truck was placed by itself in the tunnel, the influence of the truck on the streaklines is only present a small way up from the truck's roof, approximately 0.85 truck heights, and is not present at the top of the wind-tunnel. For the third test where both the truck and trailer models were present it can be seen that the streaklines are influenced significantly more than when only the truck was present. However, by comparing the streaklines, located above the box of the truck, from Fig. 12 and Fig. 14, it can be seen that the influence of the truck and trailer on the flow does not drastically alter the flow in the far field (toward the top of the wind-tunnel). This shows that the largest factor affecting the flow is the buoyancy, while the effect of blockage is more difficult to determine.

Earlier it was stated that a reduction in aerodynamic drag is expected to be obtained if the flow of air over the vehicle was modified in an optimum way. A wedge deflector was added to the passenger cab of the F-150 and cargo trailer model to see if the flow of air surrounding the LVTS could be significantly affected; the results of this can be seen in Fig. 15 below.



**Figure 15: F-150 and cargo trailer with deflector.**

The relationship between the model visualization result and the expected drag coefficient of the model will now be examined. From Fig. 15 it can be seen that there is a significant modification to the overall aerodynamics. The deflector was setup to see if it could affect the flow. At this stage, there was no intent to optimize the effect. As a reminder, the focus of this paper was to learn the challenges of using a lower Re model for studying the influence of drag reduction devices, and the potential efficacy of a simple wedge deflector. By comparing Fig. 15 with previous images of the F-150 and cargo trailer, we can see that the stagnation point on the front of the trailer has been removed. This would suggest a significant reduction in the drag coefficient of the trailer. However the drag coefficient of the truck may have increased so that a careful further study is required to learn the net drag coefficient reduction on the overall LVTS. While the separation on top of the trailer still exists, it is hoped that this can be further reduced or removed by innovative modifications to the drag reduction device. So far, we have only used the simplest wedge device.

## 2.4 Conclusions

The goal of this preliminary study was to learn the characteristic flow patterns over low Re models representing modern LVTS by performing smokewire flow visualizations, learn what improvements need to be made in the experimental set-up, and to see if there is an opportunity for reduction in aerodynamic drag. Looking in the side view perpendicular to the main axis of the LVTS, it was found that there were two major flow patterns. The first was that the flow once separated from the towing vehicle, would impinge and stagnate on the leading face of the trailer. It would continue upward from the stagnation point and then separate at the top leading edge corner of the trailer. This indicated that there is an opportunity for vast improvement in the aerodynamic efficiency of the LVTS. The second notable feature of the flow pattern is that the flow of air would unexpectedly separate over the hood of the truck at the front upper corner. This is not a characteristic that is expected to usually be present in the full-scale higher Re situation. This source of inaccuracy between the model and full-scale was concluded to have minor effect on this preliminary study to find the major flow pattern characteristics.

A deflector was added to the roof of the truck and it was found that the stagnation point was removed from the front face of the trailer. This is expected to represent a reduction in the aerodynamic drag of the LVTS. While the deflector was not optimized in this study, it was found that it had a significant effect on the flow.

One possibility that was investigated and ruled out was that there was not actually a separation bubble on the hood, but that it only *appeared* that there was one there. The hypothesis was that there was a stationary pair of counter-rotating vortices arcing over the hood of the truck, formed by the accumulated vorticity from the wake of the smokewire. By changing the position of the smokewire it was concluded that an illusion created by a counter-rotating vortex pair was not the cause of the apparent separation bubble.

The presence of this separation bubble draws attention to the influence of the great Reynolds number variation between the lower  $Re = 13,700$  of the model compared to the much higher  $Re = 3$  million of a typical full-scale vehicle-trailer system. We cannot be absolutely certain of the relevance of the model visualization results to the full-scale, but only expect a qualitative modeling in any case. However, because it is a separated flow from the cab of the truck, or

deflector wedge if deployed, the  $Re$  is expected to have less of an influence downstream because the separated flow is fully turbulent. This conclusion is boosted by the observation that the presence or absence of the hood separation, which is an effect of  $Re$  via the boundary layer separation, has been shown to have no significant influence. Therefore, although the results for the model are not quantitatively expected to precisely mimic the full-scale, the study with models can be useful as a guide to what innovative drag reduction devices should be pursued in a higher  $Re$  wind-tunnel study of full-scale. Preliminary study of models is less expensive and allows easy modification to drag reduction device geometry.

Buoyancy and blockage are other experimental model accuracy concerns to take into account. Buoyancy is created when the smokewire heats up and warms the air flowing past it. This is seen as the streaklines trending upwards in the wind-tunnel as they traverse down the wind-tunnel. This was verified by running the wind-tunnel without a model present. From the images taken it was shown that there was a small amount of buoyancy present. Buoyancy cannot be removed from the experiment completely; therefore, it has to be taken into account when analyzing any results. The blockage effect is very important to consider when performing wind-tunnel experiments as the blockage of air can alter the flow of air around the model. In this study it was found that the blockage effect was minimal as the far field (towards the top of the wind-tunnel) streaklines were unaffected by the addition of the model to the flow. In this study it was difficult to determine the magnitude of the blockage influence, however it was deemed to be sufficiently small to make qualitative comparisons between models.

If further detailed studies with aerodynamics improvement devices are to take place, the hood separation will have to be reduced or completely removed from the system to more accurately model a truck towing a trailer. Possible other solutions not covered in this study are a moving ground-plane, or a raised ground-plane (false floor) where a less developed boundary layer will be formed when the flow encounters the truck. The most accurate representation of the flow around a truck-trailer system would be to have a moving ground-plane; however this is by far the most expensive and difficult to implement solution. A partial solution found in this study was to use a deflector upstream of the model to deflect the air up and over the leading edge of the truck. While this is expected to more accurately model the air flow over the LVTS, it less accurately models the air flow underneath the LVTS along the ground-plane. This was deemed to be an

acceptable trade off because without the presence of the moving ground-plane, the flow of air around the base of the truck was inaccurately being modeled already. When this solution was implemented and the flow of air was reattached sooner over the hood of the trucks, it was found that the flow of air to the trailer was unaffected in terms of the location of the stagnation point and the severity of the separation bubble over the top of the trailer.

## **2.5 Acknowledgements**

We thank the Natural Sciences and Engineering Research Council of Canada (NSERC) for the Discovery Grant 41747. We also thank Mr. Bradley Myers for his time and effort in helping select and manufacture the models used in this study, and the design of their mounting in the wind-tunnel. Mr. Bernie Faulkner is thanked for his help with the smokewire, camera and strobe system, including the design and construction of his “Bernie SuperBox” precision timing system.

## **References**

- Beauvais F. (1967) Aerodynamic Characteristics of a Car-Trailer Combination. SAE Paper No. 670100, Soc. of Automot. Eng., Warrendale, PA.
- Boyer H., Sigurdson L., (2015) Flow Visualization of Light Vehicle-Trailer Systems Aerodynamics. *J. Vis.* 18 (3) pp. 459 - 468
- Environment Canada (2013) Canada’s Emission Trends. Environment Canada, Gatineau, QC
- Hands S., Zdravkovich M.M. (1981) Drag Reduction for a Passenger Car Towing a Caravan. *J. of Wind Eng. and Industrial Aerodyn.* 9:137 – 143
- Koenig K., Roshko A. (1985) An Experimental Study of Geometrical Effects on the Drag and Flow Field of Two Bluff Bodies Separated by a Gap. *J. Fluid Mech.* 156:167 – 204

### **3. Experimental Setup and Methodology**

In the following chapter the setup and methodology used in the experiments will be discussed, as well as the selection of the detailed models. The setup explanation will cover the wind-tunnel, as well as the detailed use of the equipment such as the smokewire, camera, and strobe lights. The calculations of the air's density and viscosity in the lab will be discussed. ICV will be introduced and a brief explanation will be given on how it works. The assumptions and challenges of ICV will be discussed. Differences of illumination between non-ICV and ICV experiments will be explained. The removal of the drop collector will also be discussed.

#### **3.1 Setup**

As mentioned previously in Chapter 2 preliminary experiments using a scale model of a Light Vehicle-Trailer System (LVTS) were performed in a 0.305m x 0.305m wind-tunnel. Smoke streaklines were produced on the center plane of the wind-tunnel by letting a drop of mineral oil coat a small wire, which was then heated causing the mineral oil to evaporate. A timing apparatus was used to trigger the heating of the smokewire, the strobe lights, and a digital camera. Shown below in Fig. 16 is a sketch of the experimental setup.

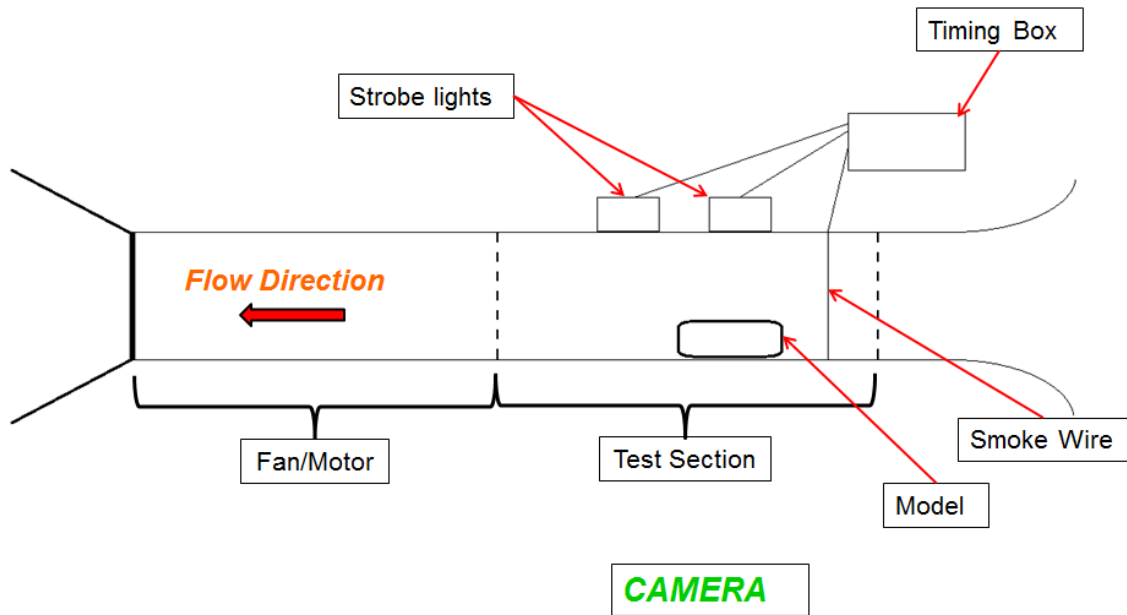


**Figure 16: Sketch of experimental setup, from the side. The camera is placed between the wind-tunnel and the viewer. Flow is right to left breaking usual left to right convention.**

### ***3.1.1 Fluid Properties***

In order to determine the Reynolds number and the correct fluid properties to use in the simulation, so that direct comparisons could be made between the experiment and simulation, the properties of the air in the lab had to be determined. To calculate the density of the air in the lab, the barometric pressure and temperature were needed. The air temperature in the lab was recorded at the beginning of every session, and monitored throughout for change. The barometric pressure was recorded at the beginning of each session where the Pitot-static probe was used. This was done because a precise measurement of the air velocity was required when calibrating the wind-tunnel or when ICV was being implemented. For the other sessions the air velocity was approximated by setting the wind-tunnel's fan at a RPM which corresponded to the proper velocity. The conversion from fan RPM to velocity was determined at the start of the study when the wind-tunnel was calibrated.

The air density was calculated assuming dry air, and was found using both temperature and pressure. The viscosity of the air was adjusted for temperature as the dynamic viscosity is independent of pressure.

The calculated air density was 1.093 kg/m<sup>3</sup>, and the dynamic viscosity was 1.86e-5 kg/ (m s). The density was calculated with the following equation:

$$\rho_{air} = \frac{P}{R_{specific}T} \quad (4)$$

The pressure, denoted by  $P$ , had a value of 93641.8 Pa, the temperature,  $T$ , had a value of 25.3 °C, and the specific gas constant had a value of 287.058 J/(kg K).

The viscosity was found using linear interpolation from the data in table A-9 for a temperature of 25.3 °C (Cengel 2010).

#### **3.1.1.1 Manometer**

To calculate the air velocity a manometer was used with a Pitot-static probe. The manometer was a Model 1430 Microtector made by Dwyer. This piece of equipment had a built-in micrometer which could be used to determine the height change of water in the u-tube by increments of 0.0254 mm (0.001 inch).

#### **3.1.2 Camera**

The camera used in this experiment was a Nikon D1X digital camera. The experiment did not have much light to illuminate the smoke; therefore the f-number of the camera was set as low as possible. This enabled the aperture of the camera to open as wide as possible which allowed the most amount of light through to the camera image plane. The shutter itself was triggered by the timing control box. In the study there were two sources of light, light from the strobe lights, and ambient light. The ambient light was unwanted in this study as it washed out the photos. To reduce the ambient light in the experiment, a cover was placed over the wind-tunnel and camera setup which blocked out much of the room's light. This resulted in higher quality photographs.

### ***3.1.3 Wind-tunnel***

The wind-tunnel used in this study was an open loop suction style. The test cross-section was a 0.305m x 0.305m (1ft x 1ft) that spanned 2.74 m (9ft). To ensure that the boundary layer would be as shallow as possible the first 0.914 m (3 ft) were used. To provide a background which was uniform and dark that would give good contrast for the streaklines a dark coloured matboard was installed on the bottom and back wall of the wind-tunnel. In addition to providing better contrast, the dark matboard covered the reflective surfaces which would wash out the photographs.

After the converging section of the wind-tunnel inlet a thin smokewire was run vertically in the center of the tunnel. Two small holes were drilled in the top and bottom plates of the wind-tunnel in order to allow the wire pass through. On the top of the wind-tunnel is a small oil reservoir which the smokewire passed through before entering the tunnel. The reservoir is a small container which holds the mineral oil for the experiment (Chapple 1998; Apps 2001). There is a hole in the bottom of the reservoir that allows the smokewire to pass through and enter the wind-tunnel; this hole is also where the mineral oil was released. The size of the hole is just enough so a single drop of oil can be released to run down and coat the smokewire if a small positive pressure is built up inside the reservoir. The pressure was increased by using a hand pump attached to a spout located on the lid of the reservoir. Normally a small drop collector is placed at the bottom of the tunnel for the smokewire to pass through; it is used to collect the excess oil. However, the drop collector was not used in this study; this is discussed later in Section 3.3.3.

### ***3.1.4 Controls – Timing Box***

In order to make the experiment more repeatable an electronic timing box was used to control the activation of the equipment. The timing box used was built in-house and featured ten independent channels that could be set with a resolution of one microsecond. When regular photos were taken (non-ICV) both strobes were controlled by the same channel to ensure that both strobes would be activated simultaneously. Conversely, when ICV photographs were taken, the strobes were triggered independently by two different channels so a small delay could be present between the two strobes (Apps 2001).

The equipment controlled by the timing box were the desk lamp, smokewire, camera, and strobe lights. The desk lamp was a small lamp that was used to illuminate the experiment since a hide blocked most of the ambient light from entering the test space. The power to the desk lamp was switched off prior to the photos being taken and turned back on after the photo was taken. The difficult part in taking good quality photos was in optimizing the timing of the strobes, camera, and smokewire. The smokewire was activated first; this allowed the streaklines to be produced and gave them time to traverse down the wind-tunnel where they would flow around the model. Next the camera was triggered to open the shutter, and a short time later the strobes were activated. The amount of time the camera's shutter was open was controlled by the camera, the timing box only triggered the camera's opening activation. Once the photo was taken the power to the smokewire was turned off, and the desk lamp was turned back on.

### ***3.1.5 Strobe Lights***

To illuminate the experiment, a light source that could flash brightly and instantaneously was needed. Therefore, two GenRad Strobolumes were used. They were placed on top of the wind-tunnel where the top plate of the wind-tunnel was a clear acrylic window. The strobe lights had many different functions; however, they were set to be automatically triggered and to flash only once. The strobe lights were set up differently depending on if normal non-ICV photos were being taken or if ICV was being done. These differences are discussed later in Section 3.3.2.

### ***3.1.6 Smokewire***

The wire used in the experiment was a tungsten wire with a diameter of 0.127 mm (0.005 inch). It was placed vertically in the middle of the wind-tunnel upstream of the model. As mentioned earlier the wire was passed through the oil reservoir at the top and the ground-plane at the bottom of the wind-tunnel. A small weight was suspended from the wire to keep the wire taut while the wind-tunnel was running. AC power was applied to the wire through leads at either end of the wire. The lead at the top was built into the oil reservoir in order to apply power below the reservoir, and the lead at the bottom was an alligator clip attached to the wire just outside the wind-tunnel. These leads were plugged into a Variac as a small amount of voltage was required. The Variac was switched on and off by the timing control box.

### ***3.1.7 Vehicle-Trailer Models Chosen***

Picking a model to study was a challenge as there are many different small trucks, and styles of small trailers to choose from. To reduce the number of combinations, the more common combinations were determined, and only one was selected for in-depth study. The more common combinations consisted of a pickup truck towing a recreational camping trailer, a pickup truck towing a fifth wheel camping trailer, a Sport Utility Vehicle towing a camping trailer, or a car towing a small trailer.

It was decided that the best combination to study was the combination that presented the best opportunity for a reduction in drag by the implementation of a drag reducing deflector. This was the truck towing a recreational camping trailer. However, for simplicity the recreational camping trailer was replaced with a cargo trailer of similar dimensions to a camping trailer. The truck that was used in this study was modeled after a Ford F-150. The models used in this study were at a scale of 1/27, and the overall dimensions of the models can be found in Appendix B.

The model was placed 0.38 model heights downstream of the smokewire.

### ***3.1.8 Air Velocity Choice***

There were several factors taken into account when selecting the air speed for the wind-tunnel experiments. First, well-defined discrete streaklines were required; in order to achieve this, the air speed had to be kept low. If set too high, the smoke's concentration would be reduced and as a result the intensity of the streaklines will be decreased making them harder to detect. Second, there is a critical  $Re$  which predicts the onset of a von Karman Vortex Street being shed from the smokewire. This critical  $Re$  (based on the smokewire diameter) is 50, which corresponds to an air speed of 6.7 m/s. Third, since the experimental model is being used to evaluate the flow characteristics of a full size model, it is normally best to keep the  $Re$  between the full-scale and model similar in magnitude. However, due to the limitations of the wind-tunnel this was not possible, and a lower  $Re$  had to be used. Although this  $Re$  disparity was not ideal, it will be shown later that as long as the  $Re$  is high enough the flow will remain qualitatively the same.

After taking these factors into account, an air speed of 2 m/s was chosen for the preliminary experiments as discussed in Chapter 2. The final experiments, in which ICV was performed, were run with an air speed of 2.34 m/s. There were also another set of experiments at 6.6 m/s to test the effect of Re on the results.

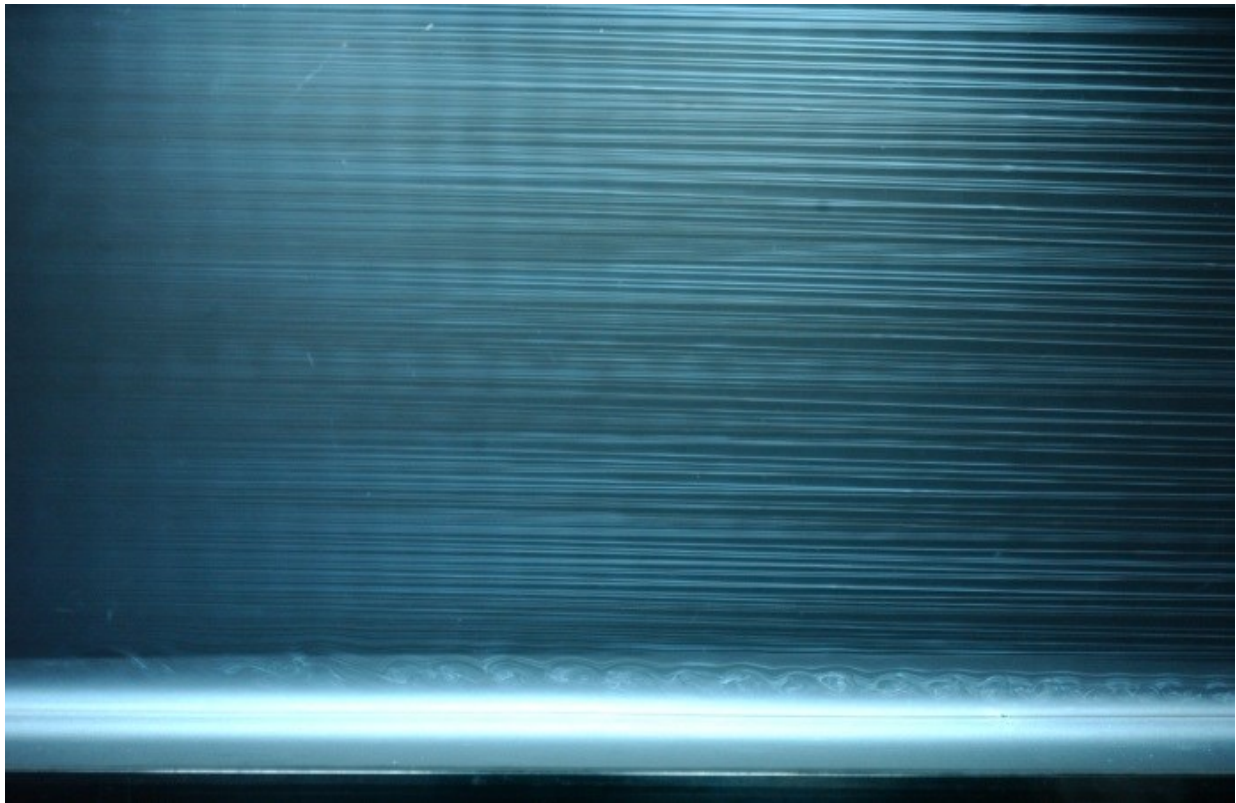
## **3.2 Image Correlation Velocimetry**

Image Correlation Velocimetry is a method which is used to produce a 2D vector plot of the flow field in a plane (Sigurdson 2003). One limitation of this method was the accuracy, which was highly dependent on the quality of the images and the strength of the pattern within them. ICV gave a reasonable approximation of the velocity vector field without the addition of new equipment other than the beam splitter apparatus. Once the simulations were compared with the experimental results and it was found that the two methods agreed reasonably well, other than some concerns for the deflector case, calculated values of drag from the simulation could then be used to give some indication of the effect a deflector might have on the model. In this study ICV performed well in describing the flow patterns; however, it under-predicted the velocity by up to 15% when compared with the measured velocity of the wind-tunnel using a Pitot-static probe indicating that its accuracy for these particular images was limited. While the Pitot-static probe only measured the air velocity at one point, it was assumed that the flow in the wind-tunnel was uniform. This assumption was proved correct when patterns in the smoke streaklines showed there to be a near uniform flow profile. Evidence of a uniform profile can be seen in Fig. 17 where the wave's varying intensity in the streaklines are seen to remain in vertical columns as the smoke traverses downstream. This suggests that the flow profile in the wind-tunnel is fairly uniform.

### ***3.2.1 Flow Patterns for ICV Correlation***

ICV works by analyzing patterns in a photo in order to produce a velocity vector and other plots. For this study, the deduced translation of two different patterns was used by the ICV program to calculate the vector field. One pattern was the fluctuating intensity of the smoke streakline. The second pattern was the presence of turbulence or swirling in the flow which created large-scale structures.

The presence of fluctuating intensity in the smoke streaklines was due to the 60 Hz alternating current of the power applied to the smokewire. However, because of the alternating current there was in fact a 120 Hz frequency in the heating of the smokewire. Due to the resistance in the wire, when power was passed through it, it began to heat up which caused the mineral oil to evaporate. At the high point in the rectified 60 Hz sine wave when more power was run through the wire, the oil would evaporate more quickly causing the smoke to become denser, making the streakline appear brighter since more light would be reflected. This is visualized by a 120 Hz wave pattern in the smoke's intensity which can be seen in Fig. 17. The ICV program uses this wave pattern to correlate on; however, it was not as effective as the patterns found in the shear layers where small turbulent vortices were present.



**Figure 17: No model heat wave intensity in smoke.**

In Fig. 17 it can be seen that there are light and dark vertical bands of smoke. The bright bands are where the smoke is denser due to the increased heating of the wire, while the dark bands correspond to a cooling of the wire. Figure 18 is a photograph when the ICV illumination method is used.



**Figure 18: ICV Photograph showing red and then delayed blue strobe exposures of smoke streaklines.**

From Fig. 18 it clearly shows that there are two distinct colour patterns in the smoke, one red and one blue. Problems with the ICV method arose when trying to find the velocity of the smoke around the top leading edge of the trailer, this challenge will be discussed in the next section.

### ***3.2.2 Image Acquisition and Calculation Methods and Challenges***

In order to produce a vector plot of the flow, two images of the smoke streaklines are taken at slightly different times and then compared by a computer program. By comparing these two images it can determine how far the patterns from the first image have shifted. To accomplish this, both images were super-imposed onto one photograph by performing a double exposure. This is done by opening the shutter of the camera, and activating two strobes, one after the other, with a known delay. To distinguish between the strobes, each one had its own coloured filter, one red and other blue.

The image taken is then analyzed by the ICV program. The analysis carried out is as follows:

1. A correlation window is selected by the program.
2. The red pattern inside the window is recorded to memory.
3. A search window is then moved over the rest of the image, comparing the blue pattern it finds with the red pattern in memory. This is done until the maximum search distance is reached.
4. After this whichever location had the highest correlation between the red and blue pattern is considered to be the location the smoke moved to from the original correlation window.

The program completes this cycle until it has analyzed the entire image. The search parameters and settings of the ICV program are controlled by the user through the use of a text file. The adjustable settings and their description can be found in Appendix A.

Once complete the ICV program outputs an ASCII data file with the results. The output variables are the pixel location, the intensities of the red and blue components in the original image, the value of the correlation coefficient, and the calculated pixel velocity components. The output had to be converted from the pixel velocity, represented as  $pixel_m$ , which was the distance in pixels that the pattern had moved, into physical velocities. To calibrate the conversion from pixels to meters a photograph of grid paper was taken, from this photograph the number of pixels were counted for a known length. This conversion factor is represented by  $k$  which is the physical length per pixel. Finally, the velocity was calculated by dividing the length by the time difference between the strobes,  $\Delta t$ . This conversion is summarized by the following equation:

$$U_m = pixel_m \times \frac{1}{\Delta t} \times k \quad (5)$$

Where,  $U_m$  corresponds to either the vertical or horizontal velocity.

### 3.2.2.1 Challenges with ICV

The main challenge with ICV is that the pattern in the smoke must remain relatively constant other than a simple translation between the two exposures (red and blue) in order to have a high correlation. Therefore, this method operates on the premise of Taylor's Hypothesis. Taylor's Hypothesis suggests that if the air velocity, carrying the turbulent eddies, is much greater than

the turbulent velocity it can be assumed that any changes are due to the passage of an unchanging pattern of turbulent motion (Taylor 1938). This hypothesis can be extended to say, for this study, that as long as the time difference between exposures is small enough the flow patterns' movement will primarily be a result of the main flow, and the underlying structure will remain unchanged. There are instances when this definitely does not hold.

To ensure that Taylor's Hypothesis remains valid, the air velocity and the time difference between strobe light flashes must be taken into account. The higher the air velocity, the smaller the time difference between the strobe flashes needs to be. This is important because the ICV program correlates from the red pattern of smoke to the blue pattern of smoke, and if the time difference between the two patterns is too large spatial resolution in the velocity detected is lost. For the waves on streaklines this would result in a loss of ICV velocity information in regions where there is accelerating flow, or flow curvature (direction change in the flow). This was particularly challenging when the model was present, as both effects exist due to the deflection of the flow, especially at the corners of the trailer.

At the corner of the trailer there were three other negative effects. They were caused by the unsteady wake of the truck distorting the streaklines which then impacted the face of the trailer and subsequently convected around the corner. First, if turbulence occurs there is increased mixing between the smoke and the surrounding air which results in a diminution of individual discrete streaklines as the smoke turbulently diffuses. Second, there may be turbulent mixing between the individual streaklines. Third, there is a smearing of the streaklines when they are brought together due to the acceleration of the flow as a result of mass conservation.

Additionally, due to the wave intensity pattern of the smoke if the time difference is too large the ICV program could possibly correlate to the wrong wave. This meant that the time difference had to be kept under a limit which was set at the period of the heating in the smokewire. Since the frequency at which the smokewire was heated was 120 Hz, the period was 0.0083 s. Therefore, a theoretical maximum  $\Delta t$  of 0.0083 s could be used before the wave pattern exactly overlapped itself; therefore, a much lower  $\Delta t$  of 0.0025 s was used. With this  $\Delta t$ , and an air velocity of 2.34 m/s the number of pixels spanned by one wavelength of the intensity pattern was

144 pixels. At the free-stream velocity this would mean that the smoke pattern translated 43 pixels, resulting in a pixel error of 1% (defined shortly).

Conversely, if the strobe flashes are too close together the uncertainty in the pixel displacement starts to become an issue. This is referred to as the pixel error (Sigurdson 2003). Pixel error is unavoidable and is due to the resolution of the image. It has a value of  $\pm \frac{1}{2}$  pixel. For example, if the displacement found by the ICV program is 5 pixels, the pixel error is 10%.

Another challenge is the careful way the experiment needs to be lit by the strobe lights. It was found that the light from the strobes had to appear (at least to the camera) that the light was being generated from the same physical location regardless of which strobe light was being used (Apps 2001). To achieve this, a beam splitter apparatus was used. Figure 19 below shows a schematic of the beam splitter apparatus. A disadvantage of this setup is that half of the light from each stroboscope is directed away from the area of interest.

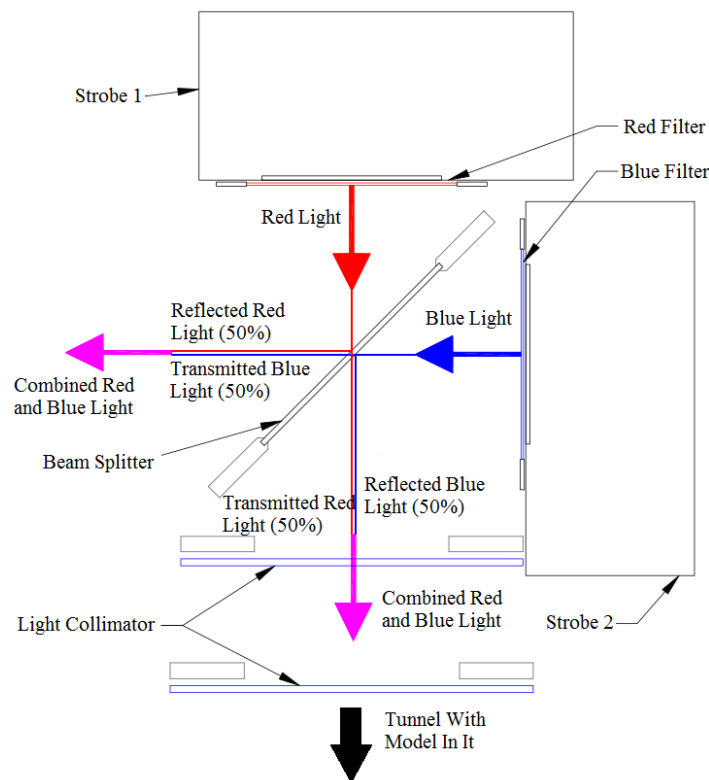


**Figure 19: Beam splitter apparatus. Image used with permission of Chris Apps. (Apps 2001; Sigurdson 2003)**

In order to see the time-average velocity vectors, which would show the steady-state flow, 50 photos were taken, and then the velocities at each point averaged. Since the timing between the photos was not identical, any frequency present in the flow was not missed or overlapped with the photographs taken. 50 photos were taken for several reasons. First, one photo was not enough because there were gaps in the vector field produced by the ICV method. Therefore, many photos were required in order to fill in the investigation region. Secondly, many photos were required in order to time-average the vector field. This average allowed for the steady-state vector field to be calculated for a better comparison with the simulations run later.

### **3.3 Methodology**

#### ***3.3.1 Wind-Tunnel Operation***

Before the experiment was run the wind-tunnel was turned on and allowed to warm up. It was found the wind-tunnel was unsteady for a period of time after being started, and required approximately 10 minutes before it settled at a constant air velocity. During this time the other equipment was readied for the experiment.

To control the speed of the air in the wind-tunnel the fan RPM was controlled. At the beginning of the study the wind-tunnel was calibrated, to determine the conversion between fan RPM and air velocity, using a Pitot-static probe and manometer. A calibration graph was produced, and was used for quick reference when the wind-tunnel's air speed could be approximated by setting only the fan RPM during the non-ICV experiments. However, when ICV was implemented the air velocity was measured via Pitot-static probe to ensure accuracy in the analysis.

For the final experiments, when ICV was used, the wind-tunnel's fan was set at the RPM at a value which corresponded with a velocity of approximately 2 m/s, and after a short time the RPM rose by about 20 RPM and plateaued. Once settled the final air velocity was measured, with the Pitot-static probe, and was found to be 2.34 m/s.

### 3.3.1.1 Reynolds number calculation

The Reynolds number,  $Re_h$ , based on the trailer's height above the ground-plane, was calculated using the air speed of the wind-tunnel, the calculated fluid properties of density and viscosity in the lab. The equation used was:

$$Re_h = \frac{\rho_{air} U_{\infty} h}{\mu} \quad (6)$$

Where,  $\rho_{air}$  is the density of the air with a value of 1.09 kg/m<sup>3</sup>,  $U_{\infty}$  is the free-stream velocity with a value of 2.34 m/s,  $h$  is the characteristic length based on model height with a value of 0.115, and  $\mu$  is the dynamic viscosity with a value of 1.86e-5 kg/ (m s).

### 3.3.2 Non-ICV vs. ICV Setup

A different setup was required for taking regular photographs of the smoke when lit with white light, and when ICV photographs were taken with red and blue light. For the white light, the strobes were not placed in the holder, and the red and blue filters placed over top of the strobes were removed. The strobes were positioned on top of the wind-tunnel where the light passed through a narrow slit, approximately 6.4 mm (1/4 inch). The slit was positioned along the centerline of the wind-tunnel; this focused the light to only illuminate the smoke streaklines. The collimation of the light in the regular photos was mandatory; otherwise the wide scattering of light would washout the photos after reflecting from parts of the test section due to the long exposure time of the camera. In addition to this, both strobes were connected and triggered by the same channel on the timing control box. This was done so that both strobes were activated at the same time to avoid ghosting of streaklines if the strobes were triggered at different times.

When ICV photographs were taken, the material used to make the slit was removed, and the beam splitter apparatus was moved into position. The trigger wire for each of the strobes was then hooked into independent channels on the timing control box.

### ***3.3.3 Drop Collector***

Early experiments, with no model present, showed that the flow along the bottom boundary of the wind-tunnel was quite turbulent. The cause of these structures was investigated since the flow was thought to be laminar in the beginning test section of the wind-tunnel. The most obvious cause of this turbulence was from the presence of the drop collector since it protruded from the wall. This collector is used to catch the excess oil from the wire, so that it does not pool on the bottom of the tunnel.

In order to study the effect the collector had on the flow photographs were taken with and without it. It was found that the wake of the drop collector was not the sole cause of the turbulence. With the drop collector present all the photos showed a turbulent boundary layer. After it was removed the boundary layer demonstrated transitional behaviour where it would alternate between being laminar and turbulent. Figures 20, 21, and 22 below show the flow along the bottom boundary with and without the collector being present. The flow is in the right to left direction, contrary to convention.

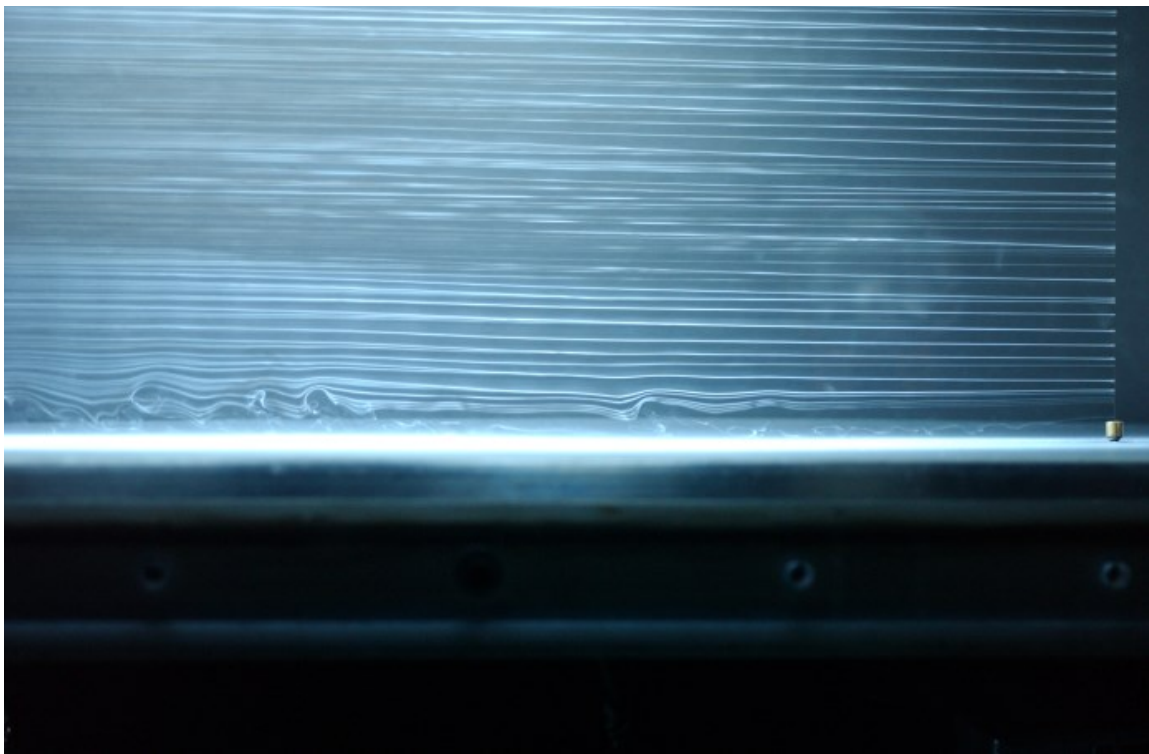


**Figure 20: Bottom boundary flow with drop collector. Flow in right to left direction.**

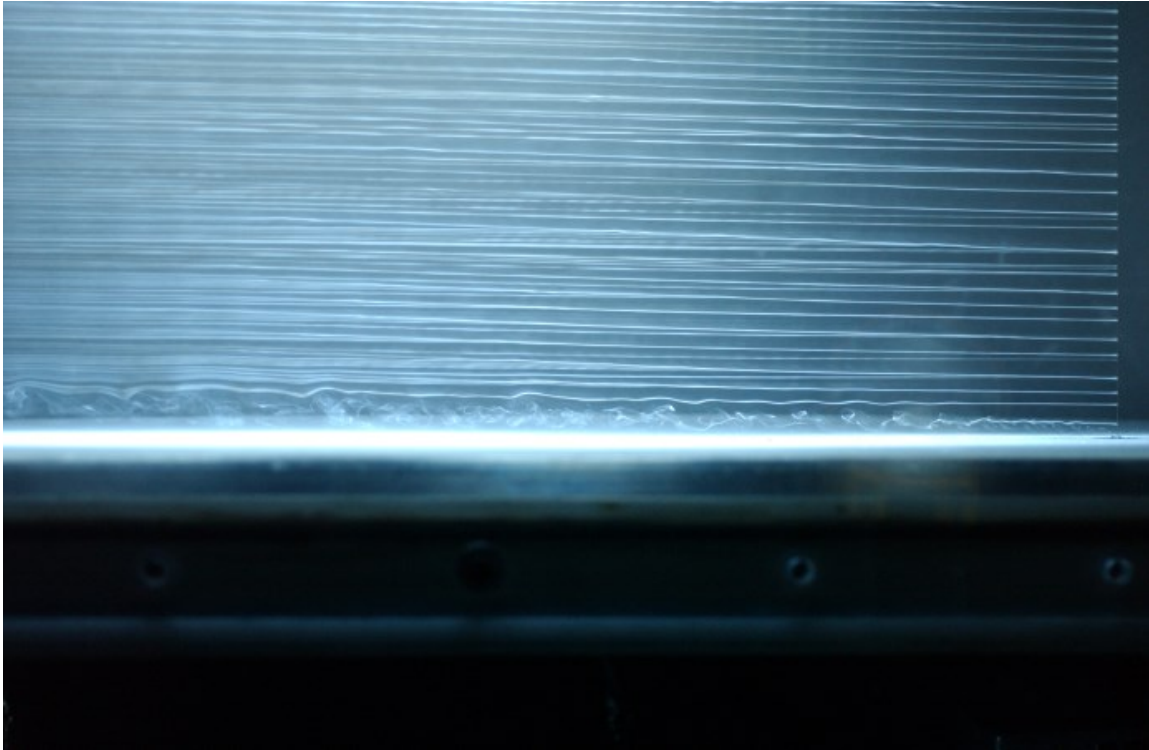


**Figure 21: Bottom boundary flow without drop collector. Flow in right to left direction.**

From Fig. 20 it can be seen that the turbulence is present downstream of the drop collector. Since the drop collector appeared to be causing this turbulence, it was removed and Fig. 21 shows the flow downstream of the smoke wire. It can be seen that turbulence is still present along the bottom boundary of the wind-tunnel, although it may be of smaller vertical dimension. As stated earlier it was observed that the bottom boundary layer was found to transition between laminar and turbulent without the drop collector present. Figure 22 shows the flow downstream of the smoke wire at an instant when the boundary layer was laminar.

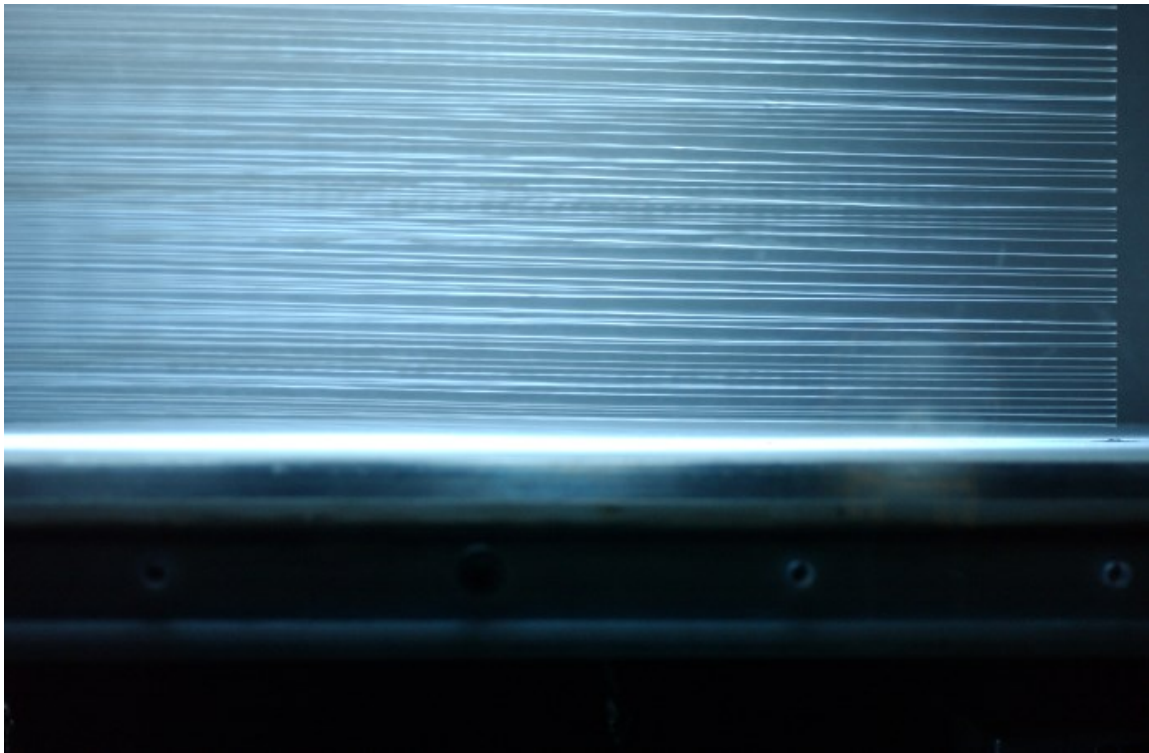


**Figure 22: Bottom boundary flow without drop collector, laminar. Flow in right to left direction.**

## **4. Computer Simulation Setup**

In the following chapter, the setup of the CFD models will be discussed. The problem description and the creation of the simplified models from the wind-tunnel models are discussed. The geometry and mesh generation are explained, as well as the implementation of a boundary inflation layer. The numerical setup and solver setup are covered, including the selection of a turbulence model, and boundary conditions. Verification methods detailing tests for mesh and domain independence as well as the estimated order of truncation are introduced. Sample results are provided which will be discussed in detail in Chapter 5.

### **4.1 Problem Description**

Computational fluid dynamics (CFD) simulations were performed in conjunction with wind-tunnel experiments. In order to have the best comparison between the two, the dimensions of all components were set as close as possible, and the Reynolds number of the flow was matched between both cases. Measurements were taken of the model used in the wind-tunnel and a corresponding simplified geometry was created using computer-aided design software. The domain of the simulation was modeled to have the same width, and height of the wind-tunnel to ensure the same blockage was experienced in both. The domain length was set and tested to ensure that the outlet boundary condition did not have a significant influence on the flow around the model. The fluid properties of the air were set to match the experiment; this included both viscosity and density. The inlet speed of the simulation was set at 2.34 m/s, to be the same as the wind-tunnel. The boundary conditions were also set the same. The walls and the body in the simulation were set to have a no slip condition, while the inlet had a constant velocity, and the outlet had zero velocity-gradient condition. The governing equations for the simulation were based on the steady-state Reynolds-Averaged Navier-Stokes (RANS) equations. One difference between the experiment and the simulation is the simulation was only run on half the model, while a symmetry boundary condition was used on the dividing plane. This dividing plane was set to be directly in the middle of the model. This is a technique used in CFD in order to make more effective use of computer resources and it is used when geometric and flow symmetry are present.

## 4.2 Model Setup

A CFD simulation requires several elements: a geometry, a mesh, and the simulation setup. In order to simulate the wind-tunnel as closely as possible, the fluid domain had the same width and height of the wind-tunnel, however, a vertical symmetry plane was used on the mid-plane of the model. There are a couple of assumptions associated with the use of a symmetry plane. The first assumption is that the geometry and flow conditions are symmetric about the symmetry plane. Secondly, the resulting flow is symmetric and steady, or transient without broken symmetries.

The inlet plane was put one model length ahead of the simulation model, approximately the same distance from the experimental model to the start of the wind-tunnel test section. This would account for the growth of the boundary layer that was formed along the bottom boundary since there is no moving ground-plane. The outlet of the simulation was set at 5 times the overall model length. This was done to ensure that the outlet boundary condition would not affect the flow upstream of the outlet. The location of the outlet plane was tested by varying its position by moving it both closer and further away to the model. It was then set at a position that was close enough to the model to not waste computational resources by having extraneous domain, and far enough away that its influence on the flow around the model was negligible.

As in the wind-tunnel a no-slip boundary condition was set on the bottom, side, and top walls. The bottom ground-plane was set to be stationary at first, and it was later made to move to investigate the effect of the moving ground.

### 4.2.1 Simplified Geometries

In order to perform CFD simulations a computer model of the experimental model had to be created. Dimensions of the experimental model were taken and used to produce the computer model. However, there were many fine details on the wind-tunnel model, such as wheel wells, rim details, and side mirrors. Finer details like these were omitted because they would have relatively minor impact on the flow, and would only lead to a waste of computer resources when it came to modeling the flow around such small detail. On the truck the underside was modelled as a being flat. The wheels were part of the main body and were not rotational as the bottom boundary was also set to be stationary. The hitch of the truck was not modelled either as this was

expected to have little impact on the flow. Even though the hitch was not modelled, the trailer was set at the proper distance behind the truck, as if the hitch was present. Like the wheels on the truck, the wheels on the trailer were part of the main body, and the bottoms were cut off. The underside of the trailer was also modelled as being flat. The simulation deflector was a 29 degree wedge and matched the dimensions of the experiment deflector within 3% of the height.

In addition to these details of the model being omitted, the bottom of the wheels on both the truck and trailer were flattened on the bottom by cutting off 0.74 mm off the wheels, this accounted for less than 1% of the overall model height.. This was done in order to avoid an error when creating the mesh. The error arose when, if the tire was unmodified, the bottom boundary wall would lay tangent to the wheel and the mesh program could not mesh to the singular point created by the tangent.

#### ***4.2.2 Mesh***

A thorough mesh analysis with many iterations was performed in order to ensure that a correct mesh was used in the final runs of the simulations. The influence of refining certain regions was tested, as well as the influence of inflation layers on surfaces with no-slip wall condition. The type of mesh generated for all cases was unstructured, consisting of mostly tetrahedrons, but also contained prisms, and pyramids. Unstructured grids were used in order to reduce the setup time for preparing the simulations.

Inflation layers were used on surfaces with no-slip wall conditions in order to more accurately capture the steep gradient of the boundary layer. Inflation layers are special elements produced on the surface of user selected faces. The elements in the inflation layers are extruded normal to the wall with the layers closer to the wall being the smallest. This was done in order to capture the steep gradient of the flow profile in the boundary layer on the walls. If an inflation layer was not present the velocity gradient would not be modelled accurately. Inflation layers are important on any surface that has a no slip condition present. Moreover, a highly refined inflation layer is required on any wall where the calculation of skin friction is needed.

Overall the mesh was highly refined around the LVTS, while a medium refinement was applied in the separation zone behind the LVTS and a smoothing refinement was used downstream of

that towards the outlet. These refinements were done in order to more accurately capture the high gradients in the velocities of the flow, and the flow direction changes. The refinement in the separation zone was required to accurately capture the pressure recovery at the rear of the LVTS, as it was found that the pressure drag was the largest contributing factor to the overall drag. An overview of all the mesh cases tested and their impact on the  $C_d$  value is shown in Appendix C.

The maximum number of nodes used in the mesh was determined by the amount of computer resources available, most importantly time. The final node count was approximately 2.8 million nodes in both the cases with and without the deflector. Figure 23 shows the overall side mesh from the deflector case.

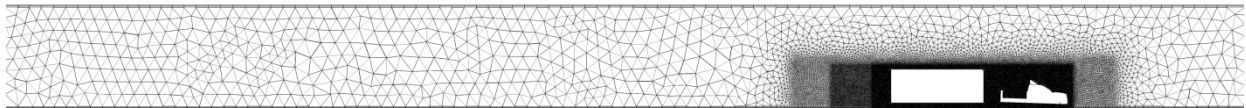


**Figure 23: Side mesh for model with deflector.**

From Fig. 23 it can be seen that there are four different refinement regions in the mesh. The mesh away from the LVTS did not need to be highly refined, since the flow is not changing significantly in this region. However, it was found that mesh refinement was required closer to the model. Therefore, two bodies of influence were created, one close to the model which was highly refined, and one further out which was an intermediate refinement. One further body of influence was included at the back of the model where a separation zone would be present. This was done because accurately predicting the pressure recovery at the back of the LVTS would have a significant impact on the calculated drag on the model.

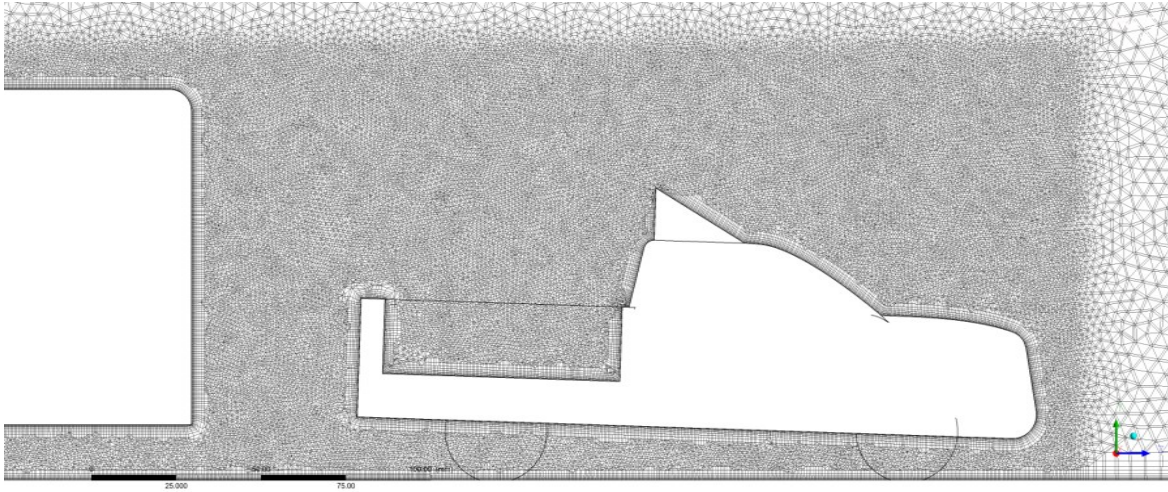


**Figure 24: Side mesh for model with deflector, detailed view.**

Figure 24 shows a more detailed view of the side mesh surrounding the truck and the front of the trailer. In it the inflation layer can be seen surrounding both the truck and the trailer. There is also an inflation layer present on the ground-plane.

Finally, the mesh viewed from the front of the model is shown below in Fig. 25.

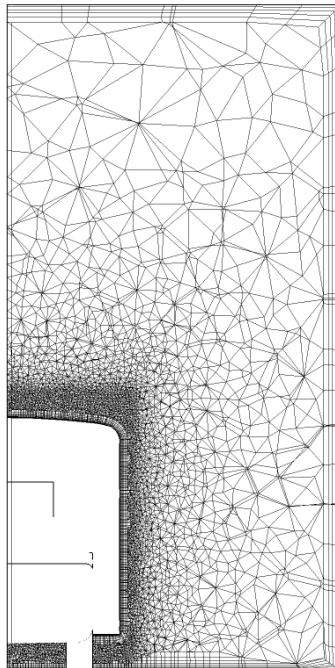


**Figure 25: Front view mesh for model with deflector.**

Figure 25 shows the mesh on a plane near the front of the trailer. Here it can be seen that there is an inflation layer present on the trailer, as well as on the bottom, side, and top walls. Images of the mesh for the no-deflector case can be seen in Appendix C.

#### **4.2.2.1 Inflation and Wall Treatment**

When a fluid flows over a no-slip boundary, a boundary profile is created which has a steep velocity gradient. In order to capture this gradient more accurately a meshing method known as inflation is introduced near the surfaces where a boundary profile will form. In a normally unstructured grid, tetrahedrons are the most common element as they are the easiest to implement for most geometries. In inflation layers using an unstructured grid the element shape is that of a triangular prism. The elements are produced by placing a triangle on the no-slip surface and then extruding it a short distance perpendicular to the wall. Several of these elements are stacked on top of each other with some set growth rate. Consequently, the element closest to the wall is the smallest, and with each added layer, the thickness of the element increases until the end of the inflation layer, where the mesh returns to the unstructured mesh using tetrahedrons. As a result of this layout the nodes in the vicinity of the wall are perfectly aligned and perpendicular to the wall allowing for an accurate calculation of normal gradients.

Inflation is very important as it can improve the accuracy of the results of the simulation by a significant amount. It is also very important if calculation of the wall shear is required. This is because with an inflation layer, the high gradient of the boundary layer can be more accurately captured, than if an unstructured mesh of tetrahedrons was used near a no-slip surface. In addition to the overall refinement of the inflation layer, the first layer's thickness is important to pay attention to, especially if a turbulence model is being used as part of the simulation. This is because in a turbulent boundary layer close to the wall there exists a viscous sublayer, and in order for the simulation to more accurately predict the flow close to the wall, it attempts to calculate the flow in the viscous sublayer. However, a grid sufficiently fine to capture this flow very accurately would waste time and computer resources, so models are used instead to calculate the flow near the wall. These models are known as Wall Treatment models (ANSYS, INC 2013, Ferziger 2002). There are traditionally two models to choose from, the first is the Log-Law of the Wall, where the flow follows a logarithmic function near the wall, and the

second model is known as Low-Re, where the flow follows a near linear growth in velocity directly next to the wall in the viscous sublayer. While ANSYS CFX does not allow for the wall treatment to be selected, there is a method which allows the user to infer which method has been used (ANSYS, INC 2013).

In order to check which wall treatment method was used a simulation needs to be run, and the  $y^+$  value on the no-slip surfaces needs to be plotted as a contour at the surface.  $Y^+$  is the normalized distance from the wall of the first node based on the shear velocity.  $Y^+$  is a calculated value and its equation is shown below in Eq. 7. Part of the  $y^+$  value requires the calculated shear velocity, which is shown in Eq. 8:

$$y^+ = \frac{u_\tau y}{\nu} \quad (7)$$

$$u_\tau = \sqrt{\frac{\tau_w}{\rho}} \quad (8)$$

Where,  $y$  is the distance from the wall to the first node,  $\nu$  is the kinematic viscosity,  $u_\tau$  is the shear velocity,  $\tau_w$  is the wall shear stress, and  $\rho$  is the density of the fluid. From Eq. 7 it can be seen that the only effective way to change the  $y^+$  value is to change the distance of the first node to the wall.

Once this is done, the minimum or maximum  $y^+$  (depending on the wall treatment required) is checked. If the minimum or maximum  $y^+$  meets the requirement for the model, then the grid is deemed acceptable. However, if the  $y^+$  falls outside the range for the wall treatment needed, then the inflation layer needs to be adjusted in order to have the first node moved either closer to or further away from the wall surface, until the requirement is met.

For this study, the turbulence model which was chosen required the use of the Low-Re Wall Treatment model, which meant that the  $y^+$  had to be kept below 4. In order to reduce the  $y^+$  the inflation layer had to be refined in order to have the first layer's thickness reduced and move the first node closer to the wall. If the  $y^+$  needed to be made larger the inflation layer had to be made coarser.

In order to make sure the  $y^+$  was below 4, an inflation layer was implemented and a simulation conducted. Once solved, a  $y^+$  contour plot was checked and the inflation layer adjusted accordingly. Figures 26 and 27 show contour plots of the  $y^+$  on the surface of the LVTS, without and with the deflector, from the final simulations. The maximum  $y^+$  is represented by the maximum on the legend. From this it can be seen that the maximum value of  $y^+$  was less than 4 for both cases.

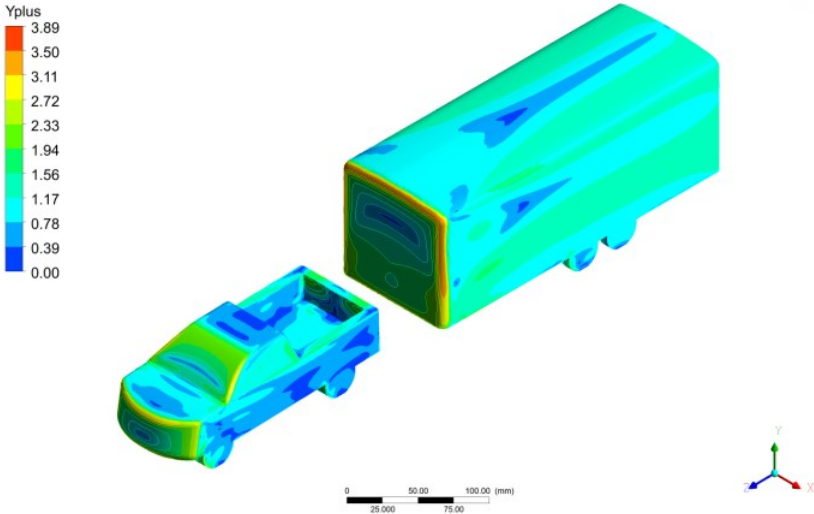


**Figure 26:  $Y^+$  contour plot for LVTS without deflector.**

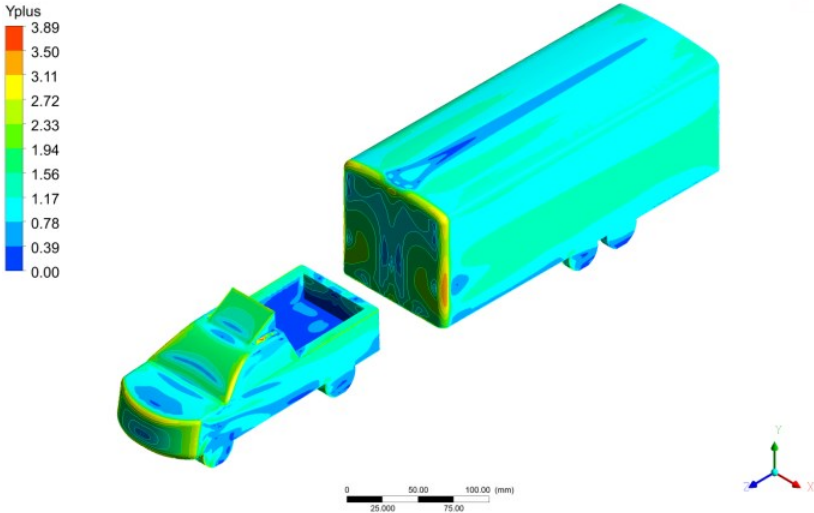


**Figure 27:  $Y^+$  contour plot for LVTS with deflector.**

The benefit of using the Low-Re model in conjunction with the  $k-\omega$  with Shear Stress Transport turbulence model is that this enables the models to predict the onset of flow separation relatively accurately (Menter 1996).

## 4.3 Numerical Setup

### 4.3.1 Assumptions

For this simulation the assumption of steady-state of the Reynolds-averaged solution is used. While a transient simulation would model the flow most accurately by capturing the fluctuations in the flow, the steady-state assumption will be sufficiently accurate for this case. With a Re number of around 16,000 it cannot be assumed that the flow is either Stokes or Euler flow, when looking to simplify the Navier-Stokes equations. In addition to the complexity of the flow associated with that high a Re number, turbulence is known to be present in the flow. Therefore, a turbulence model will be required in the simulation. The fluid in the simulation is air, the flow is three-dimensional, and there are no sources or sinks in the fluid domain. One assumption made for the simulations is that there is no effect due to gravity. The simulation, unlike the experiment, is isothermal and has no buoyancy. The flow is assumed to be incompressible, since the Mach number is much less than 0.3 (Cengel 2010).

### 4.3.2 Governing Equations

For this simulation there are several governing equations. There are a few simplifications that can be made when taking the above assumptions into account. Since the flow was assumed to be steady-state, all the transient terms can be cancelled out of the equations. The simplified continuity equation is:

$$\frac{\partial(\rho U_j)}{\partial x_j} = 0 \quad (9)$$

The simplified RANS equation, Newtonian stress tensor, and Reynolds stress are (ANSYS, INC 2013):

$$\frac{\partial(\rho U_i U_j)}{\partial x_j} = -\frac{\partial P}{\partial x_i} + \frac{\partial}{\partial x_j} (\tau_{ij} - \rho \overline{u_i u_j}) \quad (10)$$

$$\tau_{ij} = \mu \left( \frac{\partial U_i}{\partial x_j} + \frac{\partial U_j}{\partial x_i} \right) \quad (11)$$

$$-\rho \overline{u_i u_j} = \mu_t \left( \frac{\partial U_i}{\partial x_j} + \frac{\partial U_j}{\partial x_i} \right) - \frac{2}{3} \delta_{ij} \rho k_t \quad (12)$$

Where,  $\rho$  is the density,  $U_i$  is the mean velocity component,  $x_i$  is the direction,  $P$  is the pressure,  $\tau_{ij}$  is the Newtonian stress tensor,  $-\rho \overline{u_i u_j}$  is the Reynolds stresses,  $\delta_{ij}$  is the Kronecker delta,  $\mu$  is the viscosity,  $\mu_t$  is the eddy viscosity or turbulent viscosity, which must be modeled, and  $k_t$  is the turbulent kinetic energy (Wilcox 2006).

### ***4.3.3 Equation Discretization***

In order to perform calculations using the governing equations, the equations must first be discretized. For the simulations performed in this study the Central Differencing Scheme (CDS) was used for all terms, including the advection terms. This is a second order discretization, and the highest order scheme available by default in ANSYS CFX. However, for the turbulence model the advection terms were treated with the High Resolution Scheme, which is a blend between Upwind Differencing Scheme (UDS) and CDS. With this method, a small calculation is performed at each node in order to determine the amount of UDS and CDS required.

### ***4.3.4 Solver Setup***

The default fluid properties were set as air at 25°C at sea level. This resulted in having a density that was much different than the density in the experiments, since Edmonton has an elevation of approximately 670 m. Also the dynamic viscosity was slightly different due to a small temperature difference between the experiment and the set value of the air. Therefore, the density and viscosity were both changed to match the value calculated in the experiment. All properties of the simulation can be found in Table 2.

**Table 2: Final Simulation Properties.**

Fluid Properties	Values
Density	1.093 kg/m <sup>3</sup>
Viscosity	1.86e-5 kg/(m s)
Analysis Type	Steady State
Turbulence Model	<i>k-<math>\omega</math></i> with Shear Stress Transport
Advection Scheme	Central Differencing Scheme (CDS)
Turbulence Adv. Scheme	High Resolution
Residual Target	1e-5
Residual Type	RMS
Max Iterations	1500
Physical Time step	0.01s

When setting up the simulation parameters, it was important to pay attention to the fluid properties, and the time step used. Although the simulations were run as steady-state, the option for time step is effectively the under-relaxation factor for the convergence toward steady-state. When the simulations were first run it was not immediately apparent that the time step used would be important. However, once the number of nodes started to grow above about one million, it was found that the residuals, the monitored velocities, and the calculated drag force would oscillate in a predictable pattern. This may seem wrong for a steady-state solution as there should be no change with time. However, in a simulation with a higher order advection scheme, such as the pure Central Differencing Scheme, and external flow it is not out of place to see such oscillations (ANSYS, INC 2013). To check and make sure that the oscillations seen were not transient, the time step was altered and it was observed that the monitored variables did not maintain their previous oscillatory period. The under-relaxation factor can be used to help the simulation converge, if the simulation is acting unstable. Other uses for this variable are when there is poor mesh quality, large separated flow regions, or when the residual is acting in an

oscillatory manner. While the simulations in this study did have oscillatory residuals and large separated flow regions, the mesh quality was not poor. Therefore, a lower time step value was used to help smooth out convergence. While the short oscillations were removed from the residuals and the monitored variables, the large oscillations were not completely eliminated. If a low enough time step was used, the oscillations could be almost completely removed, however convergence would have taken an extremely long time. Therefore, a compromise was made between the convergence speed and an acceptable level of oscillation in the monitored variables. The oscillations were kept below 2% difference from the mean value, determined by taking the average of the last few periods of the drag force. This averaged force value is the drag value used in the analysis of the drag reduction.

The simulation was performed using a steady-state approach. While transient structures are most likely present in the actual flow, a steady numerical solution of the Reynolds-averaged equations is more than accurate enough for the goals of this study. The transient structures that are present would be averaged out over the solution. This may be the cause of some of the small oscillations seen in the monitored variables. If a transient simulation was to be done, a symmetry plane could not be used as the transient structures consisting of large turbulent vortices would most likely not be symmetric about the mid-plane.

#### **4.3.4.1 Turbulence**

The simulations were performed with the assumption that the flow around the LVTS was steady state, and the models used in the simulation were based on the Reynolds Averaged Navier-Stokes (RANS) equations. There are many turbulence models available in CFX, and this study required a turbulence model that could predict when separation was going to occur, and was fairly accurate in calculating separation zones. Therefore, the turbulence model selected was the  $k-\omega$  with Shear Stress Transport (ANSYS, INC 2013, Menter 1996, Wilcox 2006). The default turbulence model  $k-\epsilon$  was not well suited to calculating the separation zones (ANSYS, INC 2013). Also  $k-\epsilon$  has a large amount of artificial diffusion when compared to  $k-\omega$  with Shear Stress Transport. Like the  $k-\epsilon$  model,  $k-\omega$  with Shear Stress Transport uses Turbulence Kinetic Energy equation; however, it substitutes the turbulence frequency equation for the turbulence eddy dissipation. With the addition of the Shear Stress Transport a blending function is used to

merge both  $k-\varepsilon$  and  $k-\omega$  models together (Ansys, INC. 2013). In this hybrid model,  $k-\omega$  is used near the wall, which is more accurate when determining if separation will occur, and  $k-\varepsilon$  is used out in the free-stream flow. This hybrid model combines the advantages of the two turbulence models. The advantages of the  $k-\varepsilon$  model are that it is cheap and easy to implement, and highly robust. Using  $k-\varepsilon$  away from the wall is acceptable as it will not be used to calculate the separation zones that are present near the wall, which is the main disadvantage of the  $k-\varepsilon$  model. The advantage of the  $k-\omega$  model is that it has superior performance for wall-bounded boundary layers, it is good for free shear, and low Reynolds number flows. It is also suitable for complex boundary layer flows under adverse pressure gradient and separation (i.e. external aerodynamics).

#### 4.3.4.2 Boundary Conditions

The boundary conditions (BCs) were set to match the wind-tunnel. No-slip wall conditions were used on the top wall, side wall, bottom wall, and the faces of the model. A symmetry boundary condition was placed on the symmetry plane. The inlet was set as a constant velocity inlet, which was set to 2.34 m/s with medium turbulence (5%). The outlet was set as an Average Static Pressure condition (i.e. zero velocity gradient) with a relative pressure of 0 atm.

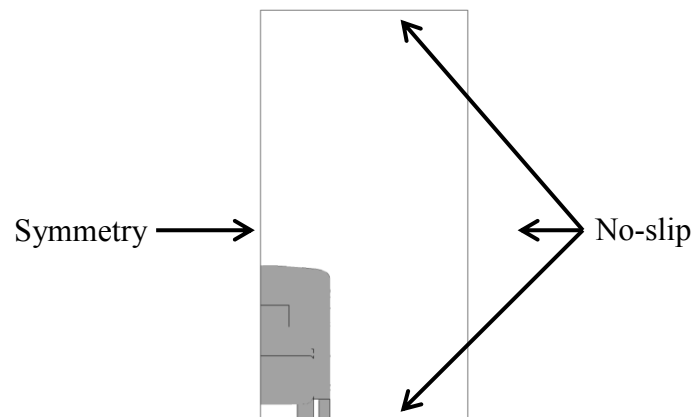


**Figure 28: Boundary conditions, front view.**



**Figure 29: Boundary Conditions, side view.**

Figures 28 and 29 show the boundary conditions applied to the fluid domain.

#### **4.3.4.3 Solver Control**

ANSYS CFX has three options for advection scheme: Upwind, High Resolution or Specified Blend Factor. With specified blend factor a value is set between 0 and 1, where 0 corresponds to the upwinding differencing scheme (UDS) and a value of 1 corresponds to the central differencing scheme (CDS), any value between 0 and 1 would result in a mixture of the two. CDS is a second order discretization scheme, while UDS is first order. One possible issue with CDS is that it may not behave naturally and may cause the solution to be unbounded. This means there may be non-physical oscillations in the final solution. UDS does not have this problem as it adds significant artificial diffusion to the solution, which smooths out the results. The boundedness issues of CDS can be overcome with a highly refined grid. High Resolution is a program controlled mixture of the two different schemes, which automatically adjusts the specified blend factor at each node. It attempts to keep the blend factor as close to 1 as possible without introducing new extrema. This method however does not give the user full control over which advection scheme is employed, therefore it was not used and a manual value for the specified blend factor was specified in the final simulations. In order to start the simulations UDS was used in order to achieve convergence early on. This helped the solution to converge, so that the results could be analyzed to find where mesh refinement was required in the early stages of setting up the simulation. Once the final grid was found, a specified blend factor of 1 was specified to ensure that pure CDS was used at all nodes in the solution.

The turbulence advection scheme has two options: First Order, and High Resolution. Like the momentum advection scheme, First Order uses the UDS for the turbulence equations and High Resolution uses a mixture of UDS and CDS for these equations. Unlike in the momentum equations, a specified blend factor cannot be set. Therefore, High Resolution was used in order to attain the highest accuracy possible.

The maximum number of iterations is not relevant to this study, as the solution was manually stopped once a stable oscillation was reached by the monitored variables. The residual target, however, had to be lowered in order to allow the solution to continue uninterrupted. The residual target was set to  $1.0e-5$ , and the norm of residual used was the Root Mean Square (RMS). While none of the simulations reached this convergence criterion, the largest residual did stabilize at about  $1.0e-4$ .

As mentioned previously the time step was adjusted to a value which gave reasonably quick convergence and did not show too much oscillation in the solution. By default the program has an auto-timescale control which multiplies some length scale of the domain by the average velocity in the domain. The default length scale used is the cubic root of the fluid domain volume, and the velocity used is the inlet velocity (as this is the only place a velocity is defined at the start of the run). This auto-timescale does not give the user full control over the numerical time scale of the solution. Therefore, the time scale control was set to the type “physical scale” and to a value of 0.01s. This complies with the suggestion from the ANSYS CFX documentation that this physical timescale not be set above the advection timescale, which was  $\sim 0.3s$ .

#### **4.3.4.4 Output Control**

In order to monitor the solution as it progressed, monitoring points were used. The calculated drag force on the body was one such monitoring value as this is the variable of interest in this study. Other monitor points consisted of watching the velocity at certain points around the model. All the monitored variables served two purposes. The first, to see if the solution was converging, and when it was converged. The second, to see where possible mesh refinement was required, and which parts of the flow were most affected by any mesh refinements.

### **4.4 Verification**

#### ***4.4.1 Estimated Order of Truncation***

When the governing equations are discretized using the Taylor series, an error is introduced known as the truncation error. This happens because only a few of the leading terms from the Taylor series are used, and thus the remaining terms that are dropped constitute the error between the exact solution and the approximated solution. A test can be performed to determine or

estimate what is the order of the simulation. This order can then be compared with the order of discretization used when discretizing the differential equations. This test is useful in code validation, and to see how accurate the simulation was. This estimated value for the order of the simulation will be referred to as the  $p$ -value.

To perform this test, three simulations are required. Each simulation is identical except for one setup variable which is systematically altered between each of the simulations. For example, the mesh from the first case is refined twice by the same amount each time, the first unrefined case, the intermediate case, and the final refined case are the three cases which are used for this test. The rate at which the setup variable is altered is known as the refinement rate or expansion rate, depending on the variable being tested, represented by  $a$ .

$$a = \frac{\Delta x_1}{\Delta x_2} \cong \left( \frac{N_2}{N_1} \right)^{\frac{1}{3}} \quad (13)$$

$\Delta x_1$  = coarse element length

$\Delta x_2$  = refined element length

$N_2$  = Number of nodes in refined case

$N_1$  = Number of nodes in coarse case

Here,  $a$  is being referred to as the refinement rate since the mesh is being refined. Normally for calculating the refinement rate the element length is used, however for the simulation performed in this study, an unstructured grid was used to produce the mesh and therefore a single element length cannot be used to represent the entirety of the mesh. Therefore, an approximation by the cube root of the number of nodes will be used instead. This ratio will result in a more accurate value for the refinement rate (Roache 1997).

This test is normally done to check for mesh independence, however, it can be extended to test other variables as well, such as the domain size. When testing for domain size effect, the above rate of change equation can be modified as shown below.

$$a \cong \left(\frac{A_2}{A_1}\right)^{\frac{1}{2}} \quad (14)$$

$A_2$  = Cross-Sectional Area from Larger Area case

$A_1$  = Cross-Sectional Area from Smaller Area case

Here in Eq. 14,  $a$  is being referred to as the expansion rate since the domain is being expanded. Like before in Eq. 13, the refinement/expansion rate is being approximated by a ratio, however this time the ratio is of characteristic domain lengths, instead of element lengths. This is why the square root of the ratio of cross-sectional areas is being used instead of a cube root of the number of nodes.

Once the three simulations are completed, the results are analyzed and the value of interest is recorded. These values are then plugged into Eq. 15 in order to calculate the  $p$ -value ( $p$ ):

$$p = \frac{\log\left(\frac{\phi_{\Delta x_2} - \phi_{\Delta x_1}}{\phi_{\Delta x_3} - \phi_{\Delta x_2}}\right)}{\log(a)} \quad (15)$$

$\phi_{\Delta x_n}$  = the value of interest ( $n$  represents which case it's from 1 for coarse, 2 for medium, and 3 for fine)

Here,  $a$  represents either the refinement rate or expansion rate. Coarse represents the simulation with the lowest number of nodes or smallest cross-sectional area out of the three test cases used, and fine represents the simulation with the highest number of nodes or the largest cross-sectional area.

For this study, since the order of discretization of the advection scheme was 2 (Central Differencing Scheme) and the order of the turbulence model fell between 1 and 2 (High Resolution), then the  $p$ -value for this study should fall between 1 and 2 with a bias towards 2. If the  $p$ -value does end up close to 2, then the simulation's mesh has been sufficiently refined, and any further refinement will only reduce the truncation error in the simulation. This condition is called grid or domain independence.

With the  $p$ -value obtained, a better estimate of the exact value can be determined using the following equations, which correspond to Richardson Extrapolation.

$$\phi_{exact} \approx \phi_{\Delta x_3} + \epsilon_h^d \quad (16)$$

where,

$$\epsilon_h^d = \frac{\phi_{\Delta x_3} - \phi_{\Delta x_2}}{a^p - 1} \quad (17)$$

$\epsilon_h^d$  is the error due to discretization (Ferziger 2002).

## 4.5 Sample Results

A full analysis of the simulation results and of the grid and domain independence will be shown in Chapter 5. Here, some sample results are presented to demonstrate the simulation.

A few examples of a typical solver output are shown below in Figs. 30 and 31.

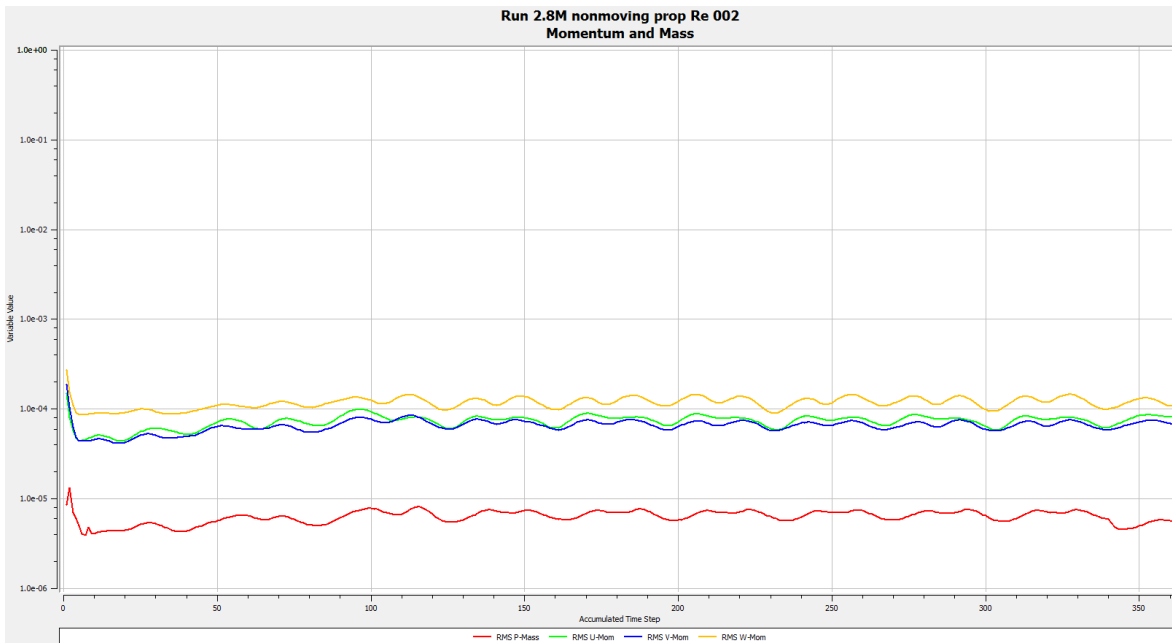


**Figure 30: Residual output for simulation without deflector.**

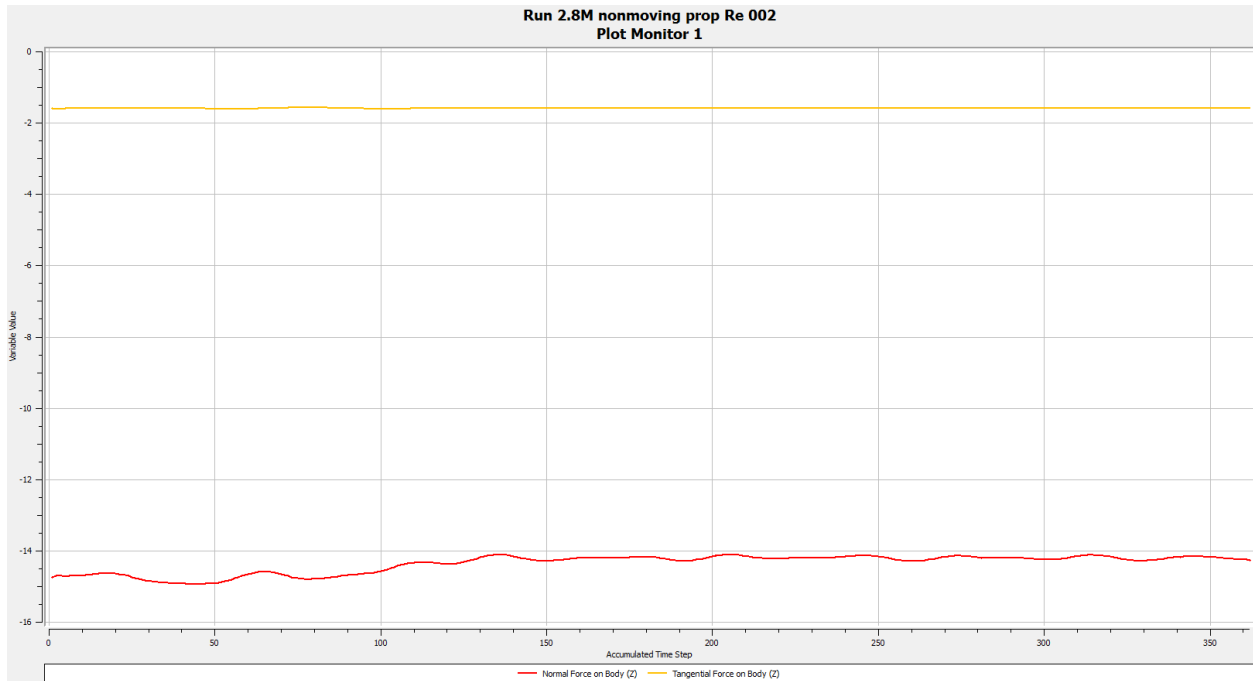


**Figure 31: Force plot for simulation without deflector.**

Figures 30 and 31 show the residual plot and the force plot, respectively, for the simulation without a deflector. From these figures it can be seen that the simulation was run for a significant amount of time to allow the residuals and the drag force to converge about some constant value. The residuals and the forces start very close to their final values because all simulations used previous results as initial conditions, in order to reduce calculation times. The residuals shown are the root mean square, and not the maximum residual in the domain. The force plot shows two different forces, they are the normal force, or the pressure drag, and the tangential force, or the drag associated with the skin friction. The total drag is the addition of these two different drag forces. The skin friction drag is much smaller than the pressure drag; skin friction is only 10% of the total drag, while pressure drag makes up the other 90%. This was expected since this is a study of a bluff body.

Figure 32 shows the side view of the LVTS with no deflector, and Fig. 33 shows the top view of the LVTS with deflector. Pressure contour plots help show how the flow is interacting with the body of the model. High pressure zones indicate areas where the flow is hitting the model at large angles, for example at a stagnation point, while low pressure zones indicate possible areas of separation.

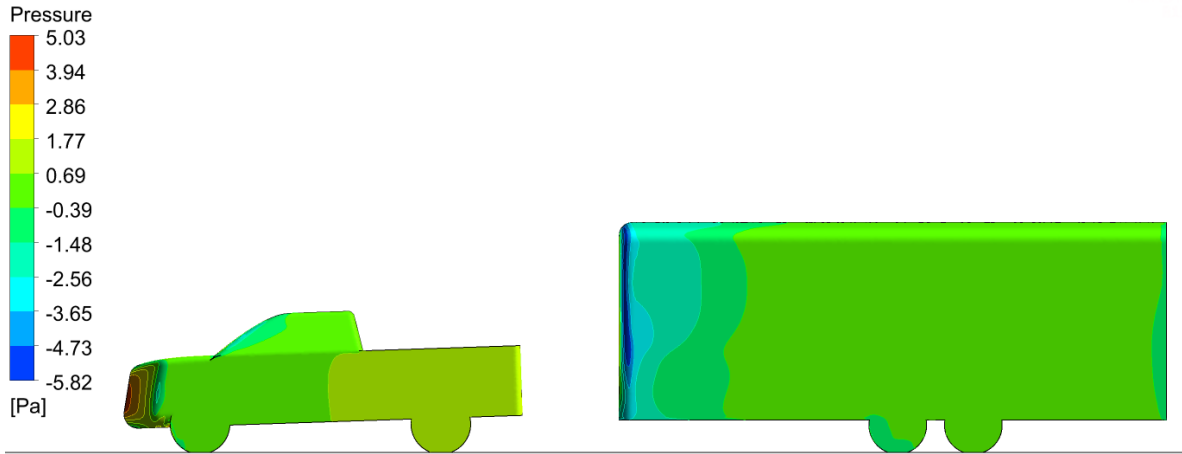


**Figure 32: Side view of pressure contour on the surface of the LVTS with no deflector**

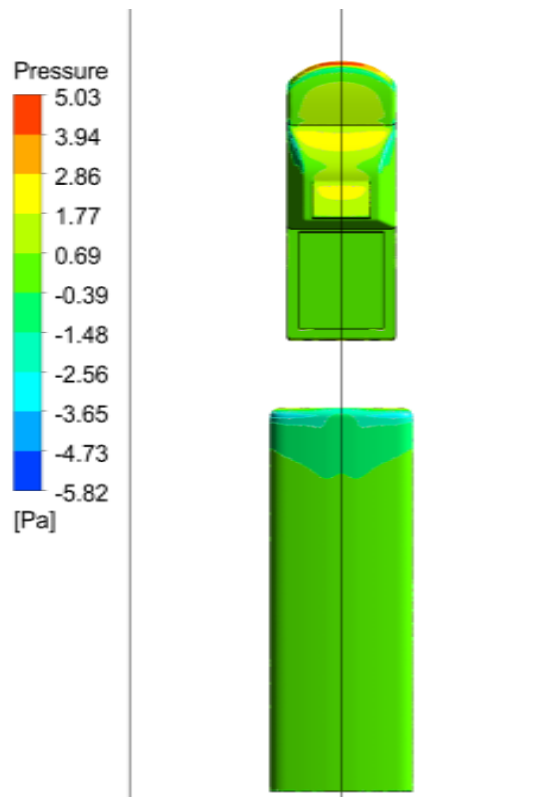


**Figure 33: Top view of pressure contour on the surface of the LVTS with deflector.**

## **5. Results and Discussion**

In this chapter the results of the wind-tunnel experiments and computer simulations will be presented and discussed. First, the Reynolds number and its effect on both the experimental results and simulation results will be discussed. Next, the blockage effect, domain size, and mesh influence on the simulation are analyzed. Following this, the results of the experiment and simulation are compared with each other by comparing the smoke streaklines with the simulation streamlines, where an augmented reality image was created by overlaying the streamlines on top of the photographs from the experiment. Further comparisons were made by creating a velocity vector plot of the experimental flow through the use of ICV, which was compared to the simulation results. Pressure contours calculated in the simulation are studied as they give a good visual representation of the effect of the deflector. The simulation had a different flow topology which showed a vortex pair present at the front of the trailer, and this will be discussed here. Next, in the simulation a moving ground-plane and its effect on the drag with and without the deflector were studied. Finally, vector profile lines from the simulation and ICV were compared directly by overlaying them on top of each other.

### **5.1 Reynolds Number Effects**

In the preliminary experiments carried out in Chapter 2 an unexpected flow pattern was found, namely a separation zone on top of the truck's hood in front of the cab. Figure 34 shows the flow of air at a Re of 15,800 where the separation can clearly be seen.



**Figure 34: Hood separation,  $Re = 15,800$ . Flow in right to left direction, contrary to convention.**

Several attempts were made, as reported in Chapter 2, to reduce the size of the separation zone as its presence could be affecting the flow. Without any success in physically tripping the flow from laminar to turbulent over the hood and have the flow stay attached, the only option left was to increase the  $Re$  number of the flow. Therefore, the air velocity in the experiment was increased by a factor of 2.8. The simulation air speed was never increased due to a resource limitation. It was immediately apparent that the hood separation had been reduced significantly. Figure 35 shows the new flow at the higher  $Re$  of 44,400.



**Figure 35: Hood separation reduced,  $Re = 44,400$ .**

This supported the conjecture that the hood separation was merely a Reynold's effect. As for the other flow characteristics, such as the trailer face stagnation point, and the separation zone on the top of the trailer they were found to be unchanged when the  $Re$  number was increased. The cause for this is that  $Re$  has less of an effect once the flow becomes fully turbulent, as is well known for turbulent flows. This is the case once the flow separates from the top of the truck and becomes turbulent.

The presence of this separation bubble draws attention to the influence of the great Reynolds number variation between the lower  $Re = 15,800$  of the model compared to the much higher  $Re = 5.3$  million of a typical full-scale LVTS. It is not possible to be absolutely certain of the relevance of the model visualization results to the full-scale, but only a qualitative modeling equivalence can be expected. Therefore, although the results for the model are not quantitatively expected to precisely mimic the full-scale, the study with models can be useful as a guide to what innovative drag reduction devices should be pursued in a higher  $Re$  wind-tunnel study of full-scale. Preliminary study of models is less expensive and allows easy modification to drag reduction device geometry.

### 5.1.1 Effect of Reynolds Number on Simulation Drag

Throughout this study the air speed and properties were varied in the simulation. In order to determine the Re, early simulations used the default fluid properties of the solver with an air speed of 2 m/s. These settings were used to establish a preliminary mesh, and gain results which could be used as initial conditions for later simulations. When the Re was altered it was found that the drag of the model was influenced slightly. This was expected to happen as it was expected that although the flow was turbulent, the flow was not yet Re independent.

For both test cases, with and without the deflector, the Re was increased from 14,900 to 15,800 by adjusting the speed and properties. The  $C_d$  in the case without the deflector was reduced from 1.06 to 1.02, and with the deflector it was reduced from 0.88 to 0.84. The changes are summarized below in Table 3.

**Table 3: Fluid Properties and Drag Coefficients Changes For Different Settings Between Original Simulation and Actual Lab Values.**

	Default Re = 14,900	Actual Lab Re = 15,800	Change 6%
Speed (m/s)	2	2.34	17%
Density (kg/m <sup>3</sup> )	1.185	1.093	-8%
Viscosity (kg/(m s))	1.83e-5	1.86e-5	2%
$C_d$ without deflector	1.06	1.02	-4%
$C_d$ with deflector	0.88	0.84	-5%

With an increase in the Re the  $C_d$  was reduced in both cases. This shows that the simulation is not quite Re independent, since the  $C_d$  changes slightly with the Re. It is expected that once the Re is high enough, the  $C_d$  will stop changing unless there is a “drag crisis” sort of behavior, as happens for a cylinder flow (Cengel 2010). However, a “drag crisis” is not expected since the separation points are fairly well fixed except on the truck hood, which has been shown to have

little effect, and perhaps on the trailer shoulder. The impact of drag reduction on fuel consumption will be discussed later in Section 5.7.3.

## 5.2 Blockage Effect, Domain and Mesh Independence

An important aspect to consider in both wind-tunnel experiments and computer simulations for bluff bodies is the effect due to blockage. Since there is limited area for the flow to go through when the model is present, part of the area is blocked off, causing the fluid to accelerate as it passes around the body. This artificially caused the drag force to go up, as it will later be shown that by reducing the blockage the drag force was reduced. Since the value of the drag is affected by the blockage, it was important to understand how large of an impact it had on the flow around the model. The blockage ratio,  $\beta$ , for the experiment was 11.0%, this value is based on the combined projected frontal area of both the truck and trailer. This projected area was used because it was the same method used in a previous study (Hucho 1998).

### 5.2.1 Blockage in Computer Simulation

In the simulation the effect of blockage was tested by systematically increasing the domain width and height. This will be referred to as the domain independence test. The air speed and fluid properties for this test are shown below in Table 4.

**Table 4: Fluid Properties for Domain Independence Test.**

Fluid Property	Value
Velocity	2 m/s
Density	1.185 kg/m <sup>3</sup>
Viscosity	1.81e-5 kg/(m s)

These fluid properties were different from the parameters used for the final simulation since the domain independence analysis was completed before ICV experiments were performed. The  $Re$  of these tests was 14,900.

In order to test the effect of blockage on the  $C_d$  of the model, several simulations were run with varying sizes of the cross-sectional area of the domain. This was done by first increasing the domain's width in five steps by 10% each step, then the domain's height was increased in the same fashion. The final blockage ratio reached was 4.2%. The  $C_d$  was calculated for each of the ten simulations, and the results have been plotted in Fig. 36.

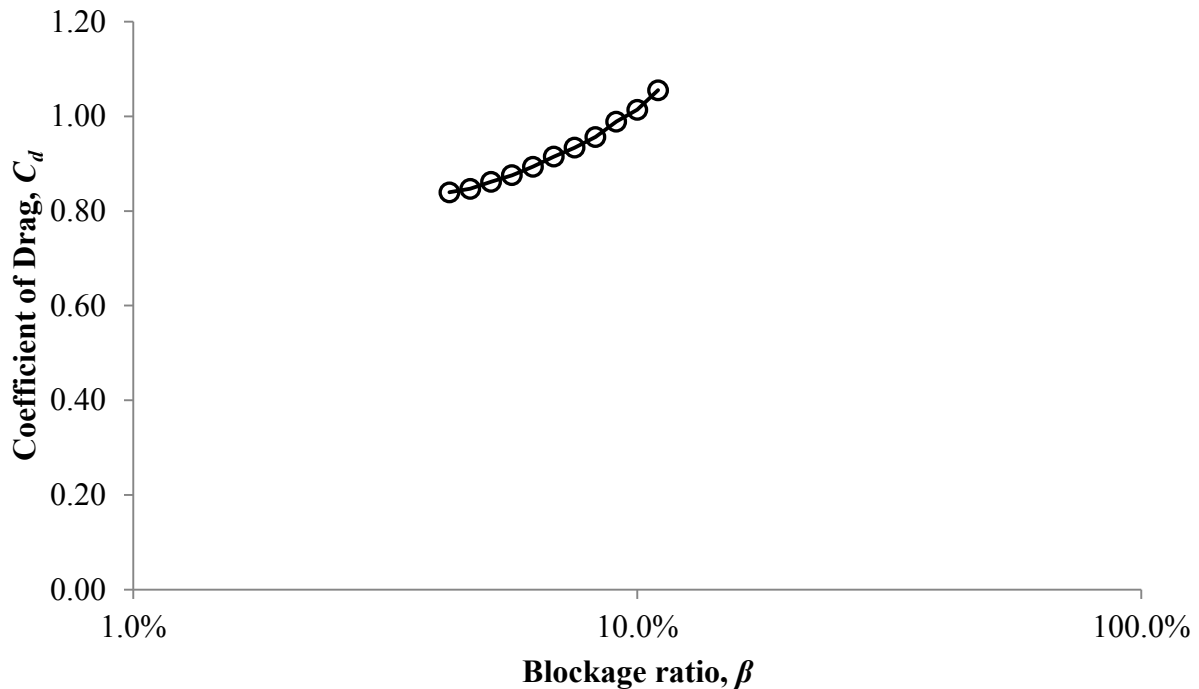


**Figure 36: Coefficient of Drag vs. Blockage Percent, for varying domain sizes.**

From this figure, it can be seen that the drag force is trending downward as the blockage is being reduced. This was expected as the original blockage ratio was quite high at 11%. The  $C_d$  with a  $\beta$  of 11% was 1.06 and the  $C_d$  after the  $\beta$  was reduced to 4.2% was 0.84. This represents a 20% decrease in the  $C_d$  due to blockage alone. The effect of  $\beta$  was not tested for the model with a deflector. It is expected to behave the same as the model without the deflector, because the deflector did not change the blockage ratio.

The expected reason this happens is that when the blockage ratio is high, the flow is forced to accelerate to higher speeds as it flows around the model, as opposed to when the blockage ratio is less. The higher speeds give an artificially high local velocity that produces more drag.

### 5.2.2 Domain Independence and Richardson Extrapolation

As explained in Chapter 4, in order to verify that a simulation is independent of a setup variable, in this case the domain's cross-sectional area, the  $p$ -value must be calculated and compared to the order of truncation used to discretize the governing equations. To perform this test three of the test cases from Section 5.2.1 above were selected such that the first and last cases were included. The values used are shown below in Table 5.

**Table 5: Test Values for Domain Independence.**

Case	Blockage, $\beta$	$C_d$
1	11%	1.06
2	6.8%	0.915
3	4.2%	0.839

The  $p$ -value was calculated to be 2.6 using Eq. 15. The order of truncation used on the governing equations was between 1 and 2, therefore an acceptable range would have been between 0.8 and 2.2. While the  $p$ -value was found to be outside this range, it must be noted that to find a  $p$ -value so close to the acceptable range is quite difficult to achieve and shows that while the simulation may not be domain independent, it is very close to becoming independent. In order to further reduce the  $p$ -value, the domain's cross-sectional area must be increased further.

With the simulation's order calculated Richardson Extrapolation can be used to better estimate what the exact value of the  $C_d$  would be if the  $\beta$  was reduced to zero. The expansion rate used was 1.27, which corresponds to a 62% increase in the cross-sectional area for each simulation. With the expansion rate and  $p$ -value calculated, Eq. 17 was used to calculate the discretization error, which was found to be -0.088. Using Eq. 16 and the recently calculated error value, an estimate of the  $C_d$  for an infinite domain with blockage approaching zero was calculated as 0.75. This extrapolated estimate could be further improved, if a  $p$ -value corresponding to domain independence could be reached.

### 5.2.3 Mesh Independence

Similar to domain independence test, the mesh can be tested to see if the simulation is grid independent. This was done using three differently refined grids, which were calculated so that the refinement rate used was approximately 1.07. The simulations with and without the deflector were tested for grid independence. The number of nodes and the resulting  $C_d$  are shown below in Table 6.

**Table 6: Mesh Independence Test Results With and Without a Deflector.**

	Nodes	$C_d$
Without Deflector	2,459,986	1.025
	1,999,781	1.028
	1,636,730	1.025
With Deflector	2,751,445	0.847
	2,227,233	0.845
	1,810,199	0.842

The values above along with Eqs. 15, 16, and 17 were used to calculate the  $p$ -value, the discretization error, and the estimated value for the  $C_d$ .

For the case without the deflector it was found that a  $p$ -value could not be estimated, as the results were not asymptotically trending. Therefore, it cannot be said that the simulation without the deflector is grid independent. However, the simulation results are not changing much between runs, when the number of nodes was increased by 23%, the  $C_d$  only changed by 0.3%. Therefore, while the simulation may not be grid independent without the deflector, it has been shown that the simulation results are not changing significantly with changes in mesh and the discretization error is small.

On the other hand for the case with the deflector a  $p$ -value of 5.4 was calculated. Like the domain independence test, the  $p$ -value here falls outside the prescribed range of 0.8 – 2.2 for this to be considered grid independent. Using this  $p$ -value, in spite of it being outside the valid range, the discretization error was estimated to be 0.005, resulting in an estimated exact  $C_d$  of 0.85. This would be the exact  $C_d$  for a wind-tunnel with 11% blockage, as in the experiment

### **5.3 Streaklines and Streamlines**

To study the flow in both the wind-tunnel experiments and the computer simulations, one method used was to compare the smoke streaklines of experiment with the streamlines of the simulation. This gave a good way to compare the two together on a qualitative basis. Later, Image Correlation Velocimetry was used to quantitatively compare the flow in a specified region between the truck and the trailer. The first case that was studied was the model without the deflector. This was done to gain an understanding of the flow in the default setting. This also set a reference point which could be used to compare the flow once the deflector was in place.

#### ***5.3.1 Flow Separating from Truck Roof***

From the preliminary experiments, covered in Chapter 2, it was first thought that the flow separating off the roof of the truck was stagnating on the front face of the trailer. This however was found to be incorrect once the simulation results were studied. It was found that the flow separating from the truck's roof was not stagnating on the trailer, but possibly reattaching on the back of the truck. This helped show that the stagnation zone was a result of the mean stream flow impinging on the front face of the trailer once it passed over the roof of the truck. The centerline streamlines showing the flow around the model can be seen in Fig. 37.

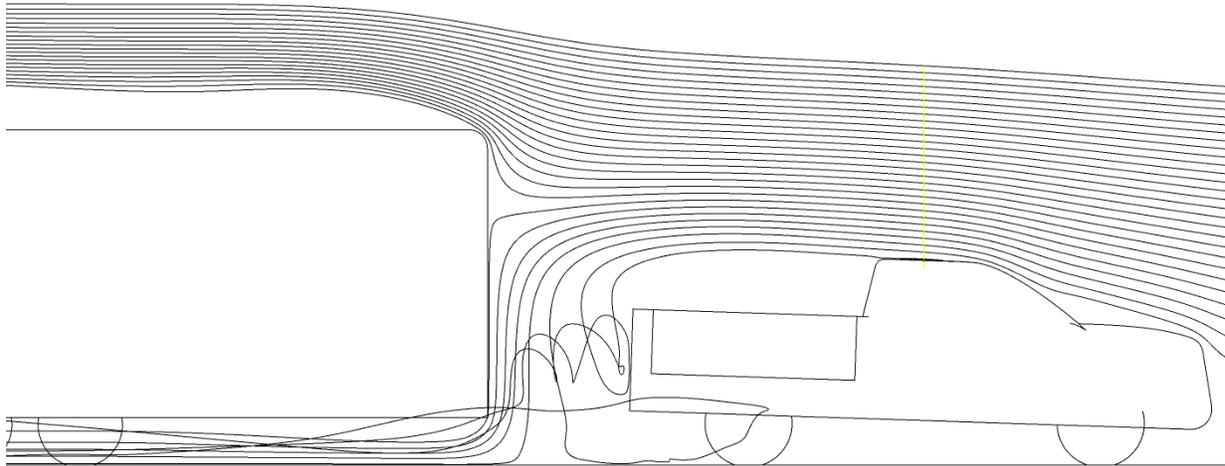


**Figure 37: Main flow streamlines over truck with no deflector,  $Re = 15,800$ . Flow in right to left direction, contrary to convention.**

From Fig. 37 it can be seen that the streamline closest to the roof of the truck, once passing over the box of the truck, appears to flow downwards and possibly reattach to the truck. If the mid-plane streamline that intersects the stagnation line on the face of the trailer was traced upstream, it shows that the flow came from the free-stream and not from the flow separating off the truck. Figure 37 also shows two separation zones on the trailer, the first is on the top of the trailer after the leading edge, and the second is on the bottom after the bottom leading edge. The separation on the bottom is better shown in Fig. 38.

Between the truck and the trailer a channel was created through which the air could flow from the mean stream flow above the truck to under the trailer. Figure 38 below shows the flow streamlines for the air channel selected from Fig. 37.

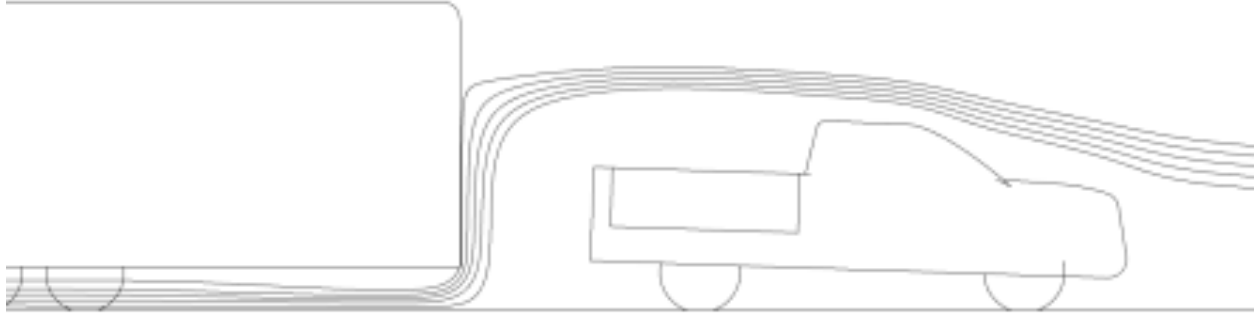


**Figure 38: Simulation featuring streamlines creating a flow channel between the truck and trailer.**

Figure 38 shows the feature streamlines coming from the mean stream flow, which stagnate on the front of the trailer, and then proceed to flow under the trailer. This flow channel is an important characteristic that defines the flow over the LVTS.

### ***5.3.2 With Deflector***

A small wedge deflector was placed on the roof of the truck with the intention of reducing the drag of the model by attempting to remove the stagnation zone from the front of the trailer and integrating the truck with the trailer's aerodynamics. Successful removal of the stagnation zone created significant differences in the flow around the model. The separation zone in the box of the truck was made larger, and the channel flow described earlier was removed.

#### **5.3.2.1 Stagnation Zone**

The stagnation on the front of the trailer was drastically altered by the addition of a simple deflector on the roof of the truck. Instead of the flow stagnating on the front of the trailer, it was deflected upward over the trailer. By removing this stagnation zone from the front of the trailer, the large pressure drag associated with it was removed resulting in a reduction in drag. The deflector used was very simple and no attempt was made to optimize its design. Therefore, it is hypothesized that the reduction in drag could be further improved by tuning the deflector to

better deflect the flow, and to have the flow reattach closer to the front leading edge of the trailer. Figures 39 and 40 below show the streamlines and streaklines, respectively, for the new flow.

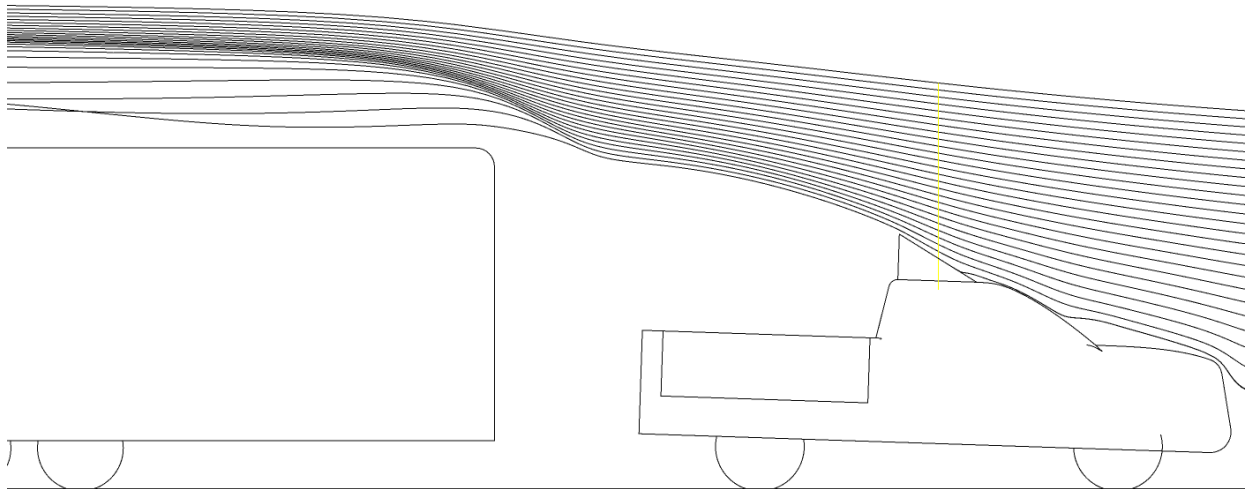


**Figure 39: Simulation streamlines of mean stream flow over model with deflector. Flow in right to left direction, contrary to convention.**



**Figure 40: Experimental streaklines of mean stream flow over model with deflector.**

By comparing Figs. 34 and 37 with Figs. 39 and 40 it can be seen that the stagnation point has been removed from the front of the trailer. One difference between the cases with and without a deflector is that the simulation found a completely different topological solution to the flow around the front of the trailer, which led to a difference in the streamlines around the trailer and the appearance of the suspicious looking cusp upstream of the trailer shoulder that is not seen in the streakline photograph. This can be seen in Fig. 39 above the front leading edge of the trailer where there is a compression of streamlines. This will be discussed later. These photos only show a two dimensional view, however, they give good insight into how the deflector is altering the flow.

### ***5.3.3 Streamline and Streakline Comparison***

From the figures shown in the previous section showing the streamlines and streaklines, an overlay was produced which directly compared them. The  $Re$  used in these images is 14,900.



Figure 41: Streamline, streakline overlay with no deflector. Flow in right to left direction.  
Re = 14,900.



Figure 42: Streamline, streakline overlay with deflector. Flow in right to left direction. Re = 14,900.

Figures 41 and 42 show an augmented reality with the simulation streamlines, shown in red, overlapping the bluish-white smokewire streaklines. The figures show that the streamlines match the streaklines reasonably well, particularly in the case without the deflector. For this case the stagnation point on the front face of the truck and trailer appear the same.

With the deflector it can be seen that there is a large impact on the overall flow. In comparing the experimental streaklines with the simulation streamlines there appears to be a discrepancy between the two at the front top leading edge of the trailer. Here there appears to be a “kick up” in the streamlines as they move over the top leading edge. Another part of the flow that the simulation captured well was the separation located on the hood of the truck when compared to the experiment’s hood separation.

## **5.4 Velocity Vector Plot**

As discussed previously, ICV was used to analyze the flow in the experiment, and to produce a velocity vector plot which could be used to compare with, and attempt to validate the computer simulation. Three tests were run using ICV, the first test was with no model in order to check that the ICV method was working properly, and to see how much buoyancy was present in the experiment. The second and third tests included the model and were run without and with the deflector, respectively.

### ***5.4.1 No Model***

In order to test the ICV method and check that it was calculating the flow’s velocity correctly, it was tested by running the experiment without the model present. Additionally, this test could also be used to calculate the buoyancy. To check the calculated value of velocity the mean stream velocity was measured by a Pitot-static probe upstream of the test region. Shown in Fig. 43 below is the vector plot produced by ICV for no model present in the wind-tunnel. The velocity values have been nondimensionalized with the free-stream velocity of 2.34 m/s. The flow is in the right to left direction, contrary to convention.

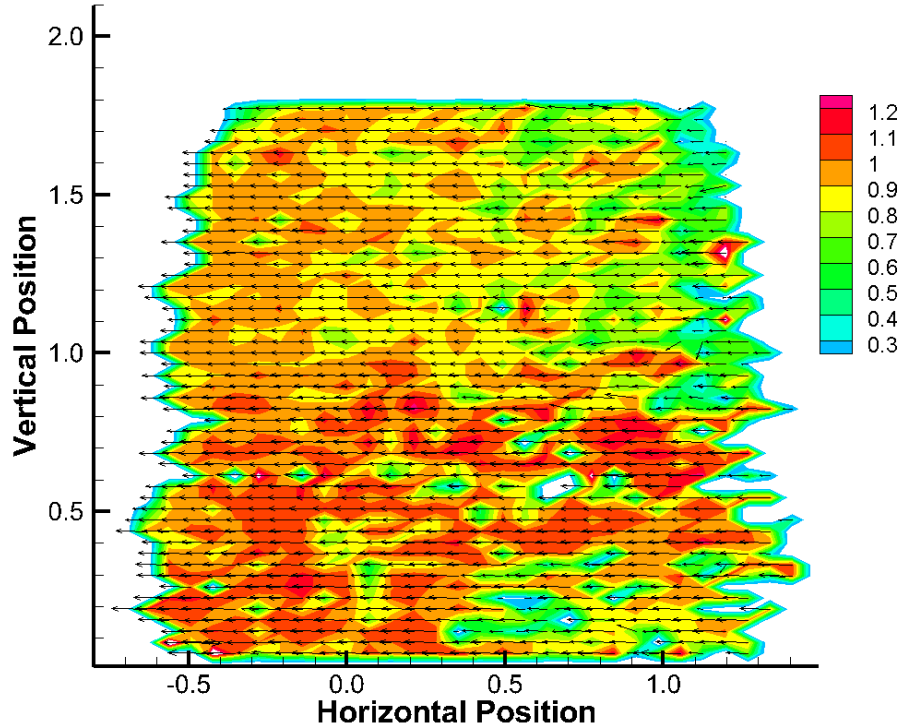


**Figure 43: Image Correlation Velocimetry, vector plot of mean stream flow (Positions nondimensionalized with the trailer height of 115.26 mm, and velocities nondimensionalized with free-stream Pitot-static probe measurement).**

In Fig. 43 the horizontal position of 0 is where the front face of the trailer is located and this is 0.31 m from the start of the wind-tunnel, and the vertical position of 0 is the ground-plane. All distances have been nondimensionalized with the trailer's height, and the velocity has been nondimensionalized with the measured free-stream velocity. From the data in Fig. 43, it can be seen that the data is not uniform, and tends to have a higher velocity closer to the bottom of the tunnel. It is not known why the velocity is higher on average towards the bottom of the tunnel. It was expected that the velocity profile across and along the wind-tunnel would be more uniform than the flow shown in Fig. 43. It should be noted at this point that the ICV data does not reach the top of the wind-tunnel. The middle of the wind-tunnel corresponds to a vertical position of approximately 1.3 which is well within the domain of the data. Data from the vector plot was extracted and plotted in Fig. 44. The data was selected using vertical polling lines at different horizontal locations.

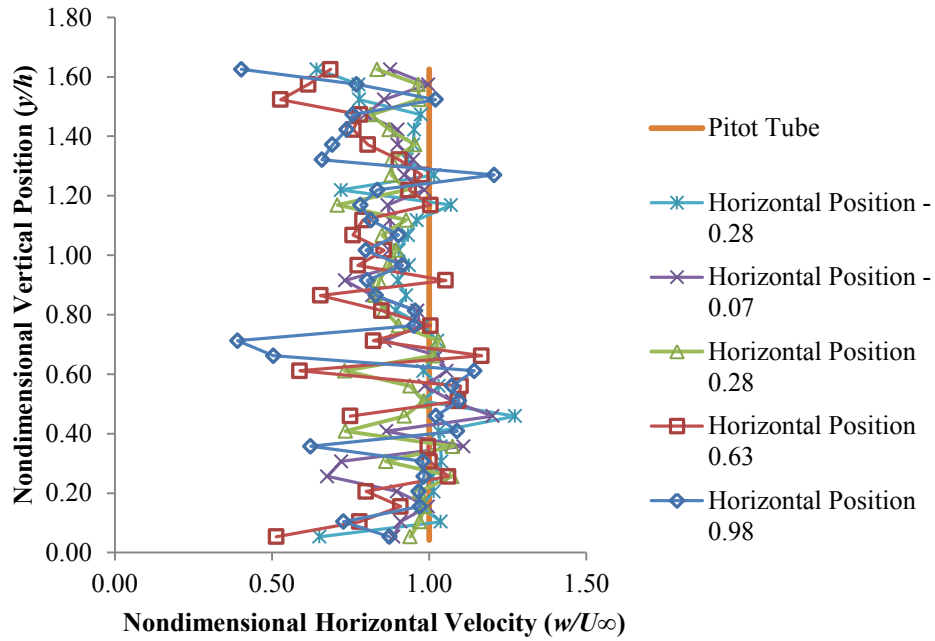


**Figure 44: Nondimensional horizontal velocity, mean stream flow 2.34 m/s.**

The lines correspond to the horizontal positions as labelled in the graph's legend above. The averages for each line are summed up in Table 7 below.

**Table 7: ICV Calculated Free-stream Velocity for Various Horizontal Locations, Nondimensionalized Velocity with Pitot-static Probe Velocity.**

Horizontal Location	Averaged Nondimensional Velocity
Pitot-static probe	1.0
-0.28	0.95
-0.07	0.92
0.28	0.91
0.63	0.85
0.98	0.85

From this data it can be seen that the ICV method is not very accurate with an under-evaluation of the free-stream velocity by up to 15%, which pixel error alone could not account for. In previous work with the ICV system it was found that with well-defined streaklines the error could be reduced to as low as 4% (Apps 2001). On the other hand, it was found that when the smoke was mixed rapidly and became a cloud of smoke rather than distinct streaklines, the error could be as high as 15%. The data from Table 7 show that the ICV method appears to be more accurate along the left side of the investigation region, since the average was closer to the expected value of 1. The averages for the other lines were found to be within error. The individual data points from Fig. 44 show that there was a large amount of noise in the data which was approximately  $\pm 0.3$  from the average. This was one large downside of this method in this study.

The data in Table 7 show that the flow accelerated by 12% through the ICV investigation region, this was much higher than expected. A small amount of acceleration was expected to be present due to conservation of mass and the growth of the boundary layer displacement thickness. Therefore, a calculation was performed using the displacement layer thickness calculation for both a laminar and turbulent boundary layer. It was found that the maximum thickness change in the boundary layer would only account for a 2% speed-up in the flow between the start and the end of the ICV investigation region.

The evidence shows that the ICV method is not highly accurate in measuring the velocity magnitude; however, the purpose of this method was to help guide the study and compare it with the CFD simulations. From the simulations more detailed quantitative results could be found. Also note that the pattern of the streaklines obtained directly from the photographs could be compared with the simulations.

#### **5.4.1.1 Buoyancy**

The buoyancy velocity in the wind-tunnel, a vertical velocity due to the heating of the air by the smokewire (sometimes called convection velocity), had to be quantified in order to account for its influence on the flow around the model. The data presented in Fig. 43, in the previous section, were used to analyze the buoyancy. The vector plot was sampled three times along the horizontal

direction at different vertical locations. This was done to check if the buoyancy varied while traversing downstream.

The buoyancy velocity was found to be so small that it was lost in the resolution of the image; this caused it to appear bi-modal. This happened because the smoke was found to rise either zero or one pixel between the red and blue flash, which corresponds to a velocity of 0 m/s or 0.021 m/s. Other values between these were interpolated by the ICV program.

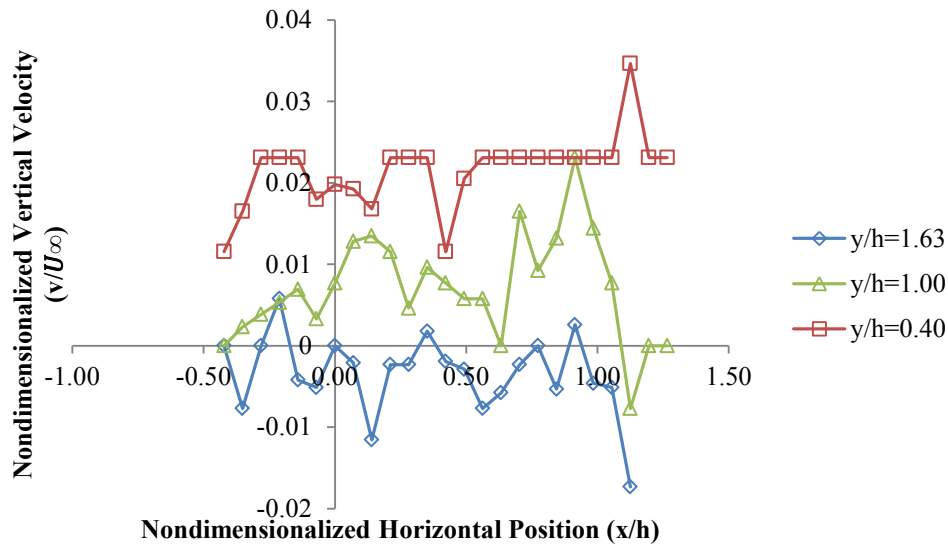


**Figure 45: Nondimensionalized vertical velocity showing the buoyancy with no model present.**

From Fig. 45 it can be seen that there is no constant value for the buoyancy. Much like the horizontal velocity in Fig. 43 there was noise in the data. It was found that the buoyancy was on the same order as the pixel error, defined earlier. The line corresponding to  $y/h = 0.40$  shows an average value of 0.021 m/s. If this was the buoyancy it is still only 2% of the mean stream flow velocity. Since the buoyancy is so small compared to the vertical velocities seen in the ICV photos, when the model is present, the effects of buoyancy were neglected.

#### **5.4.2 Model Without Deflector**

When ICV was used on the model without deflector there was a breakdown in the method due to a region of accelerating flow. However, flow outside this region was unaffected and gave results which could be analyzed. The region which caused the ICV method to break down was at the top

leading edge of the trailer where there was high curvature in the streamlines. There were two reasons for this break down. The first is that the flow was accelerating, and the ICV method works on the assumption that the flow is not accelerating (and if it is the acceleration is very small). The second reason is that in having such a high curvature in the flow the smoke streamline rotated and diffused, as discussed in Section 3.2.2.1. Since the smoke was diffuse, the ICV method did not have a pattern in the smoke on which it could correlate. Therefore, in the ICV results a large dead zone was present around the top front leading edge of the trailer. This can be seen in Fig. 46.

From Fig. 46 it can be seen that a large white region is centered at the coordinates 0.0, 1.0. This corresponds to the top leading edge of the trailer where the flow is accelerating. This acceleration affects the ICV calculations for a large radius around the trailer's corner. Directly outside the white region is a bright green zone, this zone is believed to not be the correct velocity at that point, as the calculated values in the green zone are being influenced still by the accelerating flow. The zone which can be used for analysis is outside the green zone, which are the yellow, orange and red zones. The vectors that are below the vertical position of 0.5 are thought to be accurate as they are outside the apparent radius of influence from the trailer's corner.

From the simulation a vector plot was taken at the same coordinates as the ICV vector plot. Despite best effort to make the scales as close as possible, it should be noted that the colours of the contour plots are different and should not be compared directly. Shown in Fig. 47 is the simulation vector plot for the model without a deflector.

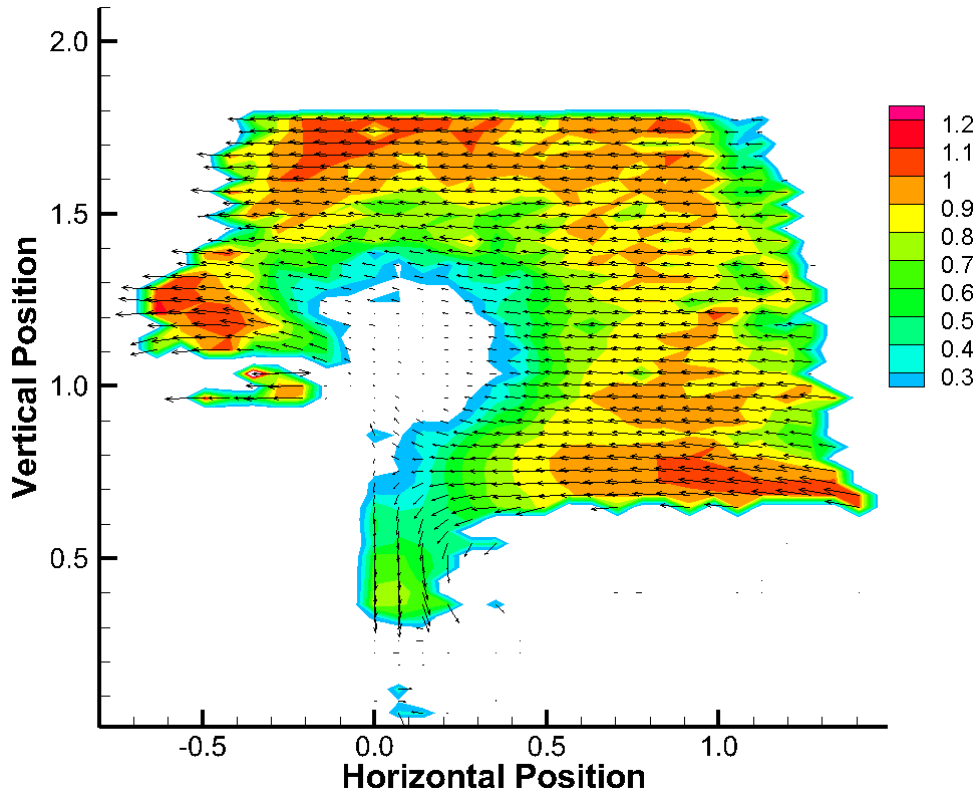


Figure 46: ICV Model without deflector (velocity nondimensionalized with  $U_{\infty} = 2.34$  m/s).

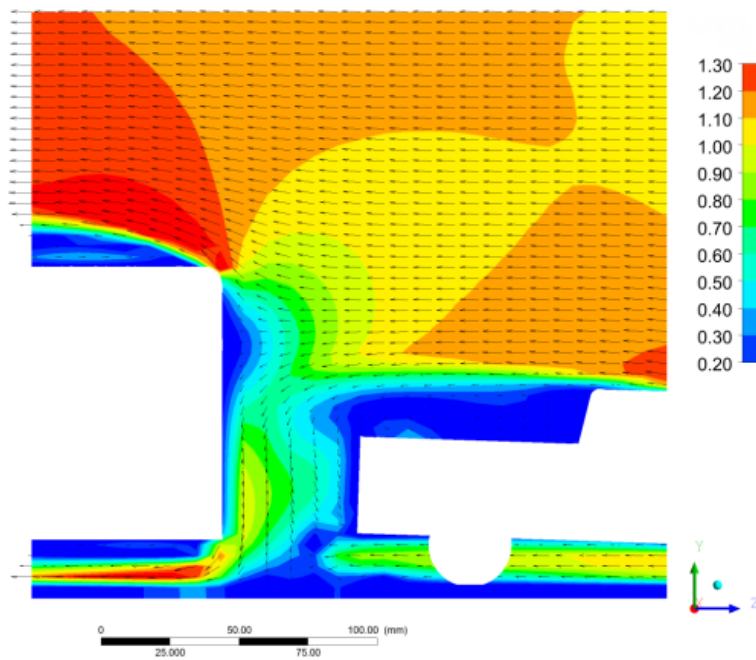


Figure 47: Simulation velocity contour and vector plot (velocity nondimensionalized with  $U_{\infty} = 2.34$  m/s).

Since the simulation is not limited in the same way that ICV is, it is able to resolve the flow around the front leading edge of the trailer. Figure 47 must be relied upon to help understand what is happening in the flow.

It can be seen by comparing Fig. 46 and 47 that the flow accelerates over the top of the truck which is expected. The flow then separates from the roof of the truck where it passes over the box of the truck before flowing down the back of the truck. As seen in the streamlines presented earlier in Fig. 37 the flow which separates from the roof of the truck is not the flow which stagnates on the front of the trailer. The flow above the roof of the truck is seen to be in the range of 1.2 – 1.3 which is slightly above that of the ICV vector plot which had a range of 1.1 – 1.2. However, as discussed previously, the ICV method was found to under-evaluated the velocity by up to 15% when based on the 120 Hz pattern in the streakline. Therefore, the flow between simulation and experiment in this region were found to agree with each other. Other areas that can be compared are the areas away from the top leading edge of the trailer; these include some of the area between the truck and the trailer and near the top of the velocity vector plot.

By comparing Figs. 46 and 47 and looking at the area between the truck and trailer, it can be seen that the flow is directed downwards and at the same magnitude in both images. As for the area towards the top of the vector plot, much like the flow above the truck the ICV method under-predicts the velocity, however the vectors all appear to have the same direction, as discussed later in Section 5.4.4.

### ***5.4.3 Model with Deflector***

The next experiment and simulation studied the model with the deflector. Velocity contour and vector plots were produced for each. For this test the ICV was not as limited in its evaluation of the flow around the top leading edge of the trailer, as it was in the previous test. With the flow now deflected up and over the trailer the loss of discrete smoke streaklines was no longer experienced. Therefore, the gap in data seen before was significantly reduced, and a more complete velocity contour and vector plot was produced. Figure 48 shows the ICV output and Fig. 49 shows the vector plot from the simulation for the model with a deflector.

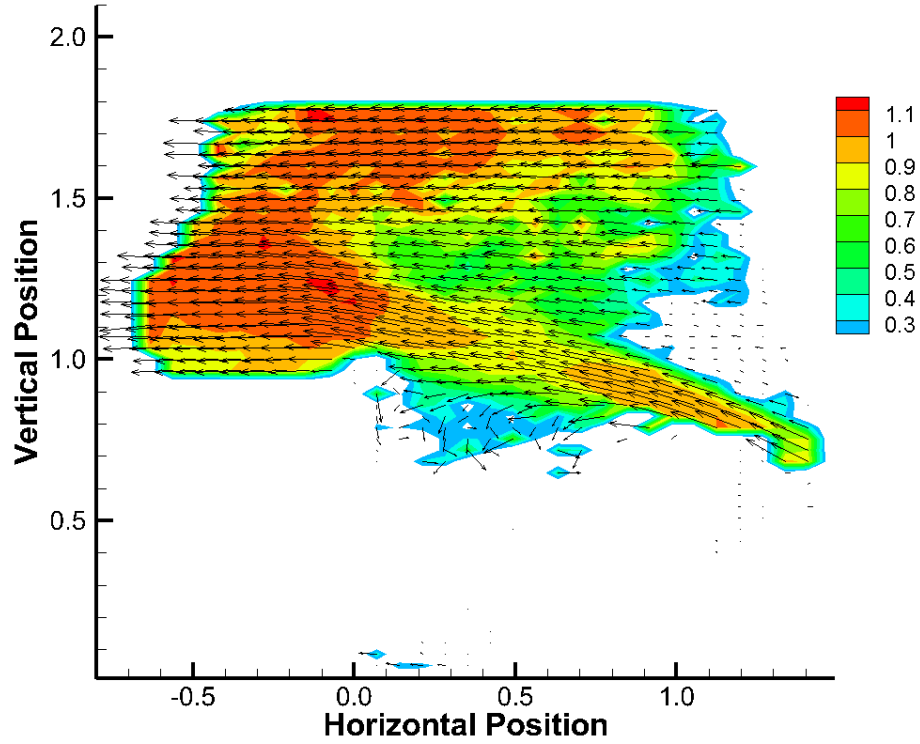


Figure 48: ICV Model with deflector (velocity nondimensionalized with  $U_{\infty}= 2.34$  m/s).

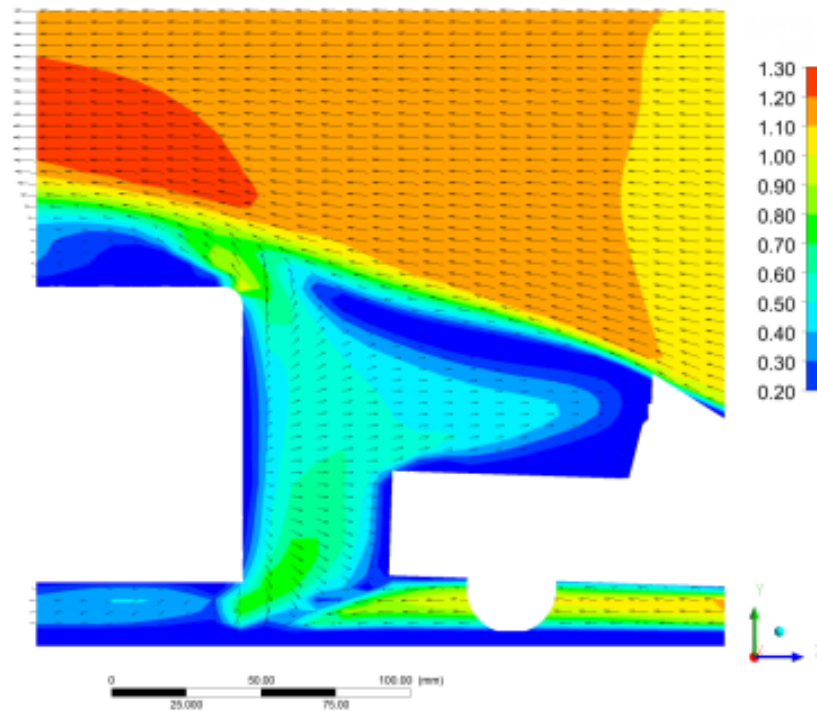


Figure 49: Simulation velocity contour and vector plot (velocity nondimensionalized with  $U_{\infty}=2.34$  m/s).

From Figs. 48 and 49 it can be seen that there is some general agreement between the two methods; however, there appears to be a large disparity between the two methods in the flow at the front of the trailer. In the simulation it can be seen that the vectors are directed more upwards as a result of an up flow of air from in front of the trailer, this is what caused the “kick up” observed previously in the streamlines. This flow pattern was not experienced in the experiment. The cause of this odd behavior in the simulation is discussed further in Section 5.6.

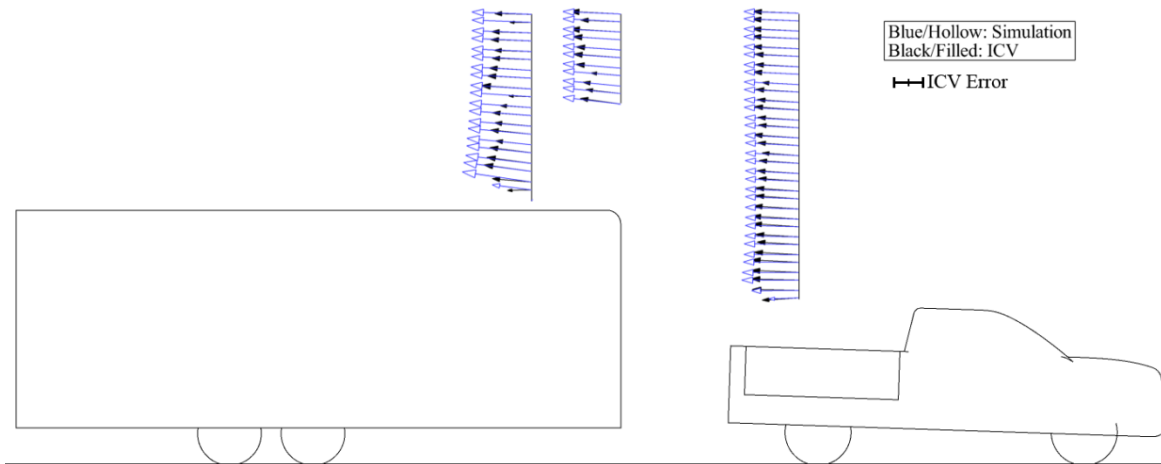
One feature to note about the ICV vector plot is that there appears to be a triangular shaped region in the plot with the left hand corner located at approximately (0.0, 1.4) and with the region extending to the right from there. This region in the ICV shows that the velocity is 0.8 or less, which is highly unlikely as this is part of the free-stream which has a value of 1.0. Therefore, this region is believed to be an incorrect measurement of the flow, and not just the usual under-evaluation found in the free-stream flow discussed earlier. Like the simulation though, over the trailer there is an acceleration of the flow. While the flow has been deflected to above the trailer, the area through which the air can pass is being choked down. This is what causes the speed-up of air in both cases.

From these 2D vector plots the basic properties of the flow could be found and studied. These plots suggest that the stagnation point on the front face of the trailer has been moved upward. This would result in a significant change in the pressure drag of the model and was proven to be true by examining the pressure contour on the surface of the model. While a slight increase in the pressure drag of the truck was seen, the trailer’s reduced drag was enough to offset the increase and a net reduction in drag was found. Studying the flow at the 2D level was found to be beneficial, and using the mid-plane was a great first step in understanding the aspects of the flow. However, to gain a deeper understanding of the flow the 3D aspects of the flow must be considered.

#### ***5.4.4 Flow Profile Comparisons***

To more appropriately compare the flow calculated in the simulation and the flow evaluated using ICV in the experiment, vectors from each test were compared directly with one another. This allowed for a comparison of both the direction and magnitude of the vectors. Three different locations were chosen, the first location was half-way between the truck and trailer ( $x/h = 0.70$ ),

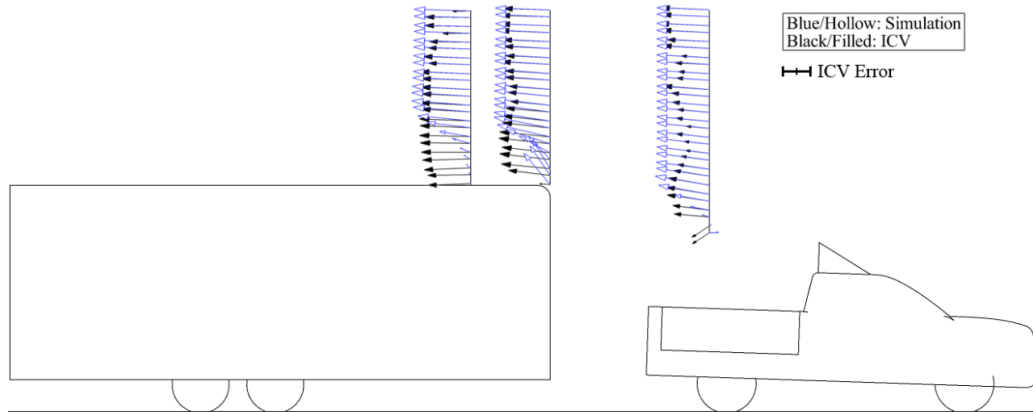
the second location was above the trailer at the front face of the trailer ( $x/h = 0$ ), and the final location was on top of the trailer after the leading edge ( $x/h = -0.35$ ).



**Figure 50: Vector plot comparisons between simulation and ICV. Blue/Hollowed vectors are from the simulation. Black/Filled vectors are from ICV. The error bar shown in the image is the uncertainty in the ICV method. The nondimensionalized error is plus/minus 0.3 from the middle of the error bar.**

Figure 50 shows the no-deflector case. The blue/hollow arrows represent the flow calculated in the simulation, while the black/filled arrows represent the flow measured by the ICV method. As seen before the ICV method under-evaluated the velocity's magnitude; however, the direction of the vectors matched almost identically with only minor deviation in some of the vectors. This shows that while the ICV method was not accurate in measuring the magnitude of the velocity; it correctly evaluated the flow direction.

A vector plot comparison was also done for the deflector case shown in Fig. 51.



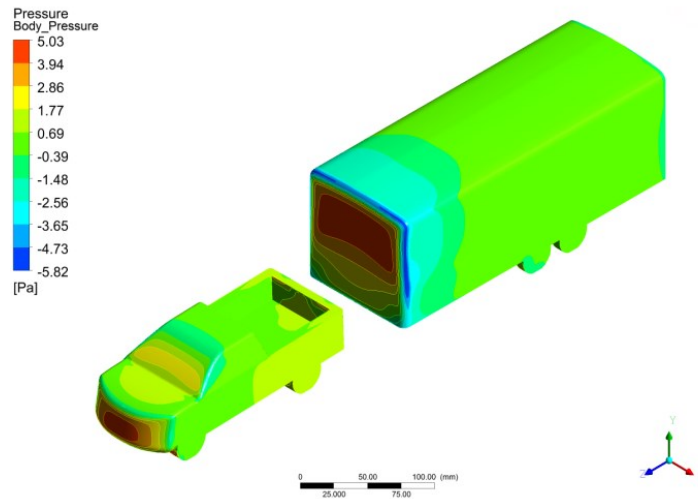
**Figure 51: Vector comparison between simulation and experiment with deflector. Blue/Hollowed vectors are from the simulation. Black/Filled vectors are from ICV. The error bar shown in the image is the uncertainty in the ICV method. The nondimensionalized error is plus/minus 0.3 from the middle of the error bar.**

Figure 51 shows that the two different methods do not agree with each other as well as before in the no-deflector case Fig. 50. This is because the simulation settled on a solution that was topologically completely different. Discussed later in Section 5.6, a pair of vertical vortices was found to wrap around the front of the trailer. This caused a large vertical component in the velocity close to the front leading edge of the trailer in the simulation's vectors, as the vortex pair's induced velocity field deflected the flow away from the trailer. The vectors that compare well in this case are the vectors closer to the free-stream. Like before, the ICV method underestimated the magnitude of the velocity; however, it captured the direction quite well. The bottom two vectors on the midway profile line between the truck and trailer were evaluated below the shear-layer in the experiment. At this part of the flow the vectors become slightly erratic and should be ignored.

Apart from the discrepancies discussed in the vector plot comparison in the deflector case, the ICV method was found to agree well with the simulation, and the simulation results were mostly within error of the ICV method. ICV captured the correct flow direction, and at times the proper magnitude. The lack of accuracy in the velocity magnitude however is not a systematic error since the discrepancy is not uniform between the simulation and ICV vectors.

## 5.5 Pressure Contours

The pressure contours on the surface of the model were studied with and without the deflector present. It was determined from the CFD analysis that the pressure drag made up about 90% of the aerodynamic drag on the LVTS while the other 10% was due to skin friction. Since the pressure drag of the model contributed the most, looking at the pressure contours was an effective way to visually show how the drag was reduced with the addition of the deflector. The pressure contours can be seen below in Figs. 52 and 53.



**Figure 52: Pressure contour model no deflector according to CFD.**

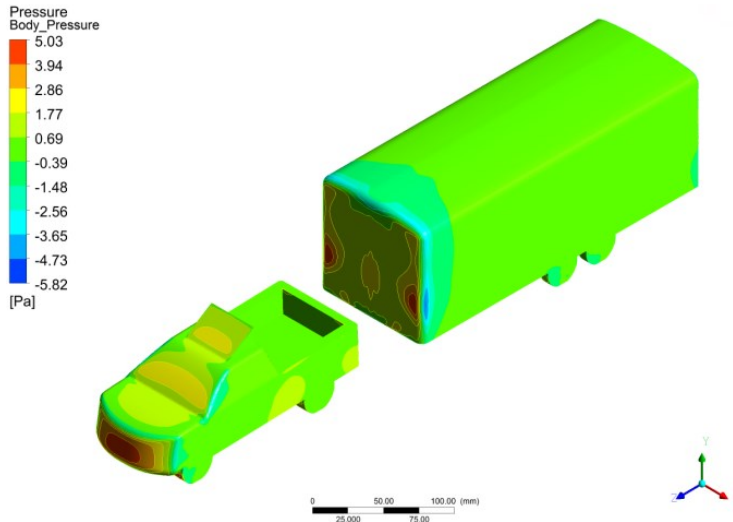


**Figure 53: Pressure contour model with deflector.**

Figures 52 and 53 immediately show that the large high pressure zone on the front of the trailer has been almost completely removed through the addition of the deflector. While the deflector itself has added frontal surface area and drag to the model, the reduction of the pressure on the front of the trailer has led to a net positive benefit by reducing the models' overall drag. The pressure values shown in Figs. 52 and 53 are actually the gauge pressure, and the negative values show where the pressure is less than the atmospheric pressure.

## 5.6 Vortex Pair at Front of Trailer

When the deflector was added to the model in the simulation, a peculiar flow characteristic was found that was unique to the simulation and was not present in the wind-tunnel experiment. A pair of vortices were found to wrap vertically around the front face of the trailer. At first it was thought to be an anomaly with the simulation since this flow topology was not present in the experiment, and it very well may be one that will never occur in reality. Nevertheless it was not immediately discarded since it is hypothesized that this new topology may be a result of critical flow parameters that could be present in the simulation and not in the experiment. It is known that the interaction of a body's wake with the stagnation point of a downstream object can produce a vortex pair. This was the same concept that led to the idea in Chapter 2 that the hood separation was actually a pair of vortices holding the smoke off the hood of the truck, with the vortices created by the wake of the smokewire interacting with the stagnation point on the front of the truck. Figure 54 below uses streamlines to visualize the vortex wrapping around the front of the trailer in the simulation with the deflector.

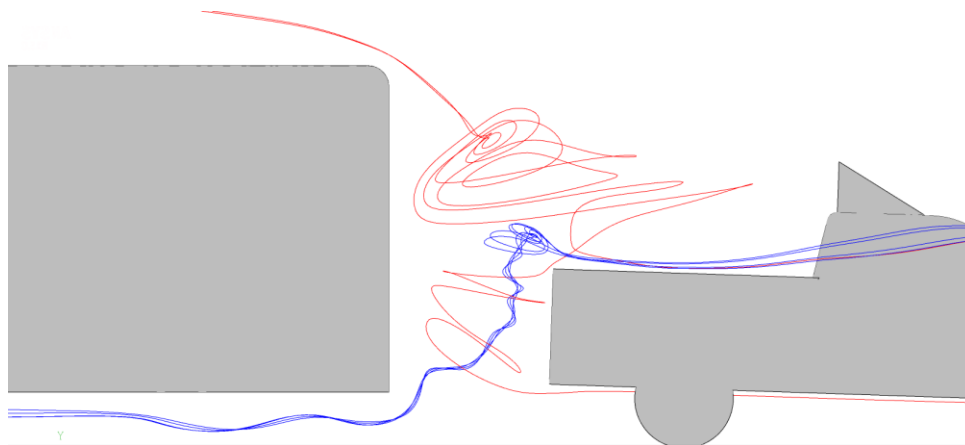


**Figure 54: Vortex wrapping around the front of the trailer.**

In Fig. 54 the streamlines show the presence of a vortex wrapping around the front of the trailer. The streamlines going over the trailer are located in the center of the vortex. The streamlines flowing under the trailer are wrapping around the core of the vortex. Shown in Fig. 54 is only one of the vortices, there is an equal and opposite vortex mirrored across the mid-plane of the VTS. Note that the streamlines entering the vortices come from the side of the truck. That indicates that the vorticity entering the vortices has come from the sides of the truck, which represents the drag coming from the flow interaction with the truck.

## **5.7 Moving Ground-Plane**

In an effort to more closely model the full-scale moving vehicle-trailer system situation the ground-plane in the simulation was made to move. This would more accurately simulate a vehicle travelling down a road. However, the wheels of the truck and trailer were still stationary as opposed to rotating, and the fluid domain was kept the same size as the wind-tunnel. Making the ground-plane move was a simple addition to the simulation without being a large incremental computing resource drain. The overall flow around the model appeared to be, for the most part, quite unaffected by the addition of the moving ground-plane. In addition to studying the effect on the flow due to the ground-plane, the deflector was tested to compare its drag reducing effectiveness between cases with and without the ground-plane moving. For both tests the inlet velocity and the ground-plane were set to have a velocity of 2 m/s in the same direction.

### ***5.7.1 Effect on Flow Around Model***

It was found that the moving ground-plane did not significantly affect the flow around the model, however it was found that there was a slight reduction in the coefficient of drag of the model due to its presence. When the ground-plane was stationary the flow profile under the vehicle was very similar to Poiseuille flow between two flat plates. When the ground-plane was made to move the flow under the vehicle was very similar to Couette flow with a pressure gradient on top of it. In Poiseuille flow there was more back pressure on the fluid which caused a slowdown of air entering the underside of the vehicle; this will be referred to as “choking” of the flow. However, in Couette flow, since one side of the domain is moving, while the other boundary is stationary, there is much less choking of the flow and this resulted in more air flowing

underneath the vehicle. The flow profile was found from the simulation results and can be seen in Fig. 55 below.

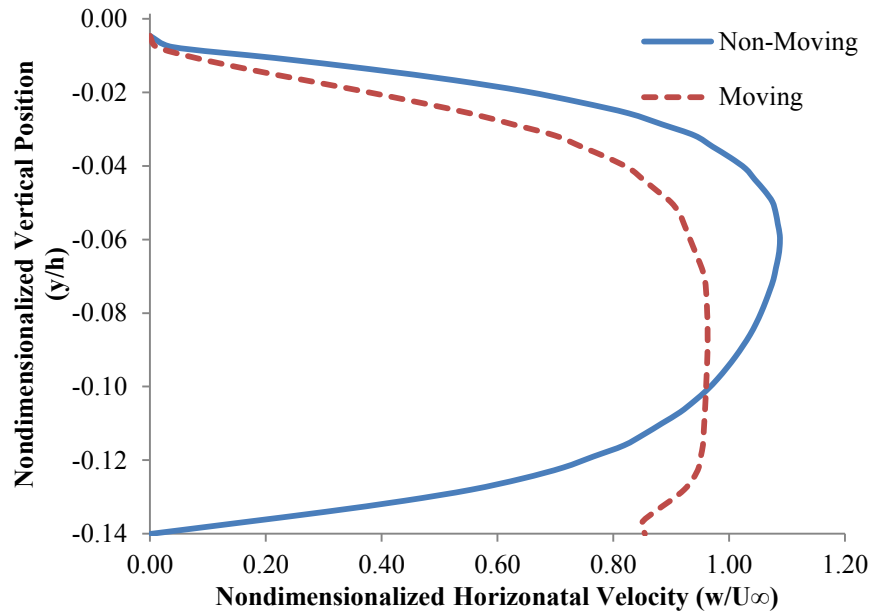


**Figure 55: Flow profile underneath vehicle with non-moving and moving ground-plane. (Position nondimensionalized by  $h = 115$  mm, Velocity nondimensionalized by  $U_{\infty}=2.34$  m/s)**

Figure 55 shows the profiles for both the moving and non-moving ground-planes, and how they reasonably resemble the Pousielle and Couette flow profiles. The y-origin is located at the bottom of the trailer. From this it can be said that there is a higher average flow rate of air passing under the vehicle in the moving ground-plane case. In addition to this, Fig. 55 also shows that the gradient of the velocity associated with the non-moving ground-plane is much larger than the gradient of the moving ground-plane profile line. This means that there will be a lower wall shear stress on the model when the ground-plane is made to move. This helps explain why the drag on the vehicle is reduced when the ground-plane is made to move.

In addition to the flow profile under the model being affected by the moving ground-plane, other flow characteristics were also affected, such as the pressure on the LVTs surfaces. By comparing the pressure contour for both the no-deflector, and with-deflector cases before and after the

ground-plane was made to move, it can be seen that the pressure on the front faces of the truck and trailer were reduced. This is shown in Figs. 56, 57, 58, and 59 below.

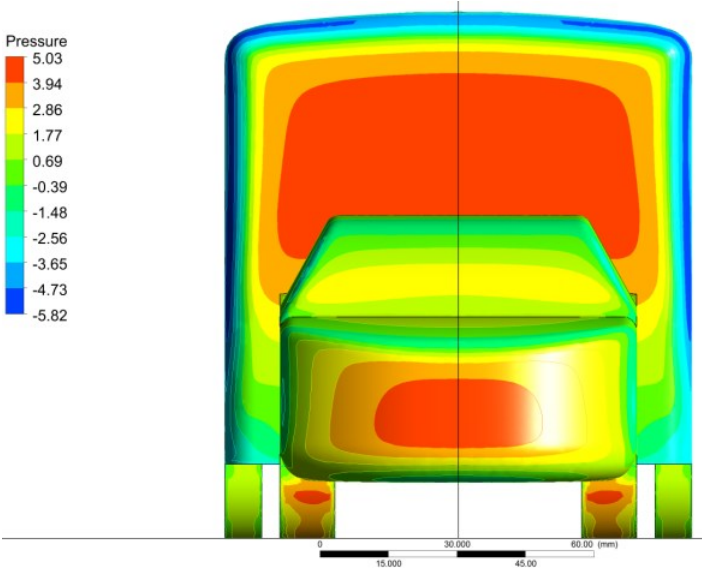


**Figure 56: Simulation of LVTS with non-moving ground-plane.**

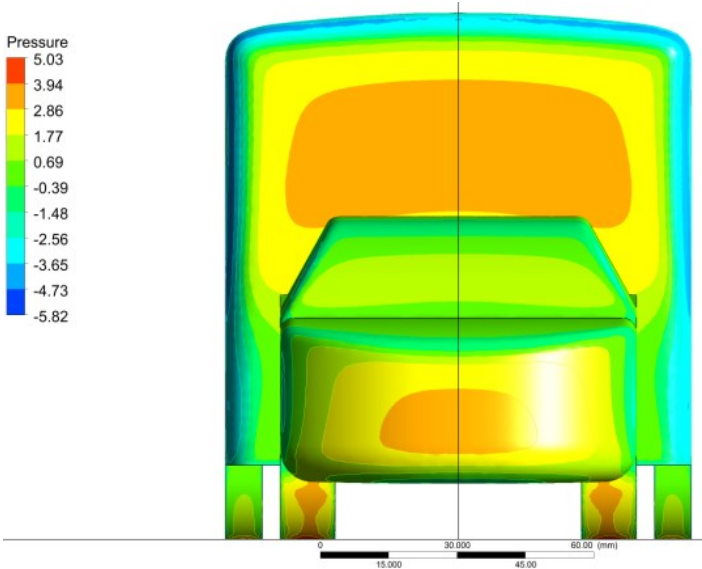


**Figure 57: Simulation of LVTS with moving ground-plane.**

The non-moving ground-plane case exhibits a large range of pressures, both high and low, compared to the moving ground-plane case. This explains why there is a reduction in drag when the ground-plane is made to move, and is further discussed later. Similar results are seen in the

case where the deflector is present. Figs. 58 and 59 below are with the deflector when the ground-plane is stationary and moving, respectively.

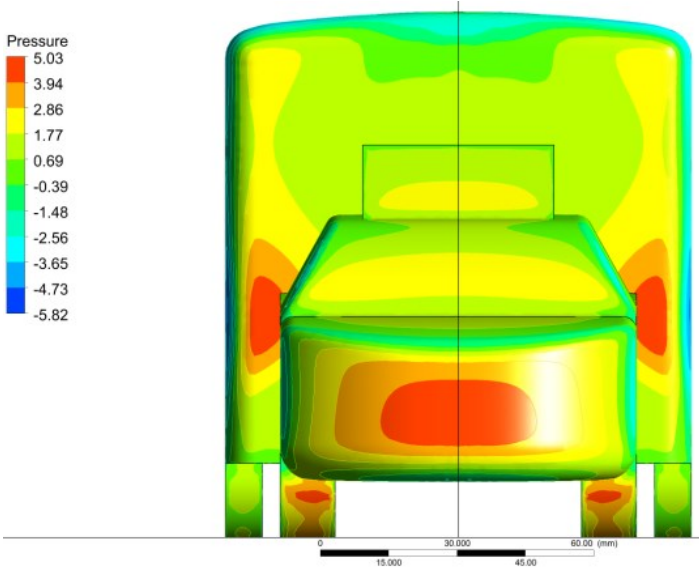


**Figure 58: Simulation with deflector, stationary ground-plane.**

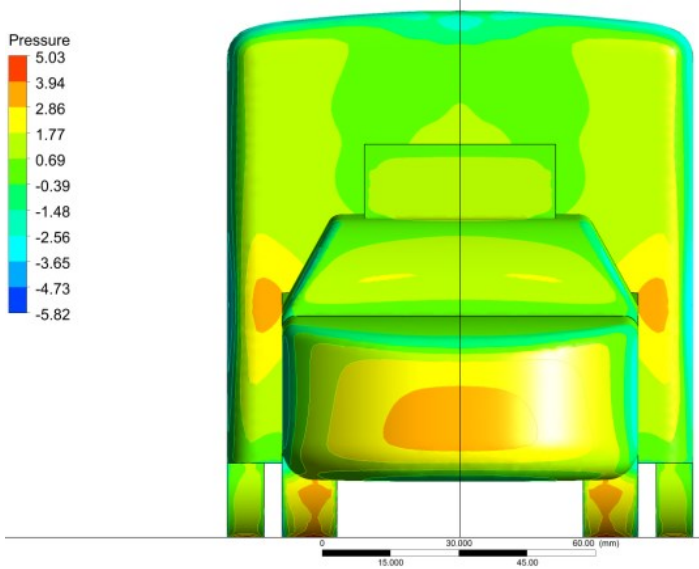


**Figure 59: Simulation with deflector, moving ground-plane.**

Another change with the moving ground-plane is the location of the stagnation point on the front of the truck. It was found that this stagnation point was lowered when the ground-plane was

moving. This is difficult to tell by using pressure contours, therefore, streamlines were used to compare two cases in Figs. 60 and 61.

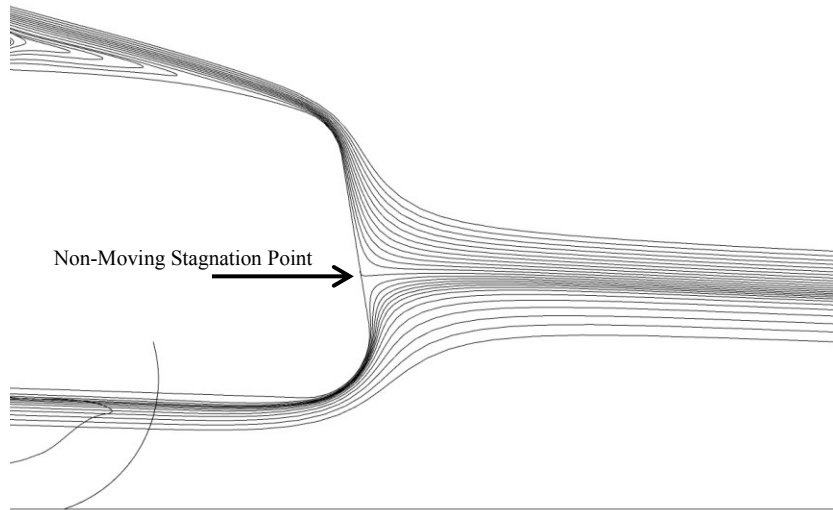


**Figure 60: Truck stagnation, non-moving ground-plane, no deflector.**

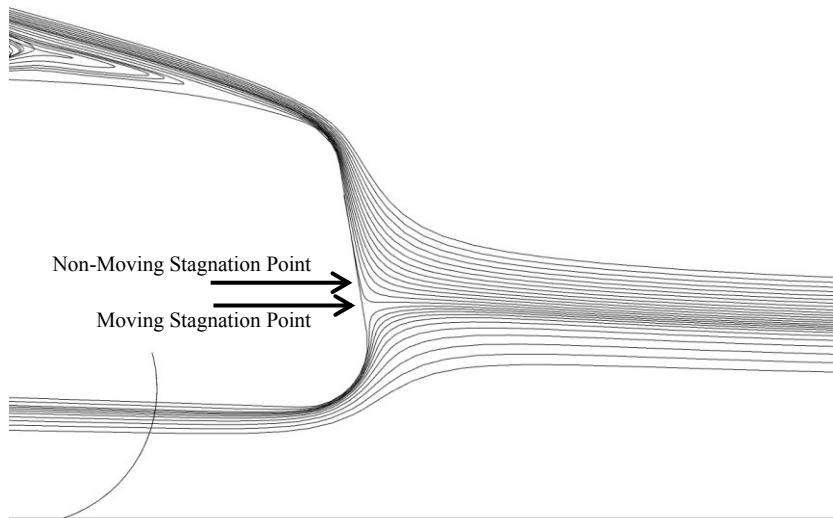


**Figure 61: Truck stagnation, moving ground-plane, no deflector.**

Figures 60 and 61 show that the stagnation point was lowered when the ground-plane was moving. An argument for why this is possible is as follows. Consider that there is less of a restriction of the flow under the model, because of the reduction of shear stress at the ground-plane when it is moving, as indicated in Fig. 55. This would suggest that the volume flow rate

beneath the vehicle, and therefore the stagnation streamline, would increase. However, this would lead the observer to expect that the stagnation streamline should move upward to accommodate the increased flow rate. Paradoxically, the stagnation streamline was observed to move downward. This is not inconsistent with an increased flow rate in this case, because the upstream flow beneath the stagnation streamline is now a fuller, completely uniform flow profile, as opposed to the volume flow rate deficit that goes with the boundary layer flow, when the ground-plane is stationary. The conclusion is that a lowered stagnation point is not inconsistent with an increase in flow rate beneath the vehicle, when the ground-plane is moving relative to the vehicle.

### ***5.7.2 Effectiveness of Deflector with Moving Ground-Plane***

Since it was found that the moving ground-plane had an effect on the drag of the model, it was necessary to check and see if the effectiveness of the deflector was affected by the moving ground-plane. The drag was calculated four different ways: when there was no deflector with the ground-plane moving and not moving, and when the deflector was present with the ground-plane moving and not moving. The results are summed up in Table 8, and are all for the fluid properties listed in Table 4.

**Table 8: Effect of Deflector on Coefficient of Drag with Moving Ground-Plane.**

	Ground-Plane		Change
	Non-Moving	Moving	
Without Deflector	1.06	0.93	-12%
With Deflector	0.88	0.81	-8%
Change	-17%	-13%	

From Table 8 it can be seen that there was a reduction in the drag of the model when the deflector was present in both cases. However, the effectiveness of the deflector was reduced when the ground-plane was made to move. A 13% reduction in the drag was found when the

ground-plane was moving, instead of the original 17% reduction when the ground-plane was stationary.

The reason for this reduction in effectiveness is that the moving ground-plane had a larger effect on the model when no deflector was present. A reduction of 12% in drag was found with the model when no deflector was present, but only an 8% reduction was found with the model when the deflector was present. The data show that the model with no deflector is more susceptible to the influences of the ground-plane. This is because of the size of the stagnation zones on the model when no deflector is present. Any flow change that affects the stagnation zones will have a large impact on the drag of the model, and since the model with the deflector has removed the stagnation point from the front of the trailer, the effect of the moving ground-plane on the model with deflector has been reduced. It was found that when the ground-plane was made to move, and there was less choked flow under the vehicle, the pressure on the front faces of the model was reduced both with and without the deflector present, but more for the no-deflector case.

As discussed in Chapter 1, a previous study found that a flat plate deflector on a car towing a small camping trailer (caravan) could reduce the drag by approximately 15% (Hucho 1998). Even though it is a different geometry, this boosts confidence in the current CFD since it compares well with the current result of a 17% decrease without a moving ground-plane. There was not a moving ground-plane in the previous study. Additionally, in Chapter 1 and before CFD was performed, estimates of the  $C_d$  before and after drag reduction was made. The estimated  $C_d$  before drag reduction was 0.82, and after was 0.75. From the current results the  $C_d$  was 0.93 before drag reduction and 0.81 after with the moving ground-plane. The estimates were low; however, the blockage of the simulation has not been accounted for. It was previously shown that when the blockage was reduced from 11% to 4.2% the  $C_d$  of the model with no deflector was reduced from 1.06 to 0.84. This means that the simulated  $C_d$  values without blockage could more closely match the estimated values, than the current CFD result based on the blockage in the wind-tunnel experiments.

### ***5.7.3 Greenhouse Gas Emissions and Fuel Consumption Reduction***

One positive effect of reducing the aerodynamic drag of a motor vehicle is that the fuel consumption is reduced, and less greenhouse gases are emitted. A study on HVTs (Patten 2012)

found that approximately 67% of the power required to cruise at a speed of 105 km/h is used to overcome aerodynamic drag, while the remaining 33% of the power is spent overcoming mechanical losses and rolling resistance. This percentage is for HVTS; however, it will serve as a preliminary estimate on how much of an impact the reduction in aerodynamic drag can have on the LVTS. The aerodynamics of typical LVTS is much less refined than the modern HVTS, therefore it is expected to be an underestimate. The 13% reduction in aerodynamic drag that was found for the LVTS would result in a 9% reduction in the vehicle power required. This suggests that fuel consumption and, assuming a simple linear correlation, greenhouse gas emissions will be reduced by 9%.

## 6. Conclusions

### 6.1 Summary

The goals of this study were to determine the impact a simple non-optimized deflector could have on the drag of a Light Vehicle-Trailer System, and to learn the characteristic flow patterns over a modern LVTS. Low Re wind-tunnel experimental models were used for simplicity, and gave a good qualitative estimate of how the flow might be affected. From these experiments an understanding of the characteristic flow patterns was found. Patterns included the identification of several separation zones, and stagnation points.

Computational Fluid Dynamic simulations were run in parallel with experiments to obtain quantitative results of the drag. In the simulation which most closely matched the full-scale case, a reduction in drag of 13% was found, despite no effort being made to optimize the deflector. Since the deflector used in this study was not optimized it is thought that further drag reduction may be possible. It is conjectured that this optimization would require positioning the deflector so that the air that separates off the deflector would then reattach near the front leading edge of the trailer. There was good comparison between the simulations and experiments, with the notable exception of the deflector case, where there were significant differences in the topology of the flow.

This chapter will review details of the overall findings.

### 6.2 CFD Drag Force Reduction

Two CFD tests were performed to determine the drag reduction potential of a simple wedge deflector. The first test studied the switching of the ground-plane from a stationary boundary condition to a moving boundary condition with velocity set to match the free-stream velocity. With the moving ground-plane the  $C_d$  of the model without the deflector was 0.93, and with the deflector was 0.81, which gave a 13% reduction in drag. When the ground-plane was stationary the  $C_d$  of the model without the deflector was 1.06, and with the deflector was 0.88, giving a drag reduction of 17%.

In the second test the effect the blockage ratio had on the  $C_d$  was analyzed. The blockage was systematically reduced from 11% to 4.2% which caused the  $C_d$  to be reduced from 1.06 to 0.84. This test was only performed for the no-deflector case.

### ***6.2.1 Comparison of Preliminary Investigations with Final CFD Results***

From a previous experimental work a reduction of 15% was achieved for a simple flat plate deflector on a car towing a small camping trailer (caravan). The value of drag reduction achieved here via CFD was 17% for the relevant comparison when there was no moving ground-plane. Although being for a different geometry, this suggests that the current deflector was similarly effective for a modern LVTS, and reinforces confidence in the present CFD.

Before CFD was performed, estimates of the  $C_d$  for a modern LVTS before and after drag reduction were made here, assuming the 15% drag reduction was achievable. The estimated  $C_d$  without drag reduction was 0.82, and with was 0.75. Once CFD was performed it was found that with a moving ground-plane the  $C_d$  before and after drag reduction was 0.93 and 0.81 respectively. The original estimates before CFD was performed were lower, and did not take blockage into account. This suggests that simulated  $C_d$  values without blockage, if performed, might more closely match the estimated values than the current CFD result based on the 11% blockage in the wind-tunnel experiments.

### ***6.2.2 Relevance to Full-Scale Road Applications***

While the study presented here focused mainly on the wind-tunnel experiments and computer simulations of a model, the intention was to study the potential effect a simple deflector had on the full-scale LVTS. The experiments and simulations were run with a Re of 15,800, however, the full-scale has a Re of approximately 5,300,000. This difference in Re is not expected to significantly affect the scaling of the model to the full-scale as the majority of the flow is turbulent separated flow with a fixed separation point, which is associated with the  $C_d$  being approximately Re independent. Other uncertainties that are present in the simulation are the mesh, the blockage, the discretization schemes, as well as the inaccuracies due to modelling the turbulence when using Reynolds-Averaged Navier-Stokes equations. Additionally, it is not clear if the 13% drag reduction found in the simulation is correct given that a different topology of the

flow was found compared to the wind-tunnel experiment. Many full-scale properties of the actual flow were not modelled in this study. These include the atmospheric turbulence, the natural wind boundary layer, if the LVTS was driving into a cross-wind creating yaw, road vibrations, and rotating wheels.

### **6.3 Greenhouse Gas Emission and Fuel Savings**

One goal of this study was to estimate the effect a drag reducing deflector could have on the emissions of greenhouse gases and fuel consumption. Published results for Heavy Vehicle-Trailer Systems (HVTS) showed that approximately 67% of the power required to cruise at highway speeds was to overcome aerodynamic drag. The aerodynamics of typical Light Vehicle-Trailer Systems (LVTS) are much less refined than modern HVTS, therefore it is expected to be an underestimate. The 13% reduction in drag that was found for the LVTS would result in a 9% reduction in fuel consumption and, assuming a simple linear correlation, a 9% reduction in greenhouse gas emissions.

### **6.4 Experiment-Simulation Comparison Conclusions**

#### ***6.4.1 Reynolds Number Effect***

##### **6.4.1.1 Experimental Reynolds Number Effect**

In preliminary experiments, an unexpected flow separation on the hood of the truck was found. Unsuccessful attempts were made to reduce the separation bubble by tripping the boundary layer from laminar to turbulent. The  $Re$  was increased by a factor of 2.8 from 15,800 to 44,400, which was achieved by increasing the speed of the wind-tunnel. At the higher  $Re$  the hood separation was found to be significantly reduced in size. Apart from this, the increased  $Re$  did not appear to affect the other characteristics of the flow, such as the trailer's stagnation point and the trailer's separation zones. This was the case since, once separated and fully turbulent,  $Re$  does not have a significant impact on the flow.

##### **6.4.1.2 Effect of Reynolds Number on the Coefficient of Drag**

The CFD Reynolds Number was changed from 14,900 to 15,800. A small change in the  $C_d$  was recorded for both the no-deflector and deflector case. In the no-deflector case the  $C_d$  was found

to decrease from 1.06 to 1.04, a 4% reduction and in the deflector case the  $C_d$  was decreased from 0.88 to 0.84, a 5% reduction. Therefore the simulation was not quite Re independent. It is expected that the  $C_d$  will become Re independent once the Re is increased sufficiently.

#### ***6.4.2 CFD Moving Ground-Plane***

To more closely simulate the full-scale case a test was performed with a moving ground-plane. However, the wheels of the LVTS were still stationary. Due to the limitation of a fixed wall in the wind-tunnel, the moving ground-plane was only tested in the simulations. With the moving ground-plane having the same speed as the free-stream flow, it was found that the deflector still reduced the drag, but with a lower effectiveness. The effectiveness of the deflector was reduced from 17% to 13%. The reason for this is that, since there was less-choked flow under the model, less air had to flow over top of the model, which reduced the pressure on the front faces of the LVTS. This in turn reduced the effectiveness of the deflector.

The major flow characteristics were not significantly affected by the moving ground-plane. The largest change was that the flow profile underneath the LVTS had been altered. It was found that in the non-moving case, the flow profile resembled a Poiseuille type flow. However, since the flow was turbulent the profile was more of a tophat. In the moving ground-plane case it was found that the profile had a Couette type flow profile with a super-imposed pressure gradient. Both observations are consistent with what would be expected given the respective boundary conditions. This is why there could be a higher flow rate of air underneath the LVTS with a moving ground-plane.

It was observed that with a moving ground-plane the stagnation point on the front of the LVTS was *lowered*. This was the result of the upstream flow beneath the stagnation streamline having a uniform flow profile, as opposed to the volume flow rate deficit that is found with the necessary boundary layer when the ground-plane is stationary. It was concluded that the lowered stagnation point was not inconsistent with an increase in flow rate beneath the vehicle.

### **6.4.3 Streaklines and Streamlines**

#### **6.4.3.1 No Deflector**

Early in this study it was thought that the flow *separating off the truck roof* was stagnating on the trailer's front face. This was found to be an incorrect understanding once the simulation's results were analyzed. The streaklines were found to have a good qualitative basis for understanding the overall characteristics of the flow, and gave good insight into how the flow should be altered to reduce the drag of the LVTS. From the simulation results, streamlines were produced that showed that a primary flow channel was present from above the truck and then downward between the truck and trailer. With this discovery it was determined that it was the free-stream flow that was stagnating on the trailer's front face, and not the flow separating off the truck. From the simulation streamlines it appeared that the flow separating off the truck's roof could be reattaching to the back of the truck. Other primary features in the no-deflector case included the stagnation zone on the trailer's front face; separation zones surrounding the trailer's front leading edge, on the top, bottom, and sides of the trailer; and a separation bubble on the front hood of the truck.

#### **6.4.3.2 With Deflector**

With the deflector it was immediately apparent that the stagnating flow on the front of the trailer had been significantly affected. From the experimental smoke streaklines the free-stream flow over the truck was no longer stagnating on the front of the trailer but being deflected over the trailer. In the simulation the streamlines showed that the stagnation had been removed from the front face of the trailer; however, it was found that the simulation had calculated a completely different topological solution. In this low  $Re$  simulation a vertically-oriented vortex pair was found to be present at the front of the trailer, wrapping around the top and bottom of the trailer. These vortices were not present in the experiment; however, it was theorized that there might be critical parameters which could trigger the onset of this vortex pair. Therefore, it is possible that they may be found in future experiments with slightly different settings. It is suggested that the vortex pair was created by the truck's wake interacting with the stagnation zone on the front of the trailer.

### **6.4.3.3 Augmented Reality – Super-imposed Streaklines with Streamlines**

A hybrid image of super-imposed streamlines and streaklines showed that they agreed very well. One exception to this was the difference in the flow around the trailer in the deflector case, where a different topological solution was found.

### **6.4.4 Velocity Vector Plots**

Velocity vector and contour plots were produced from the experiment and simulation in order to compare to the flows. Issues were present with the ICV method which resulted in small regions where no data could be collected. This was most noticeable in the deflector case at the top leading edge of the trailer. The ICV method broke down in the region because of the highly accelerated flow. Once away from this region the ICV worked quite well. Overall the velocity vector plots were found to compare well between the experiment and simulation, with the exception of the deflector case around the front of the trailer due to the presence of the nonphysical vortex pair in the simulation.

#### **6.4.4.1 Velocity Vector Profile Overlays**

As with the streakline-streamline overlay the vectors from both the experiment and simulation were overlaid to have a better comparison. This was done by considering several vertical interrogation lines for the data in the experiment and simulation data. This comparison showed that while the ICV captured the direction of the velocity vector very well, it consistently under-evaluated the velocity's magnitude. The under-evaluation of the velocity magnitude was not systematic as difference in speed from the simulation to the experiment was different for every vector.

## **6.5 Strictly Experimental Conclusions**

### **6.5.1 Preliminary Experiments**

In preliminary flow visualization experiments, two characteristic flow patterns were identified. The first was the stagnation of the flow on the leading face of the trailer followed by a separation as it would flow upward and over the top leading edge of the trailer. The second pattern was presence of an unexpected separation bubble over the hood of the truck. It was confirmed that it

was an actual separation and not an artifact of the flow visualization process. Its presence had a minor effect on the downstream flow over the trailer.

When a deflector was added to the roof of the truck it was found that the stagnation point was removed from the front face of the trailer. It was expected that this would result in a reduction of the aerodynamic drag of the LVTS.

Buoyancy and blockage were both studied on a preliminary basis. It was concluded that the effect of blockage, at least on the qualitative aspects of the flow, was minor.

### ***6.5.2 Turbulent Bottom Boundary Layer***

The boundary layer on the bottom surface of the wind-tunnel was studied with no model present to see if the flow remained laminar, or transitioned to turbulence. From the photographs it was determined that the flow was near a critical  $Re$  since the boundary appeared to switch between laminar and turbulent at the same location. In an effort to promote a laminar boundary layer the drop collector at the bottom of the smokewire was removed. This helped keep a laminar boundary layer, however, the boundary layer was still found to transition to turbulent occasionally.

### ***6.5.3 ICV Mean Stream Flow (No Model)***

To test the ICV method the model was removed from the wind-tunnel and ICV was performed on the uniform flow field. It was found that ICV was accurate to  $\pm 15\%$  in determining the velocity's magnitude. The output from ICV showed that it measured a non-uniform velocity vector field, in which higher velocities were found toward the bottom of the wind-tunnel. It also showed that the flow was accelerating by 12% over the region being investigated. Estimates showed that the flow should only have accelerated by 2% due to the increased thickness of the boundary layer. The speed measured by ICV was compared to the speed measured by a Pitot-static probe at a single point upstream of the ICV investigation region, and it was found that the ICV under-evaluated the speed of the flow by up to 15%. It was determined that this error was not due to pixel error alone.

A vertical buoyancy velocity was present in this study due to the presence of the heated smokewire. The velocity deviation from zero was found to be very small; its magnitude was only about 2% of the free-stream velocity. With the magnitude so low, it was on the order of the error present in the ICV method, and was ignored throughout the study.

## **6.6 Strictly Simulation Conclusions**

### ***6.6.1 Domain Independence***

When the effect of the blockage ratio was being tested, the simulation was also checked for domain independence. It was determined that the simulation was not domain independent at a final blockage ratio of 4.2%. Richardson Extrapolation was used to predict what the final  $C_d$  would be if the effect of the domain was reduced to zero. The estimated value of  $C_d$  was found to be 0.75, compared to the value before extrapolation of 0.84 at a blockage ratio of 4.2%.

### ***6.6.2 Mesh Independence***

A mesh independence test was performed in the simulation for both the no-deflector and deflector cases. Although the no-deflector case was not mesh independent, it was determined that the simulation results were not being significantly affected by the mesh as a 23% change in mesh size resulted in <1% change in  $C_d$ . The deflector case was also not mesh independent. However, like the no-deflector case, the change in  $C_d$  was <1% for a 23% change in mesh. Richardson extrapolation was used to estimate what the  $C_d$  for the deflector case with non-moving ground-plane, as if the simulation was mesh independent, and was found to be 0.85, slightly less than the 0.88 reported otherwise. This represents an uncertainty in the calculated  $C_d$  of approximately 4%.

### ***6.6.3 Pressure Contours***

Aerodynamic drag is made up of two components, pressure drag, and skin friction. The CFD results revealed that 90% of the drag was pressure drag. The pressure on the front face of the trailer was significantly reduced with the deflector present. This was because the deflector moved the stagnation from the front face of the trailer to the top of the trailer.

## **6.7 Future Work**

In this study there was no attempt to optimize the deflector and it was capable of reducing the drag by 13%. It would be valuable to perform further simulations where the deflector is optimized to potentially reduce the drag even further. The deflector used was only a simple wedge and its shape was not altered throughout the course of this study. It would be valuable to try different shapes. One idea was to have the deflector extend down the sides of the towing vehicle. This would deflect the air around the sides of the trailer, in addition to the deflecting the air over the top of the trailer, which could potentially reduce the drag even further.

In this study the most common type of LVTS was studied; however, other types of LVTS combinations exist and the effect of the deflector needs to be tested on these. It would also be useful to perform larger wind-tunnel experiments which more closely match the  $Re$  of the model with the full-scale.

## References

- Adem, F., Zhou, D., Krishnani, P. (2010) CFD Analysis of Drag Reduction Using External Devices on Pickup Trucks. International Mechanical Engineering Congress & Exposition, Vancouver, BC, Nov. 12-18, ASME
- ANSYS, INC. (2013) ANSYS CFX-Solver Modeling Guide, Release 15.0, November
- Apps, C., (2001) A Study of "Synthetic Fence Jets" Using Image Correlation Velocimetry, University of Alberta, Mechanical Engineering, Thesis
- Beauvais F. (1967) Aerodynamic Characteristics of a Car-Trailer Combination. SAE Paper No. 670100, Society of Automotive Engineers
- Boyer H., Sigurdson L., (2015) Flow Visualization of Light Vehicle-Trailer Systems Aerodynamics. J. Vis. 18 (3) pp. 459 - 468
- Browand, F., Hammache, M. (2004) The Limits of Drag Behavior for Two Bluff Bodies in Tandem. 2004 SAE World Congress, Detroit, Michigan Mar 8-11, Society of Automotive Engineers
- Buckley, F., Marks, C. (1978) A Wind-Tunnel Study of the Effect of Gap Flow and Gap Seals on the Aerodynamic Drag of Tractor-Trailer Trucks. ASME 100, Dec, pp 434 – 438
- CBC (2015) <http://www.cbc.ca/news/politics/canada-sets-carbon-emissions-reduction-target-of-30-by-2030-1.3075759>
- Cengel, Y., Cimbala, J. (2010) Fluid Mechanics: Fundamentals and Applications, 2<sup>nd</sup> Edition, McGraw-Hill Companies, Inc.
- Chapple, D. (1998) The Role of Turbulence in Pulsation Induced Orifice Plate Flow Metering Error, University of Alberta, Mechanical Engineering, Thesis
- Environment Canada (2013) Canada's emission trends. Environment Canada, Gatineau, QC
- Ferziger, J., Peric, M. (2002) Computational methods for Fluid Dynamics, 3<sup>rd</sup> Edition, Springer

Hammache, M., Michaelian, M., and Browand, F. (2002) Aerodynamic Forces on Truck Models, Including Two Trucks in Tandem. SAE Technical Paper 2002-01-0530, doi:10.4271/2002-01-0530

Hands S., Zdravkovich M.M. (1981) Drag Reduction for a Passenger Car Towing a Caravan. Journal of Wind Engineering and Industrial Aerodynamics, 9:137 – 143

Hong, P., Marcu, B., Browand, F., Tucker, A. (1998) Drag Forces Experienced by Two, Full-Scale vehicles at Close Spacing. International Congress and Exposition, Detroit, Michigan Feb 23-26, Society of Automotive Engineers

Hucho, W. (1998) Aerodynamics of Road Vehicles. 4th edition, Society of Automotive Engineers

Koenig, K., Roshko, A. (1985) An Experimental Study of Geometrical Effects on the Drag and flow field of Two Bluff Bodies Separated by a Gap. Journal of Fluid Mechanics, 156, pp 167-204

Lakshman, M., Aung, K. (2004) Drag Reduction Through Changes in Cabin Geometry and Trailer Gap of Heavy-Duty Trucks. 2004 ASME Heat Transfer/Fluids Engineering Summer Conference, Charlotte, NC, July 11-15

Menter, F., R. (1996) A Comparison of Some Recent Eddy-Viscosity Turbulence Models. Journal of Fluids Engineering, 118, pp 514-519

Patten, J., McAuliffe, B., Mayda, W., Tanguay, B. (2012) Review of Aerodynamic Drag Reduction Devices for Heavy Trucks and Buses. National Research Council Canada

Roache, P. (1997) Quantification of Uncertainty in Computational Fluid Dynamics, Annual Review Fluid Mechanics, (29) pp 123-160

Sigurdson, L., Apps, C., Chen, T., (2003) “Two Color Image Correlation Velocimetry Applied to Turbulent Smoke-Wire Streaklines,” Experiments in Fluids 35, Sept, 2003, pp 288-290

Sitlani, M., Aung, K. (2006) Numerical Simulations on Aerodynamic Drag of Ground Transportation System (GTS) Model. ASME International Mechanical Engineering Congress and Exposition, Chicago, IL, Nov. 5-10, ASME

Taylor, G. (1938) The Spectrum of Turbulence. Proceedings of the Royal Society of London, A, 164, pp 476-490

Van Raemdonck, G., Van Tooren, M. (2008) Design of an Aerodynamic Aid for the Underbody of a Tractor-Trailer Combination. Bluff Bodies Aerodynamics & Applications VI International Colloquium, Milano, Italy, July 20-24

Watkins, S., Vio, G. (2008) The Effect of Vehicle Spacing on the Aerodynamics of a Representative Car Shape. Journal of Wind Engineering and Industrial Aerodynamics, 96, pp 1232-1239

Wilcox, D., (2006) Turbulence Modeling for CFD, 3<sup>rd</sup> Edition, DCW Industries

Wood, R., Bauer, S. (2003) Simple and Low-Cost Aerodynamic Drag Reduction Devices for Tractor-Trailer Trucks. SAE Technical Paper 2003-01-3377, doi:10.4271/2003-01-3377

Zhang, J., Li, Z., Bai, B., Zhang, L. (2012) Analysis and Simulation of Air Drag in Vehicles Close-Following, Applied Mechanics and Materials, 152-154, pp 1438-1442, doi:10.4028/www.scientific.net/AMM.152-154.1438

## 7. Appendices

### 7.1 Appendix A – Image Correlation Velocimetry Program Settings

When the program is given an image to analyze, there are a few options that the user has to set which control how the ICV program runs.

- `Velocity output skip (i and j)`: Determines how many pixels between the vectors in the horizontal (*i*) and vertical (*j*) direction
- `Max search distance (high res)`: This sets the maximum distance the correlation window searches before moving onto the next window to correlate. This value is determined by estimating the maximum velocity in the flow and back calculating into the number of pixels that corresponds to.
- `Correlation window half size (i and j)`: This is the size of the correlation window that the program used to search for patterns in the flow. There is a trade off on the size of the window, the smaller the window the more accurate and higher the resolution of the program output are, however if the window is too small there is not enough of a pattern for the program to correlate on and it will produce no significant results. If the window is made too large, the correlation window may include part of the flow that is at free-stream velocity, and another part which is accelerating. When the correlation window is moved to find where the pattern was moved to then the free-stream flow will be overestimated, and the velocity of the accelerating flow will be underestimated. In effect a larger correlation window will average parts of the flow out.
- `Deviation of correlation tables`: This sets the distance the correlation window is deviated when the program is using Correlation Based Correction. This value must be less than the correlation window size.
- `Calibration Parameter (alfa and beta)`: unused in the final version of the program
- `Calibration Parameter Threshold (threshold)`: This is the threshold for how intense a pixel needs to be in either red or blue, for the ICV program to use it when determining the pattern it will be searching for. If the value of either red or blue falls below this value, then that particular pixel is not used when correlating the pattern.

- `Calibration Parameter (corrthreshold)`: This value sets the minimum correlation required for the program to output data for any correlated data. Example, if this value is set to 0.8, then any data that is output will have at minimum a correlation value of 0.8. All other data is dropped from the output. This value ranges between 0 and 1, with 1 being a perfect correlation.
- `Pseudo cropping (istart -> iend, jstart-> jend)`: This is the interrogation window that the program runs inside of. This is used to cut down on the amount of the photo which is analyzed. Used mostly to trim the black regions out of the integration window.
- `Number of Tables (2, 4, 1)`: This is the number of tables used in Correlation Based Correction, a higher number is better if more accuracy is required in the output, however it significantly slows down the image analysis. If this value is set to 1, then correlation based correction is not used as only one correlation window is used. If the all the patterns in the photo are well defined, then correlation based correction is not as effective.
- `Max Velocity (half res, quarter res)`: These, like the Max Search Distance, set the distance the correlation window half size moves before stopping the search for how far a pattern has moved. Effectively the half res Max Velocity should be half of the Max Search Distance, and quarter res Max Velocity should be one quarter of the Max Search Dist.

## 7.2 Appendix B – Dimensions of Models

Presented in this section are the overall dimensions of the simplified model used in this study, as well as the deflector. All dimensions are in millimeters.

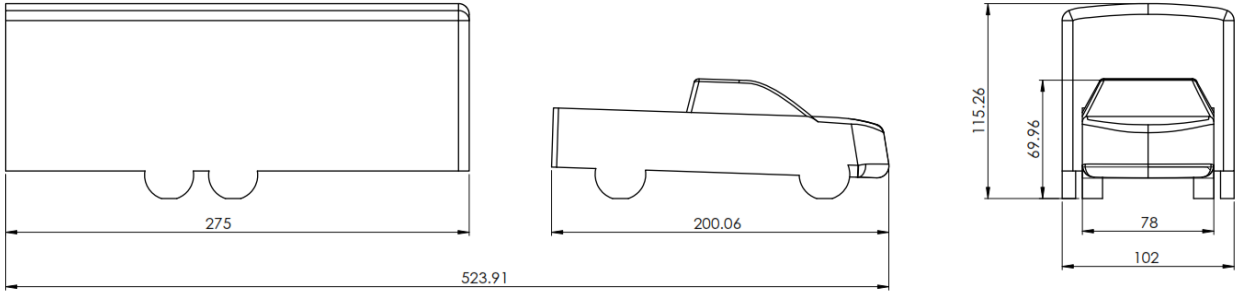


**Figure 62: Overall dimensions of the model, truck and trailer. Dimensions in millimeters.**

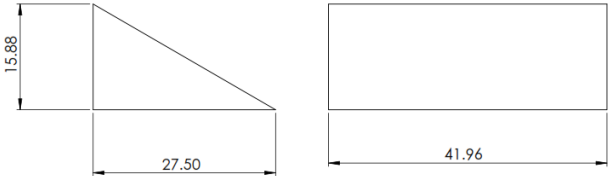
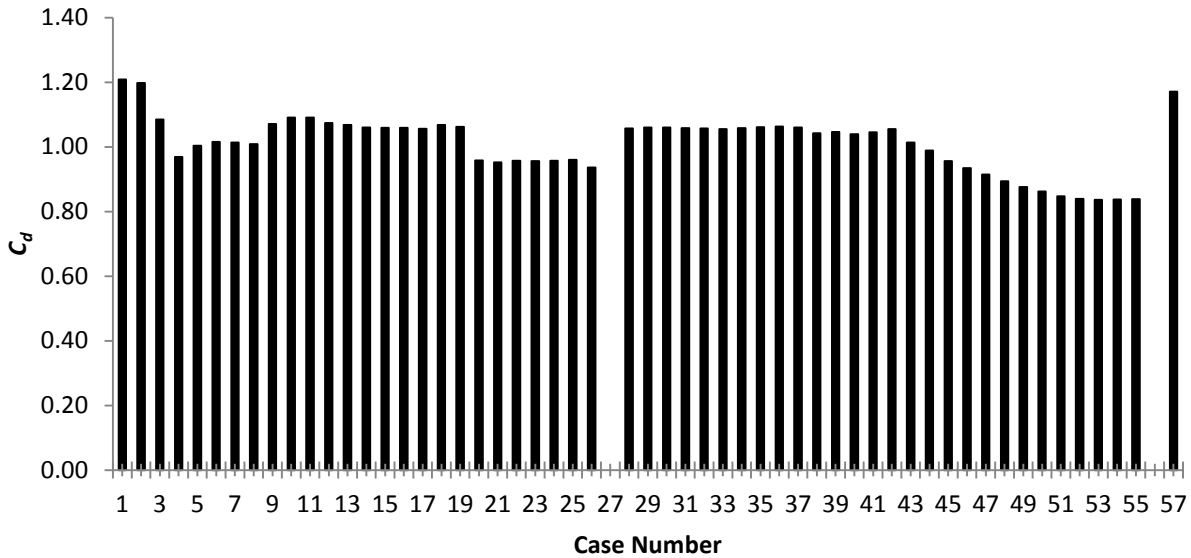


**Figure 63: Dimensions of the deflector. Dimensions in millimeters.**

Figure 62 shows the overall dimensions of the truck and trailer, and Fig. 63 shows the dimensions of the deflector.

### 7.3 Appendix C – Mesh Images of No Deflector Case

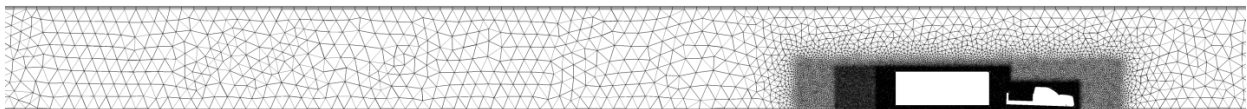
Presented in this section are an overview of all the mesh cases tested and their impact on the  $C_d$  value, and supplemental images showing the mesh of the no-deflector case.



**Figure 64:  $C_d$  vs. case number, overview of mesh evolution through testing.**

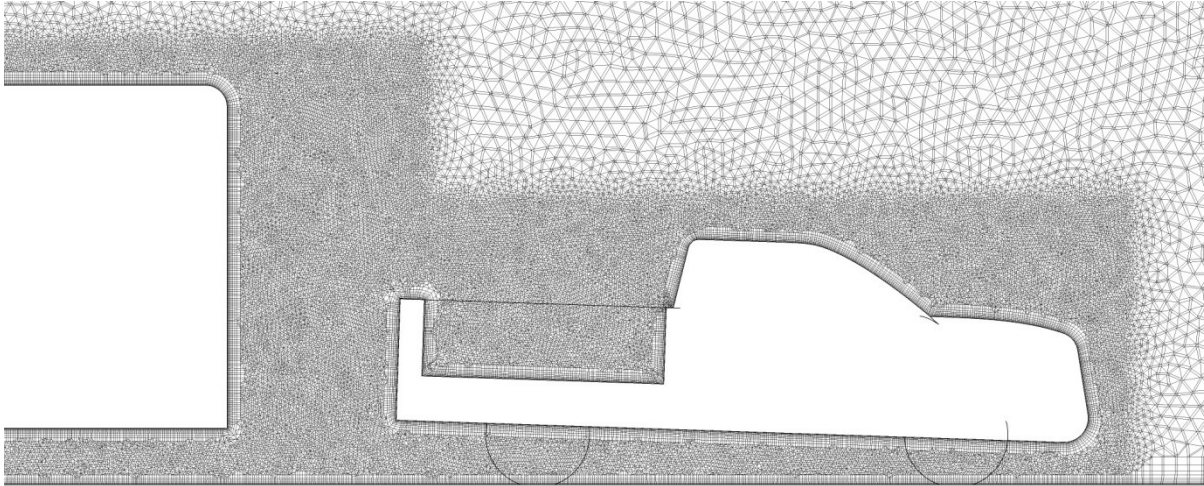
Figure 64 shows the  $C_d$  from the many test cases performed throughout the study. Many of these test cases were done to study the effect the mesh had on the results during the mesh setup/refinement. Other cases were used to see the effect changing the advection scheme, this can be seen between test cases 19 to 21, where the advection scheme was switched from Upwind Differencing Scheme (UDS) to Central Differencing Scheme (CDS).

Figure 65 shows the overall side mesh.



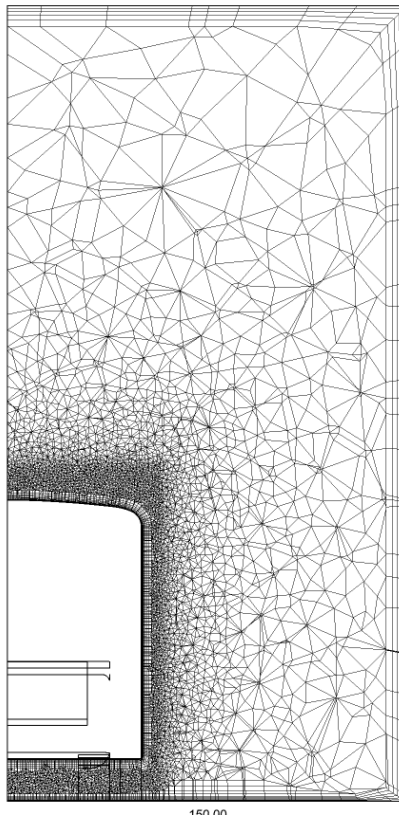
**Figure 65: No deflector side mesh.**

Figure 66 shows a zoomed detailed view of the side mesh.



**Figure 66: Zoomed view of no-deflector case side mesh.**

Figure 67 shows the mesh of the no-deflector case from the front.



**Figure 67: Front mesh of no-deflector case.**